

POLITECNICO DI TORINO

Master's Degree in Aerospace Engineering



**Politecnico
di Torino**

Master's Degree Thesis

**Low-Thrust Optimal Escape Trajectories
from Lagrangian Point L2 of the
Earth-Moon System**

Supervisors

Prof. LORENZO CASALINO

Candidate

MATTIA VENTO

December 2023

*To all the Dreamers
who live with the feet on the Earth
and the head in the Space*

Abstract

This thesis focuses on optimizing escape trajectories from the Lagrangian point of the Earth-Moon system in a higher fidelity model using electric propulsion. Lagrange points represent specific locations in space where objects placed there tend to remain stationary. At Lagrange points, the gravitational attraction exerted by two massive bodies exactly balances the centripetal force necessary for a smaller object to move with them. These points are useful for spacecraft to minimize the amount of fuel consumption required to maintain their position. Therefore, the exploitation of these points has become of great interest for the future space missions. In fact, among many uses, it also allows a gateway to Deep Space exploration. Among the countless trajectory available for a specific mission, the ones that require minimal propellant while still satisfying all the other conditions have been employed to optimize scientific results and minimize the associated costs.

To achieve this objective, this work addresses the optimization of escape trajectories using electric propulsion with the primary aim of reducing the amount of propellant required and, consequently, maximizing the payload mass. The optimization is achieved using an indirect method based on the optimal control theory. This method transforms the challenge of minimizing propellant usage into a multipoint boundary value problem, which is resolved through an iterative single-shooting process based on Newton's method. The case addressed in this work belongs to a particular subset of optimal control problems characterized by a discontinuous control law, known as "bang-bang". An automated tool is used to handle numerical complexities and identify suitable preliminary solutions. The problems relating to the discontinuity of the thrust were addressed, along with the delicacies of the indirect method, which strongly depend on the initial conditions, such as the a priori definition of the thrust structure. Pontryagin's Maximum Principle allows for adjusting suboptimal solutions when the thrust structure violates them in certain trajectories arcs.

The dynamical model encompasses the gravitational influences of four celestial bodies, whereby the spacecraft is influenced by the gravitational forces of the Earth, Moon and Sun. This model relies on JPL's ephemerides to account for the evolution of the positions of these celestial bodies over time. It also includes solar radiation pressure, the lunisolar gravitational effect and a spherical harmonic model for the Earth as perturbative additional effects. The complex gravitational interactions between the Sun, Earth and Moon dictate the trajectory dynamics near the starting point, i.e. the Lagrangian Point L2. In this highly complex framework, the optimal trajectory is sought among the sub-optimal ones, differentiating the various solutions from each other.

In particular, this work focuses on the Earth-Moon system, which presents more complexities related to the Moon's motion of revolution. First, a scenario is analyzed in which the departure date is varied along a whole lunar period maintaining fixed escape time and free terminal energy. Successively, specific dates among them are selected, and the escape durations is varied, still with free terminal energy. Lastly, a more complex analysis is carried out by fixing the terminal energy and letting the escape duration be free.

Acknowledgements

I would like to express my heartfelt gratitude to my professor Lorenzo Casalino that through his passion and expertise has helped to increase in me a deep interest in this field. In addition, I would like to thank him for giving me the opportunity to conduct research on Lagrangian Points.

I would like to extend my sincere gratitude to my university, Politecnico di Torino, for giving me the tools necessary for the formation of skills and knowledge that have been the foundation of this thesis.

Table of Contents

List of Tables	IV
List of Figures	V
1 Introduction	1
1.1 Motivation and Objectives	3
1.2 Thesis Overview	5
2 Dynamic Models	7
2.1 Reference Frames	8
2.1.1 Geocentric-Equatorial EME2000	9
2.1.2 Perifocal	9
2.1.3 Topocentric Zenith-East-Nord	10
2.1.4 Coordinate Transformations	11
2.2 Two-Body Problem	13
2.2.1 Constants of Motions	13
2.2.2 Sphere of Influence	14
2.2.3 Escape Velocity	14
2.2.4 Hyperbolic Excess Velocity	15
2.3 Three-Body Problem	15
2.3.1 Equation of Motion	18
2.3.2 Jacobi Constant	21
2.3.3 Equilibrium Solutions	22
2.3.4 Zero Velocity Surfaces	25
2.4 N-Body Problem	29
2.5 Equation of Motion in Spherical Coordinates	31
2.6 Perturbing Accelerations	32
2.6.1 Lunisolar Effect	32
2.6.2 Solar Radiation Pressure	34
2.6.3 Earth Asphericity	35

3	Optimal Trajectories	37
3.1	Direct and Indirect Numerical Method	37
3.2	Optimal Control Theory	39
3.2.1	Two-Point Boundary Value Problem	39
3.2.2	Boundary Conditions	41
3.2.3	Multi-Point Optimal Control Problem	44
3.3	Boundary Value Problem	46
3.4	Application of OCT in the Case Study	50
4	Escape Trajectories from Earth-Moon L2	54
4.1	Boundary Conditions	56
4.1.1	Terminal Conditions	57
4.1.2	Initial Conditions	58
4.1.3	Propellant Consumption	60
4.2	Escapes with imposed mission duration Δt	61
4.3	Escapes with variable mission duration Δt	68
4.4	Escapes with constrained final energy \mathcal{C}_{3f}	77
5	Conclusion	85
	Bibliography	87

List of Tables

2.1	Positions and Jacobi Constants of the Earth-Moon system, synodic RF. Credits:[17]	26
2.2	Characteristic quantities in NBP for Earth-Moon system	30
2.3	Spacecraft characteristic values	34
4.1	Selected departure epochs	59
4.2	Implemented electric propulsion system's main characteristic	60
4.3	EML2 escape trajectories performance - fixed $\Delta t = 75$ days, free \mathcal{C}_{3f}	62
4.4	EML2 selected escape trajectories	68
4.5	EML2 escape trajectories performance - variable Δt , free \mathcal{C}_{3f}	71
4.5	EML2 escape trajectories performance - variable Δt , free \mathcal{C}_{3f}	72
4.6	EML2 escape trajectories performance - free Δt , fixed \mathcal{C}_{3f}	80

List of Figures

2.1	EME2000 $\{\hat{\mathbf{I}}, \hat{\mathbf{J}}, \hat{\mathbf{K}}\}$, Perifocal $\{\hat{\mathbf{p}}_{SC}, \hat{\mathbf{q}}_{SC}, \hat{\mathbf{w}}_{SC}\}$, ZEN $\{\hat{\mathbf{u}}, \hat{\mathbf{v}}, \hat{\mathbf{w}}\}$ Reference Systems	8
2.2	Perifocal reference frame	9
2.3	Transformation from EME2000 RF to perifocal RF	12
2.4	Synodic reference system	16
2.5	Lagrangian Points in Earth-Moon synodic RF	24
2.6	3D Earth-Moon Zero-Velocity Surfaces at LPs energy. Credits:[17]	25
2.7	Forbidden regions in the Earth-Moon system for decreasing values of Jacobi's constant. Credits:[21]	27
2.8	Earth-Moon Zero-Velocity Surfaces at LPs energy. Credits:[17]	28
2.9	N-Body Problem EME2000 RF	29
2.10	Representation of third-body gravitational perturbation	33
3.1	Simplified representation of an MPBVP trajectory composed of n_p arcs	44
3.2	Simplified representation of nondimensional time t_ε in the j -th arc	46
3.3	Thrust angle in the topocentric RF of the spacecraft	52
4.1	Solar gravitational perturbation proportionality terms	55
4.2	Polar plot of σ_u, σ_v and σ in function of $\Delta\theta$ in SC-Earth rotating RF	55
4.3	EML2 escape trajectories over a lunar month - fixed $\Delta t = 75$ days, free \mathcal{C}_{3f} , EME2000 RF	61
4.4	EML2 escape trajectories over a lunar month - trend over time of cost and free final characteristic energy - fixed $\Delta t = 75$ days, free \mathcal{C}_{3f}	63
4.5	EML2 escape trajectories over a lunar month - trend over time of adjoint variables $\lambda_{r,0}, \lambda_{u,0}, \lambda_{v,0}$ - fixed $\Delta t = 75$ days, free \mathcal{C}_{3f}	64
4.6	EML2 selected escape trajectories over a lunar month - trend over time of Sun-SC relative angle, Moon-SC relative angle and optimal thrust angle - fixed $\Delta t = 75$ days, free \mathcal{C}_{3f}	65
4.7	EML2 selected escape trajectories polar plot - fixed $\Delta t = 75$ days, free \mathcal{C}_{3f} , Earth-Spacecraft rotating RF	66

4.8	EML2 escape trajectories over a lunar month - fixed $\Delta t = 75$ days, free \mathcal{C}_{3f} , SE synodic RF	67
4.9	EML2 selected escape trajectories over a lunar month - variable Δt , free \mathcal{C}_{3f} , EME2000 RF	70
4.10	EML2 selected escape trajectories - trend over time of Sun-SC relative angle - variable Δt , free \mathcal{C}_{3f}	73
4.11	EML2 selected escape trajectories - trend over time of optimal thrust angle - variable Δt , free \mathcal{C}_{3f}	74
4.12	EML2 selected escape trajectories polar plot - variable Δt , free \mathcal{C}_{3f} , Earth-Spacecraft rotating RF	75
4.13	EML2 selected escape trajectories - variable Δt , free \mathcal{C}_{3f} , SE synodic RF	76
4.14	EML2 selected escape trajectories over a lunar month - free Δt , fixed \mathcal{C}_{3f} , EME2000 RF	79
4.15	EML2 selected escape trajectories - trend over time of Sun-SC relative angle - free Δt , fixed \mathcal{C}_{3f}	81
4.16	EML2 selected escape trajectories - trend over time of optimal thrust angle - free Δt , fixed \mathcal{C}_{3f}	82
4.17	EML2 selected escape trajectories polar plot - free Δt , fixed \mathcal{C}_{3f} , Earth-Spacecraft rotating RF	83
4.18	EML2 selected escape trajectories - free Δt , fixed \mathcal{C}_{3f} , SE synodic RF	84

Chapter 1

Introduction

Space exploration has consistently played a pivotal role in the initiatives of various space agencies. Presently, the engagement in space activities not only manifests as a consolidated presence in Earth's orbits, notably exemplified by the International Space Station (ISS), but also extends to the presence in advanced telecommunication, navigation, and monitoring systems. As outlined in the Global Exploration Roadmap, the focus in the present and forthcoming decades will transition towards exploring our Solar System[1]. Space agencies are increasingly dedicating their efforts to the establishment of long-term infrastructure in the cis-lunar space. This renewed commitment is evident in recent missions as for example NASA's Artemis, the Chinese Chang'e 6 mission, and the Lunar Orbital Platform - Gateway (LOP-G), formerly known as the Deep Space Gateway (DSG)[2, 3]. The purpose of this orbiting platform is to streamline deep space operations, facilitate the utilization of lunar resources, and serve as a central hub for supplying other spacecraft, such as the Deep Space Transport, during their journeys to and from far-off destinations.

As attention increasingly gravitates towards missions extending beyond Earth, such as those targeting the Moon and Mars, the complexities and requirements of these endeavors become more pronounced. Certain requirements in space missions can be negotiable, but others significantly limit the options and determine if a mission is feasible or not. One particularly strict requirement is the availability of propellant, as there are currently no refueling stations built in the solar system by humans. Since the inception of space exploration, the assessment of a mission's value has been closely linked to the payload — the quantity of "useful" goods a spacecraft can carry. The goal of maximizing the payload, namely achieving the maximum scientific return in exchange for the costs associated with the conception, design, and realization of the mission, plays a fundamental role. This objective can be attained through two distinct approaches: constructing a larger spacecraft or creating more available space within the spacecraft itself. The feasibility of the first approach is limited, while the second involves adjusting the only other variable

quantity within the vehicle, that is the propellant.

The Rocket Equation, formulated by Konstantin Eduardovich Tsiolkovsky in 1903, is fundamental to understand the relationship between the mass of a rocket and the amount of propellant it consumes during its journey[4]. Mathematically, the Rocket Equation is expressed as:

$$\frac{m_p}{m_0} = 1 - \exp\left(-\frac{\Delta V}{I_{sp}g_0}\right) \quad (1.1)$$

The propellant required is a function of g_0 , the gravitational acceleration at sea level, and two other parameters: ΔV , representing the required change in velocity for the space vehicle to transition from point A to point B, and the I_{sp} term, known as the specific impulse. The first parameter measures the cost of reaching the target, while the second measures how efficiently a thruster consumes propellant. As deep-space exploration missions evolve, an escalating demand for substantial ΔV underscores the need for a concurrent increase in specific impulse to render these missions viable. Conventional chemical propulsion systems, which are capable of generating a large amount of energy in a very short time, but which are characterized by a specific impulse in the hundreds of seconds range, e.g. the most high-performance propellant combination to date, LOX-LH2, develop a specific impulse of 450 seconds. Due to physical limitations, no obvious improvements are possible in the short term for this type of propulsion. Nonetheless, an alternative solution lies in electric propulsion, an avenue extensively researched and tested in the past but only nowadays finding practical applications in space application. Through various electric propulsion systems—electrothermal, electrostatic, and electromagnetic—it is possible to achieve specific impulses exceeding 5000 seconds. The drawback of this type of propulsion lies in the relatively low thrust levels provided over time and the requisite ΔV tends to be higher than the ideal. Consequently, thrust phases transition from the minutes of chemical propulsion to the hours, days and even weeks of electric propulsion. Managing these prolonged thrust phases demands meticulous precision and continual adjustments over time.

Two primary branches of numerical methods, direct and indirect, have historically been employed for solving boundary value problems. Both aim to address infinite-dimensional time-continuous problems[5]. Direct methods transcribe the original problem into subclasses subject to algebraic constraints, discretizing functions into a mesh. The refinement level of this mesh balances accuracy and computational cost, often requiring a high number of variables. Despite computational challenges, direct methods exhibit robustness against initial guesses but may lack accuracy, necessitating further refinement. Conversely, indirect methods are generally faster due to a smaller set of variables. They produce accurate optimal solutions or offer insights for improving potentially suboptimal ones. Indirect methods introduce adjoint variables and Lagrange multipliers, forming an augmented problem with

necessary conditions for optimality. Retrieving these conditions case-by-case demands a deeper understanding of the problem. Despite their sensitivity to initial conditions and potential poor convergence, some drawbacks inherent to indirect methods can be minimized. In complex problems, direct methods are traditionally preferred, but similar problems are now being addressed using indirect methods due to their expanded applicability[6].

1.1 Motivation and Objectives

The trajectory optimization addressed in this thesis delves into the intricacies of minimizing propellant usage for an escape trajectory from Lagrangian Points using electric propulsion in a higher fidelity model. The selection of this scenario could offer an explanation for the notable interest in Lagrangian Points in recent years. These points represent specific equilibrium positions within the three-body problem, where small objects like spacecraft can maintain relatively fixed and stable positions relative to two primary bodies in a rotating reference system. Because of their various advantages, including suitability for deep space exploration, both space agencies and the scientific community have displayed immense interest in utilizing these Lagrangian points. This keen interest is underscored by the planning and execution of numerous missions, both directed to and from these strategically significant points in space.

For instance, the European Space Agency (ESA) is actively advancing the VIGIL mission[7], previously known as Lagrange, with the goal of monitoring solar activity and providing early warnings for incoming solar storms, enabling better protection for orbiting spacecraft, ground infrastructure, and future explorers. Two spacecrafts will be strategically positioned at the Sun-Earth Lagrangian Points L1 and L5 to facilitate this mission. Numerous missions have already been scheduled and launched for the Sun-Earth Lagrangian Point L2 (SEL2), among them the EUCLID space telescope[8], which was launched on July 1, 2023. This telescope is designed to investigate the expansion of the universe, dark matter, and dark energy. Concurrently, other missions such as PLATO[9] and ARIEL[10], focused on the study of exoplanets, are still in the development phase. Moreover, missions are currently in development to depart from these precise points, particularly in the realm of interplanetary exploration. A noteworthy instance is the Comet Interceptor mission[11, 12] scheduled for launch in 2029, directed towards the SEL2 point in conjunction with the ARIEL mission. Following an initial waiting phase for target selection, the Comet Interceptor will leave SEL2, undertaking a mission to explore a long-period comet (LPC) or an undiscovered interstellar object as it approaches Earth's orbit.

Similarly, NASA, CSA, ESA, and JAXA are currently engaged in the development of the Lunar Orbital Platform - Gateway[2]. This innovative platform will be placed in a stable orbit close to the Earth-Moon Lagrangian Point L2 (EML2), specifically adopting a Neo-Rectilinear-Halo-Orbit with a 9:2 resonance. Designed as a versatile outpost, the station is poised to play a pivotal role, offering indispensable support for lunar surface missions, serving as a hub for scientific endeavors, and acting as a critical staging point for extended deep space exploration, including initiatives like the Deep Space Transport. Therefore, the examination of departure trajectories from LOP-G is particularly intriguing, as they demand minimal propulsive effort and are thus ideally suited for implementation through electric propulsion.

In prior research, Ref.[13] explored escape maneuvers from the Sun-Earth Lagrangian Point L2 using the Circular Restricted Three-Body Problem (CR3BP) model. The approach in this study initially treats maneuvers as impulsive and subsequently extends them to incorporate finite low-thrust electric propulsion. Conversely, research on the Earth-Moon Lagrangian Points, as discussed in works [14], does not primarily focus on low-thrust trajectories. In another study [15], escape trajectories from EML2 are analyzed within the Sun-Earth-Moon Bi-Circular Restricted Four-Body Problem (BCR4BP) model, taking into account the Sun's gravitational perturbation and the relative angular position of the Moon, but employs impulsive maneuvers. In the works [16, 17], there is, however, a parallel to the research conducted in this thesis, which makes an effort to expand upon the outcomes achieved in the analysis of escape trajectories from EML2.

The selected scenario for this thesis focuses on direct escape trajectories from the Earth-Moon Lagrangian point L2, employing a higher fidelity model and electric propulsion. The dynamics in the vicinity of these Lagrangian points are intricate due to the complex gravitational interaction between the Sun, Earth and Moon. Consequently, the dynamic model employed in this thesis adopts a 4-body gravitation approach, accounting for the gravitational influences of Earth, Moon, and Sun. The DE430 JPL's ephemerides are utilized to track the states of these gravitational bodies over time. Furthermore, various perturbations and gravitational effects, such as solar radiation pressure, a spherical harmonic model for the Earth, and the lunisolar gravitational effect, are taken into account.

This research aims to identify optimal trajectories and establishes a general framework for distinguishing them from sub-optimal ones. The analysis of time-continuous problem domains requires the careful selection of a suitable numerical method. Specifically, employing a numerical model that provides theoretical insights into improving sub-optimal solutions would be highly beneficial for this purpose. In this thesis, the optimization is achieved using an indirect method based on the optimal control theory. This method transforms the challenge of minimizing propellant usage into a multipoint boundary value problem, resolved through an

iterative single-shooting process based on Newton’s method. The case addressed in this work belongs to a particular subset of optimal control problems characterized by a discontinuous control law, known as “bang-bang”. An automated tool is used to handle numerical complexities and identify suitable preliminary solutions. The problems related to the discontinuity of the thrust were addressed, along with the delicacies of the indirect method, which strongly depend on the initial conditions, such as the a priori definition of the thrust. Pontryagin’s Maximum Principle allows for adjusting sub-optimal solutions when the thrust structure violates them in certain trajectories arcs.

The main goals of this thesis are:

- Improve the results of previous research on the escape trajectories from EML2;
- Analyze the influence of Earth’s motion around the Sun and the Moon’s motion around the Earth on escape trajectories from EML2;
- Investigate scenarios where the departure date is varied along a lunar period while maintaining a fixed escape time and free terminal energy;
- Select specific dates within the varied departure dates and analyze the effect of varying escape durations while keeping terminal energy free;
- Perform a more comprehensive and more complex analysis, focusing on the previously chosen dates, by fixing the terminal energy and allowing the variation of the escape’s duration;

1.2 Thesis Overview

To achieve the above research objectives, the thesis is organized as follows:

Chapter 2 presents a first view on the reference systems used in the analysis and a detailed description of the dynamic model. A clarification of basic astrodynamics concepts is addressed, followed by an in-depth study of the three-body problem and n-body problem to provide a clear understanding of the context of the scenario under consideration. In this Chapter is also discussed the perturbative accelerations included in the model and their impact.

Chapter 3 presents the Optimal Control Theory with a description of the Two-Point Boundary Value Problem and the Multi-Point Boundary Value Problem which is the one applied in the case study. The differences between the direct method and the indirect one are discussed. The Chapter provides major focus on

the second method which is the one applied to the case study.

Chapter 4 analyzes the optimal solutions of the escape trajectories from the Lagrangian Point L2 of the Earth-Moon system, computed using the n-body dynamic model described in Chapter 2. First there is a focus on the Boundary Conditions followed by an in-depth analysis on three particular cases: fixed duration, variable duration and variable \mathcal{E}_{3f} . Optimal thrust structure, thrust strategies, optimal thrust directions and favourable exploitation of the lunisolar perturbation are also addressed.

Chapter 5 provides the conclusion with a summary of the key points of this thesis..

Chapter 2

Dynamic Models

In this Chapter is presented a detailed description of the dynamic model used in the analysis. While this work is grounded in the use of n-body Equations of Motion (EOM) in a higher-fidelity model, initial considerations are made regarding the Three-Body Problem (3BP) to provide a clearer understanding of the context of the scenario under consideration.

The initial section of the chapter introduces the reference systems used in ephemeris models. A quick overview is given of the fundamental concepts of orbital mechanics, which are essential for understanding the following sections of this thesis. For example, an introduction to the two-body problem and classical orbital parameters is provided. For more complete information, please refer to well-known books on orbital mechanics, such as [18–21]. The following part of the chapter presents the dynamic model for the three-body problem and the n-body problem in detail. The final section discusses the impact of perturbative accelerations.

Throughout this thesis, the same notation as in Mascolo’s Ph.D. dissertation[17] will be utilized; indeed, the present research commences from such heritage. Vectors, presented as column vectors, will be represented in bold lowercase font (\mathbf{x}), except for known quantities (such as velocity \mathbf{V} and thrust \mathbf{T}); unit vectors in bold lowercase with a hat ($\hat{\mathbf{x}}$); matrices denoted by a bold uppercase font (\mathbf{A}). Quantities derived with respect to time will be marked through a dot or a plus dot equal to the order of derivation. Greek letters and calligraphic fonts such as Ralph Smith’s Formal Script and Zapf Chancery, will be used for describing certain known quantities and for quantities that have undergone mathematical manipulation, such as nondimensionalization. If these quantities are represented by the same graphic characters as the corresponding Latin characters, a superscript will be used to distinguish nondimensional from dimensional quantities ($\check{x}, \check{\check{x}}$).

2.1 Reference Frames

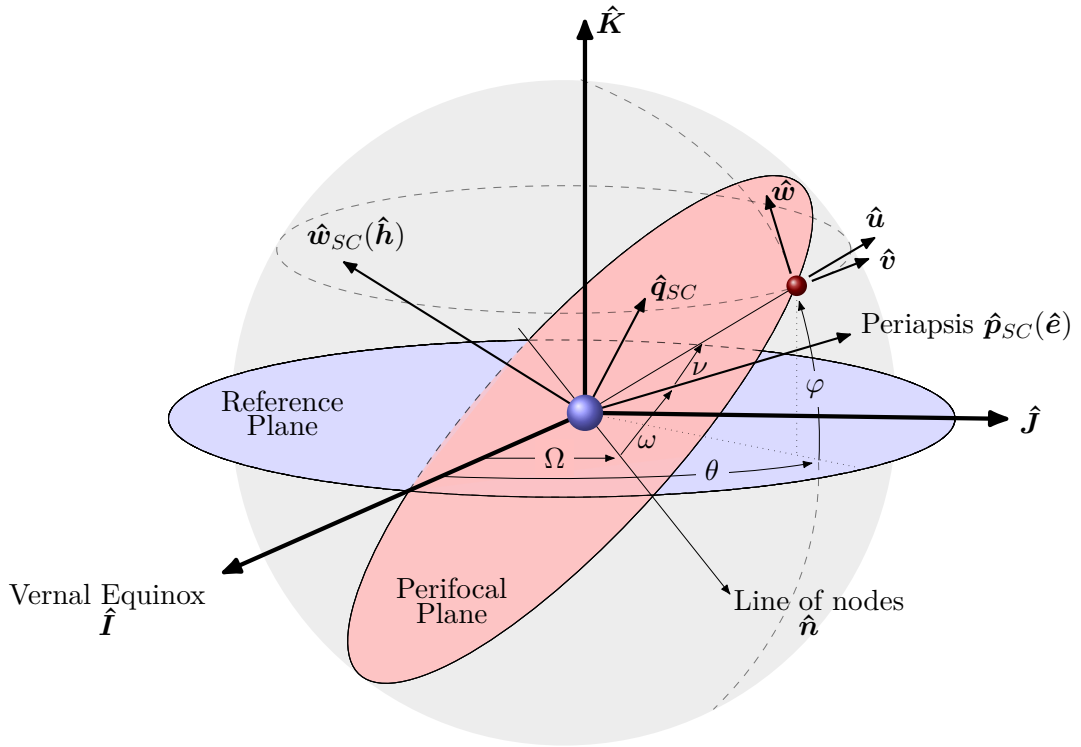


Figure 2.1: EME2000 $\{\hat{I}, \hat{J}, \hat{K}\}$, Perifocal $\{\hat{p}_{SC}, \hat{q}_{SC}, \hat{w}_{SC}\}$, ZEN $\{\hat{u}, \hat{v}, \hat{w}\}$ Reference Systems

A reference system is generally defined by a fundamental plane, an origin and a set of mutually orthogonal right-hand axes. Two types of reference frame (RF) can be distinguished: inertial and non-inertial, with the primary distinction lying in the state of motion. The first one is characterized by an object either remaining at rest or moving at a constant velocity unless subjected to an external force. In contrast, the second one is undergoing accelerating or rotating. In non-inertial one, apparent forces manifest, such as the centrifugal and Coriolis forces, due to the relative motion of the reference system itself. The choice between inertial and non-inertial reference systems depends on the nature of the analysis to be conducted. For instance, when representing the trajectory of a spacecraft in relation to the Earth, it is more convenient and comprehensible to utilize an inertial RF.

2.1.1 Geocentric-Equatorial EME2000

In this study, the equatorial geocentric reference frame aligns precisely with the Earth Mean Equator and Equinox of Epoch J2000 (EME2000), as illustrated in Figure 2.1. The origin is situated at the center of the Earth, the fundamental plane corresponds to the equatorial plane, and the versors $\{\hat{\mathbf{I}}, \hat{\mathbf{J}}, \hat{\mathbf{K}}\}$ are defined with $\hat{\mathbf{I}}$ aligned towards the vernal equinox, $\hat{\mathbf{K}}$ normal to the reference plane, and $\hat{\mathbf{J}}$ completing the triad. JPL's ephemerides, belonging to the DE400 series (such as DE430, employed in this thesis), are referenced within the International Celestial Reference Frame (ICRF)[22, 23]. The incorporation of libration and nutation motions in the ICRF leads to the characterization of EME2000 as quasi-inertial. Despite a rotational difference of 0.01 arcsecond between the EME2000 and the ICRF dynamical system, determined with an accuracy of 0.001 arcsecond, the EME2000 RF is still classified as inertial[24].

2.1.2 Perifocal

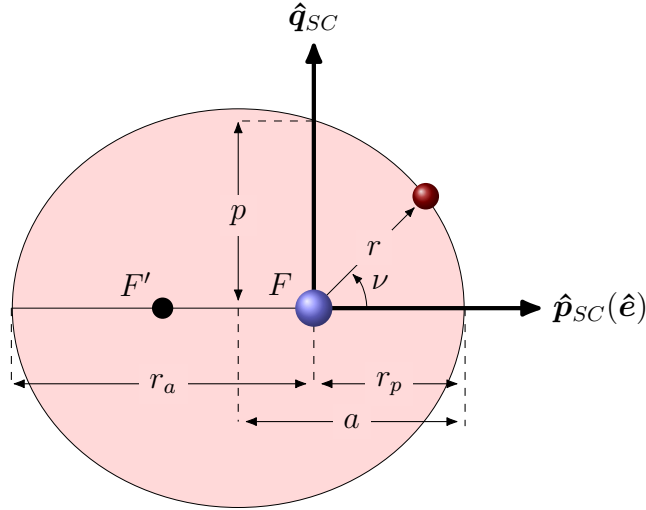


Figure 2.2: Perifocal reference frame

One of the most practical reference systems employed for describing satellite motion is the perifocal coordinate system, as shown in the Figure 2.2. Here the origin is situated at the center of the gravitational body's in the primary focus, the fundamental plane corresponds to the plane of the satellite's orbit and its unit vectors are $\{\hat{\mathbf{p}}_{SC}, \hat{\mathbf{q}}_{SC}, \hat{\mathbf{w}}_{SC}\}$. The $\hat{\mathbf{p}}_{SC}$ one is precisely aligned with the eccentricity vector, indicating the direction toward the periapsis, the closest point in the orbit. Vector $\hat{\mathbf{w}}_{SC}$ is normal to the plane of the orbit and it is aligned to the direction

of the angular momentum vector $\hat{\mathbf{h}}$. Finally, the unit vector $\hat{\mathbf{q}}_{SC}$ completes the right-handed triad of the perifocal system.

According to Kepler's first law, in the absence of external perturbations, a spacecraft in this reference system would describe an infinite conic, assuming it is closed. The shape and orientation of this conic in space can be uniquely described with the use of different ways, including the famous Keplerian orbital parameters $\{a, e, i, \Omega, \omega, \nu\}$. In the case of a closed orbit, only three of these are sufficient to represent the trajectory in the perifocal reference system: the semi-major axis a and eccentricity e that describe, respectively, its shape and size, and the other one is the true anomaly ν which define the position of the spacecraft along the trajectory. The third parameter identifies the angular position of the spacecraft with respect to periapsis. Sometimes it is also possible to use the mean anomaly M . The semi-major axis and eccentricity are linked by the semi-latus rectum $p = a(1 - e^2)$, which is sufficient to represent an orbit in the perifocal RF, by the well-known conic equation[18, 19, 21]:

$$r = \frac{a(1 - e^2)}{1 + e \cos \nu} \quad (2.1)$$

In order to represent the conic and, consequently, the orientation of the perifocal plane in three-dimensional space, namely with respect to the EME2000 RF, the last three orbital parameters are required. Specifically, the orbital plane can be inclined with respect to the fundamental plane (the equatorial one) by an angle called inclination i . The intersection between the reference plane and the orbit plane gives the line of nodes $\hat{\mathbf{n}}$, which defines the transition of the spacecraft during orbit from the southern to the northern hemisphere and vice versa, at the ascending and descending nodes, respectively. The main direction of the line of nodes indicates the ascending node and is measured in the geocentric-equatorial reference system from the axis through the right ascension of the ascending node (RAAN) Ω . The last of the six classical orbital parameters is the argument of the periapsis ω , which, in the case of non-circular and non-equatorial orbits, indicates the position of the latter from the line of nodes. For a more detailed description, please refer to the well-known books on orbital mechanics.

2.1.3 Topocentric Zenith-East-Nord

The final reference system under consideration is a topocentric, rotating, non-inertial, commonly known as the Zenith-East-North (ZEN) RF, defined by the triad $\{\hat{\mathbf{u}}, \hat{\mathbf{v}}, \hat{\mathbf{w}}\}$. Generally, this triad is used for the convenient description of the satellite's velocity components in the radial, tangent, and normal directions, respectively. The radial direction is obtained by extending the spacecraft's position vector with respect to the centre of the Earth; the tangent one coincides with the direction of

the parallel of the celestial sphere, while the normal one coincides with that of the meridian.

2.1.4 Coordinate Transformations

The coordinates of a vector can be expressed in any reference system, but there is often a need to convert between systems. It is important to note that during a coordinate rotation, only the base of the vector undergoes a change. In other words, the vector retains its original length and direction, but the specific components associated with the coordinate axes may vary as it transitions from one system to another[19]. Moving from one reference system to another involves the use of rotation matrices. These matrices are crafted from an elementary set of Direction Cosine Matrices, which, for a generic positive rotation, are in the following form

$$\mathbf{R}_1(\cdot) = \begin{bmatrix} 1 & 0 & 0 \\ 0 & \cos(\cdot) & \sin(\cdot) \\ 0 & -\sin(\cdot) & \cos(\cdot) \end{bmatrix} \quad (2.2a)$$

$$\mathbf{R}_2(\cdot) = \begin{bmatrix} \cos(\cdot) & 0 & \sin(\cdot) \\ 0 & 1 & 0 \\ -\sin(\cdot) & 0 & \cos(\cdot) \end{bmatrix} \quad (2.2b)$$

$$\mathbf{R}_3(\cdot) = \begin{bmatrix} \cos(\cdot) & \sin(\cdot) & 0 \\ -\sin(\cdot) & \cos(\cdot) & 0 \\ 0 & 0 & 1 \end{bmatrix} \quad (2.2c)$$

To simplify the discussion, consider Figure 2.3, which shows the transition from the EME2000 inertial RF to the perifocal RF. The first step is a rotation around the $\hat{\mathbf{K}}$ -axis of Ω

$$\mathbf{r}_{I'J'K'} = \mathbf{R}_3(\Omega)\mathbf{r}_{IJK} \quad (2.3)$$

from this, the rotated $\hat{\mathbf{I}}$ -axis coincides with the line of nodes $\hat{\mathbf{n}}$. The next rotation is around the rotated $\hat{\mathbf{I}}$ -axis of i

$$\mathbf{r}_{I''J''K''} = \mathbf{R}_1(i)\mathbf{r}_{I'J'K'} \quad (2.4)$$

In this way, the $\hat{\mathbf{K}}'$ -axis, after rotation, coincides with the $\hat{\mathbf{w}}_{SC}$. Lastly, a final rotation around $\hat{\mathbf{K}}'$ of ω

$$\mathbf{r}_{pqw} = \mathbf{R}_3(\omega)\mathbf{r}_{I''J''K''} \quad (2.5)$$

resulting in the coincidence of $\hat{\mathbf{I}}'''$ with $\hat{\mathbf{p}}_{SC}$ and $\hat{\mathbf{J}}'''$ with $\hat{\mathbf{q}}_{SC}$. The angles of rotation required to align one reference system with another are also known as Euler

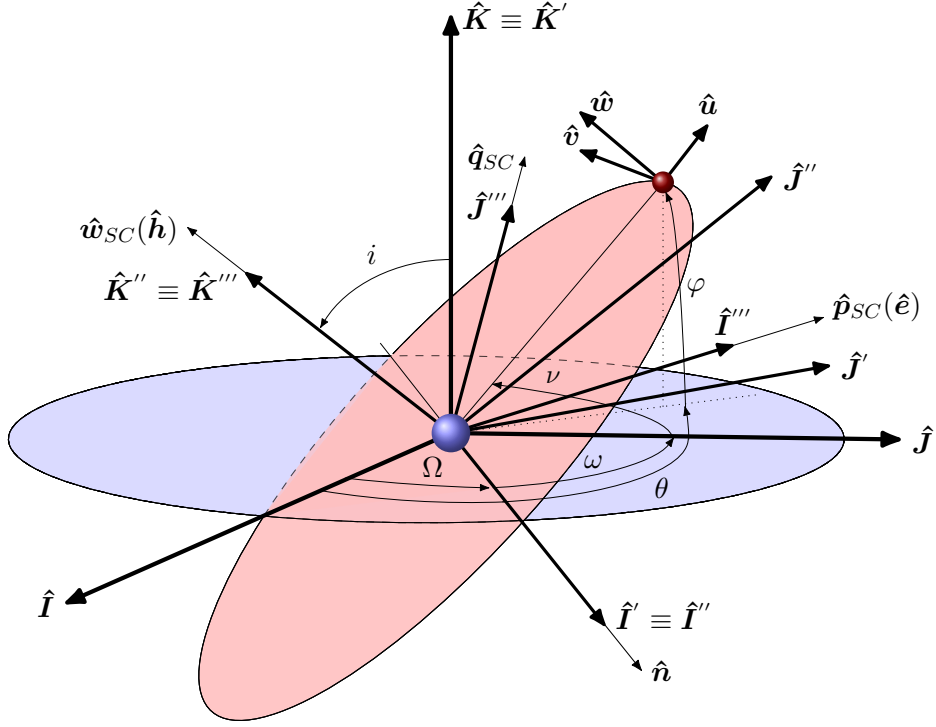


Figure 2.3: Transformation from EME2000 RF to perifocal RF

angles. A maximum of three Euler angle rotations is sufficient for this purpose. The transformation matrix between two reference systems is denoted by the following notation: the subscript, composed of a number of single digits indicating the type of rotation performed, is equal to the number of elementary rotations applied, and the brackets contain the respective angles used for the rotations. Thus, in the example

$$\mathbf{R}_{313}(\omega, i, \Omega) \quad (2.6)$$

consequently

$$\mathbf{r}_{pqw} = \mathbf{R}_3(\omega)\mathbf{r}_{I''J''K''} = \mathbf{R}_3(\omega)\mathbf{R}_1(i)\mathbf{r}_{I'J'K'} = \mathbf{R}_3(\omega)\mathbf{R}_1(i)\mathbf{R}_3(\Omega)\mathbf{r}_{IJK} \quad (2.7)$$

In a similar way, the other main rotation used in this work can also be obtained, and it takes the following form

$$\mathbf{r}_{ZEN} = \mathbf{R}_{23}(\varphi, \theta)\mathbf{r}_{IJK} \quad (2.8)$$

Inverse rotations can be calculated simply by transposing DCMs.

2.2 Two-Body Problem

The evolutionary state of a spacecraft, described in an inertial reference system such as EME2000, takes the form of a set of ordinary differential Equations(2.9), that describe how the spacecraft's position, velocity vector, and mass change over time under the action of external forces and perturbations.

$$\frac{d\mathbf{r}}{dt} = \mathbf{V} \quad (2.9a)$$

$$\frac{d\mathbf{V}}{dt} = \mathbf{g} + \frac{\mathbf{T}}{m} + \frac{\mathbf{D}}{m} + \frac{\mathbf{L}}{m} + \mathbf{a}_P \quad (2.9b)$$

$$\frac{dm}{dt} = -\frac{T}{c} \quad (2.9c)$$

In the present work, all analyzed trajectories are outside the Earth's atmosphere; therefore, the aerodynamic force terms, specifically drag \mathbf{D} and lift \mathbf{L} , can be considered negligible. The term \mathbf{g} represents gravitational acceleration:

$$\mathbf{g} = -\frac{\mu}{r^2} \frac{\mathbf{r}}{r} \quad (2.10)$$

The above set of equations admits an analytical solution in the so-called Two-Body Problem (2BP), assuming that the bodies are spherically symmetric and that there are no additional external or internal forces other than gravity acting along the line connecting the two bodies. For a more detailed explanation please refer to [18, 19, 21].

2.2.1 Constants of Motions

Two interesting quantities can be derived from the equations of motion regarding the nature of the orbital motion.

The first one is the conservation of the specific mechanical energy for any orbit

$$\mathcal{E} = \frac{V^2}{2} - \frac{\mu}{r} \quad (2.11)$$

where the first term is the kinetic energy per unit mass and the second is the potential energy per unit mass.

The second information derived from the Two-Body Problem (2BP) is the conservation of specific angular momentum for every specific orbit

$$\mathbf{h} = \mathbf{r} \times \mathbf{V} \quad (2.12)$$

Via ulterior considerations, the specific mechanical energy can be linked to the shape of the orbit through the semi-major axis

$$\mathcal{E} = -\frac{\mu}{2a} \quad (2.13)$$

Two types of orbits, closed and open, can be distinguished depending on the value assumed by \mathcal{E} . Negative values correspond to elliptical orbits; conversely, a value equal to or greater than zero indicates parabolic or hyperbolic orbits, respectively.

2.2.2 Sphere of Influence

It is worth defining the concept of the Sphere of Influence (SOI), which refers to the region where a small body, such as a spacecraft, can be considered to be influenced primarily by the gravitational attraction of a single celestial body, while the gravitational effects of other bodies can be neglected. The concept of a SOI is often applied in preliminary analyses of interplanetary trajectories to simplify complex problems into more manageable 2-Body Problem sub-problems. The SOI's shape is intricately dependent on the gravitational interactions among various celestial bodies. As a first approximation, it can be considered as a perfect sphere with a radius of [21]

$$r_{SOI} = r_{ij} \left(\frac{m_j}{m_i} \right)^{\frac{2}{5}} \quad (2.14)$$

where, m_i represents the mass of the largest, principal body, m_j denotes the mass of the smallest, secondary body, and r_{ij} is the position vector of the j-th secondary gravitational body relative to the i-th primary gravitational body.

In this thesis, it has been assumed that the escape is complete when the spacecraft reaches a distance from the main body equal to three times the radius of the sphere of influence. Given the Earth's SOI is approximately 0.925×10^6 km, the specified limit in this analysis is 3 million kilometers relative to the center of the Earth.

2.2.3 Escape Velocity

Since the specific mechanical energy remains constants throughout the whole orbit, it can be used to compare two states of the same orbit. Writing this equation first for a generic point situated at a distance r from the center of a gravitational body and then for a second point at an infinite distance, where the speed will be zero, provides

$$\mathcal{E} = \frac{V_e^2}{2} - \frac{\mu}{r} = \frac{V_\infty^2}{2} - \frac{\mu}{r_\infty} \quad (2.15)$$

From this, the minimum escape velocity - the speed a spacecraft which starts from a generic point would need to achieve to reach an infinite distance from the

gravitational body, following a parabolic trajectory, to arrive with zero velocity - can be determined

$$V_e = \sqrt{\frac{2\mu}{r}} \quad (2.16)$$

2.2.4 Hyperbolic Excess Velocity

In the same way, when the spacecraft is initially given a velocity greater than the minimum escape velocity, it can be expected that once it reaches the infinite distance from the central gravitational body, on the respective hyperbolic trajectory, it will no longer arrive with zero velocity. Instead, there will be a residual velocity, referred to as hyperbolic excess velocity V_∞

$$\mathcal{E} = \frac{V^2}{2} - \frac{\mu}{r} = \frac{V_\infty^2}{2} - \frac{\mu}{r_\infty} \Rightarrow V_\infty = \sqrt{V^2 - \frac{2\mu}{r}} = \sqrt{V^2 - V_e^2} \quad (2.17)$$

A common way to directly measure excess specific energy is to use the characteristic energy \mathcal{C}_3 , which is defined as twice the mechanical specific energy

$$\mathcal{C}_3 = 2\mathcal{E} = V^2 - \frac{2\mu}{r} = -\frac{\mu}{a} \quad (2.18)$$

It is worth noting that for trajectories with a hyperbolic excess of velocity \mathcal{C}_3 is equal to V_∞^2 .

2.3 Three-Body Problem

The relations derived from the 2BP form the foundation of a lot of work in astrodynamics. However, in certain cases, it becomes necessary to include other bodies to accurately model real physics phenomena. The Three-Body Problem (3BP) is a particular case of the N-Body dynamical model used in this thesis. This problem can be further simplified to the Circular Restricted Three-Body Problem (CR3BP) by introducing some simplifications, which will be explained in detail in the following sections. The CR3BP studies the interaction that exists between three bodies, two are the main one and the other one has a negligible mass. In contrast to the 2BP, there is no-closed-form solution for the equations of motion in the 3BP, much less in the CR3BP. Indeed, the dynamic model obtained from this scenario proves chaotic motion of the bodies for most of the initial conditions, necessitating the use of numerical integration for accurate predictions. A historically well-known example of a three-body problem is one that involves the Sun, Earth, and the Moon. This section analyzes 3BP as it relates to a generic binary system.

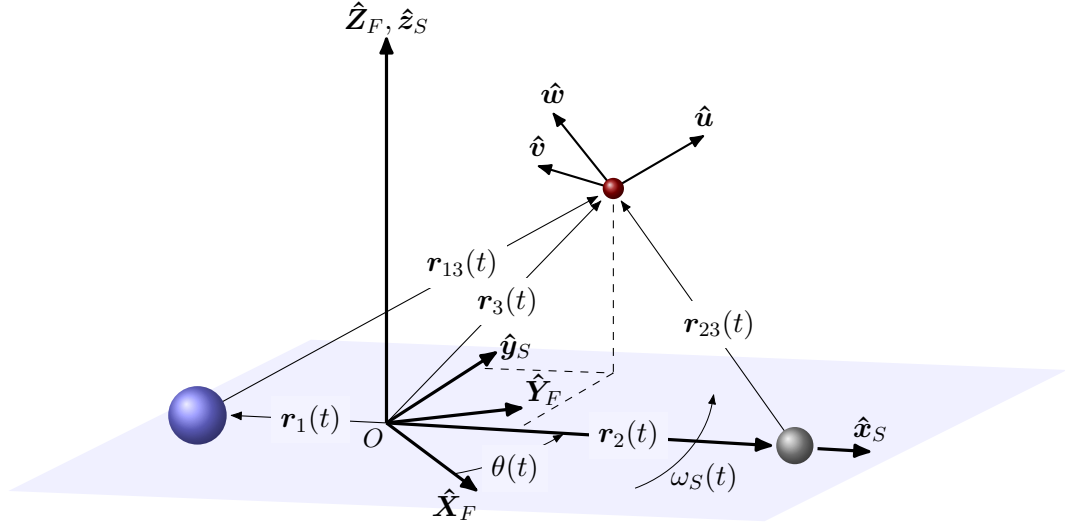


Figure 2.4: Synodic reference system

The two main bodies with masses m_1 and m_2 , the larger and the smaller, respectively, rotate around the barycenter formed by these bodies' system. It is possible to define an inertial RF $\{\hat{X}_F, \hat{Y}_F, \hat{Z}_F\}$ ¹ and a rotating non-inertial RF, also called the synodic reference system $\{\hat{x}_S, \hat{y}_S, \hat{z}_S\}$ ², which follows the motion of the primary bodies that rotate with their angular velocity ω_S . This last one is centered in the barycenter of the system, with the \hat{x}_S axis that coincides with the line which connects the two primary bodies, the \hat{z}_S is perpendicular to the plane where the orbit of the two primary bodies lies, and the \hat{y}_S completes the right hand triad.

In the 3BP, the third body is free to move in space under the gravitational influence of the two main bodies. However, to transition to the Restricted Three-Body Problem (R3BP) and subsequently to the circular Restricted Three-Body Problem (CR3BP), certain assumptions must be made. The shift to R3BP is based on the assumption that the mass of the third body is negligible, as is often the case with spacecraft. For example, in the Sun-Earth-Moon system mentioned earlier, where the Moon acts as a tertiary body, its gravitational influence, although much smaller than the ones of the other two bodies, still affects its relative motion. Therefore, in the R3BP, the third body has no influence on the primary bodies but is solely influenced by them[19].

The assumption that allows the transition from R3BP to CR3BP deals with the orbits of the two main bodies relative to the center of mass of the system. A

¹The subscript F indicates fixed reference system.

²The subscript S indicates synodic reference system.

position vector \mathbf{r}_{ij} with a double subscript denotes the position of the j -th body with respect to i -th body, where \mathbf{r}_i is defined relative to the origin of the RF. Defining μ^* as the sum of the two respective gravitational parameters of the two main bodies, it is possible to define the mean dimensional motion of the binary system as

$$n(t) = \sqrt{\frac{\mu^*}{r_{12}(t)^3}} \quad (2.19)$$

Hence, it is possible to derive the angle θ , function of time, between the fixed reference system and the synodic reference system

$$\theta(t) = n(t)t \quad (2.20)$$

where t is the elapsed time in seconds. In general, both the mean dimensional motion and the theta angle exhibit roto-pulsating behavior due to the time-varying distance between the two primaries. Indeed, when ephemerides are used in the analyses or the eccentricity of Keplerian orbits is considered, these quantities become time-dependent. The transition to CR3BP is achieved by assuming that the orbits of the primaries are circular Keplerian orbits around the center of mass of the system. In this further simplification, the distance between the two primaries remains constant over time, therefore the dimensional mean motion remains constant, and the change in theta is also constant with a velocity equal to ω_S .

A direct non-dimensionalization approach based on the characteristic quantities of length, mass, and time is considered advantageous[17, 25] because it improves the equations for numerical integration and facilitates the comparison of solutions for different three-body systems. The characteristic length l^* is the fixed average distance between the two primary bodies

$$l^* = r_1 + r_2 \quad (2.21)$$

the characteristic mass m^* of the system is the sum of the primaries masses

$$m^* = m_1 + m_2 \quad (2.22)$$

while the characteristic time t^* is not directly imposed, it results from the imposition of the non-dimensional universal gravitational constant to equal one in the formulation of Kepler's third law, from which it is derived

$$\mathcal{T}^* = \sqrt{\frac{(l^*)^3}{Gm^*}} \quad (2.23)$$

thus, the non-dimensional quantities for distance, mass, and time in CR3BP are as follows

$$\rho_{12} = \frac{r_{12}}{l^*} = 1 \quad (2.24a)$$

$$\mu = \frac{m_2}{m^*} \quad (2.24b)$$

$$\tau = \frac{\mathcal{T}}{\mathcal{T}^*} = 2\pi \quad (2.24c)$$

from which the non-dimensional relationships between the masses are obtained

$$\mu = \frac{\mu_2}{\mu^*} \quad 1 - \mu = \frac{\mu_1}{\mu^*} \quad (2.25)$$

analogously, the position of the system's center of mass relative to most massive main body

$$\rho_{CG} = \frac{\sum \rho_i \mu_i}{\sum \mu_i} = \mu \quad (2.26)$$

thus

$$\rho_1 = \frac{r_1}{l^*} = -\mu \quad (2.27a)$$

$$\rho_2 = \frac{r_2}{l^*} = 1 - \mu \quad (2.27b)$$

2.3.1 Equation of Motion

Starting from Newton's Second Law, the following compact form of the Equations of Motion (EOM) is obtained

$$\ddot{\mathbf{r}} = - \sum_{\substack{i=1 \\ i \neq j}}^n \frac{\mu_i}{r_{ij}^2} \frac{\mathbf{r}_{ij}}{r_{ij}} \quad (2.28)$$

where \mathbf{r}_{13} and \mathbf{r}_{23} are the position vectors of the spacecraft with respect to the main bodies defined as

$$\mathbf{r}_{i3} = \mathbf{r}_3 - \mathbf{r}_i \quad i = 1,2 \quad (2.29)$$

For clarity, the subscript 3 will be omitted for spacecraft only. Projecting the equations of motion in the synodic RF directions gives

$$\ddot{\mathbf{x}} = -\frac{\mu_1}{r_{13}^3}(x - x_1) - \frac{\mu_2}{r_{23}^3}(x - x_2) \quad (2.30a)$$

$$\ddot{\mathbf{y}} = -\frac{\mu_1}{r_{13}^3}y - \frac{\mu_2}{r_{23}^3}y \quad (2.30b)$$

$$\ddot{\mathbf{z}} = -\frac{\mu_1}{r_{13}^3}z - \frac{\mu_2}{r_{23}^3}z \quad (2.30c)$$

with the relative position vectors

$$r_{i3} = \sqrt{(x - x_i)^2 + y^2 + z^2} \quad (2.31)$$

In order to project the EOMs into the inertial reference system, it is necessary to first recall the transport theorem for a generic variable f .

$${}^F \frac{df}{dt} = {}^R \frac{df}{dt} + {}^{R/F} \boldsymbol{\omega} \times {}^R f \quad (2.32)$$

where the prescripts F and R indicate the fixed or rotating reference system, respectively, to which the parameter in question is evaluated, while R/F indicates that the quantity is measured in the rotating RF relative to the inertial RF. Finally, the velocity in the inertial reference system is

$${}^F \dot{\mathbf{r}} = \frac{{}^F d\mathbf{r}}{dt} = \frac{{}^R d\mathbf{r}}{dt} + {}^{R/F} \boldsymbol{\omega}_S \times {}^R \mathbf{r} \quad (2.33)$$

The acceleration, on the other hand, can be written as follows:

$$\begin{aligned} {}^F \ddot{\mathbf{r}} &= \frac{{}^F d\dot{\mathbf{r}}}{dt} = \frac{{}^R d({}^F \dot{\mathbf{r}})}{dt} + {}^{R/F} \boldsymbol{\omega}_S \times {}^F \dot{\mathbf{r}} \\ &= \frac{{}^R d}{dt} \left({}^R \dot{\mathbf{r}} + {}^{R/F} \boldsymbol{\omega}_S \times {}^R \mathbf{r} \right) + {}^{R/F} \boldsymbol{\omega}_S \times \left({}^R \dot{\mathbf{r}} + {}^{R/F} \boldsymbol{\omega}_S \times {}^R \mathbf{r} \right) \\ &= {}^R \ddot{\mathbf{r}} + {}^{R/F} \dot{\boldsymbol{\omega}}_S \times {}^R \mathbf{r} + {}^{R/F} \boldsymbol{\omega}_S \times {}^R \dot{\mathbf{r}} + {}^{R/F} \boldsymbol{\omega}_S \times {}^R \dot{\mathbf{r}} + {}^{R/F} \boldsymbol{\omega}_S \times \left({}^{R/F} \boldsymbol{\omega}_S \times {}^R \mathbf{r} \right) \\ {}^F \ddot{\mathbf{r}} &= {}^R \ddot{\mathbf{r}} + {}^{R/F} \dot{\boldsymbol{\omega}}_S \times {}^R \mathbf{r} + 2 \left({}^{R/F} \boldsymbol{\omega}_S \times {}^R \dot{\mathbf{r}} \right) + {}^{R/F} \boldsymbol{\omega}_S \times \left({}^{R/F} \boldsymbol{\omega}_S \times {}^R \mathbf{r} \right) \end{aligned} \quad (2.34)$$

The first term on the right side of the Equation (2.34) represents the acceleration in the synodic reference frames, while the remaining three terms are commonly called to as tangential, centrifugal, and Coriolis acceleration. Under the assumptions of CR3BP, where circular orbits are considered, and consequently, no variations of $\boldsymbol{\omega}_S$ occur, the terms for tangential and centripetal accelerations are zero.

Given that

$$\boldsymbol{\omega}_S = \omega_S \hat{\mathbf{z}}_S \quad (2.35)$$

and taking into account the Kleper's third law

$$\omega_S = \frac{\mu_1 + \mu_2}{r_{12}^3} \quad (2.36)$$

expanding the equation (2.33) and explicitly expressing the quantities for the general case of 3BP result in the following velocity components

$$\begin{aligned} {}^F \dot{\mathbf{r}} &= (\dot{x} \hat{\mathbf{x}}_S + \dot{y} \hat{\mathbf{y}}_S + \dot{z} \hat{\mathbf{z}}_S) + \begin{vmatrix} \hat{\mathbf{x}}_S & \hat{\mathbf{y}}_S & \hat{\mathbf{z}}_S \\ 0 & 0 & \omega_S \\ x & y & z \end{vmatrix} \\ &= (\dot{x} \hat{\mathbf{x}}_S + \dot{y} \hat{\mathbf{y}}_S + \dot{z} \hat{\mathbf{z}}_S) + [(-y\omega_S) \hat{\mathbf{x}}_S - (-x\omega_S) \hat{\mathbf{y}}_S + (0) \hat{\mathbf{z}}_S] \\ {}^F \dot{\mathbf{r}} &= (\dot{x} - y\omega_S) \hat{\mathbf{x}}_S + (\dot{y} + x\omega_S) \hat{\mathbf{y}}_S + \dot{z} \hat{\mathbf{z}}_S \end{aligned} \quad (2.37)$$

Neglecting the prescript R and R/F in the last line of the equation (2.34) for the sake of clarity, the acceleration shows the following components

$$\begin{aligned} {}^F \ddot{\mathbf{r}} &= \ddot{\mathbf{r}} + \dot{\boldsymbol{\omega}}_S \times \mathbf{r} + 2\boldsymbol{\omega}_S \times \dot{\mathbf{r}} + \boldsymbol{\omega}_S \times (\boldsymbol{\omega}_S \times \mathbf{r}) \\ &= \ddot{\mathbf{r}} + \begin{vmatrix} \hat{\mathbf{x}}_S & \hat{\mathbf{y}}_S & \hat{\mathbf{z}}_S \\ 0 & 0 & \dot{\omega}_S \\ x & y & z \end{vmatrix} + 2 \begin{vmatrix} \hat{\mathbf{x}}_S & \hat{\mathbf{y}}_S & \hat{\mathbf{z}}_S \\ 0 & 0 & \omega_S \\ \dot{x} & \dot{y} & \dot{z} \end{vmatrix} + \boldsymbol{\omega}_S \times \begin{vmatrix} \hat{\mathbf{x}}_S & \hat{\mathbf{y}}_S & \hat{\mathbf{z}}_S \\ 0 & 0 & \omega_S \\ x & y & z \end{vmatrix} \\ &= (\ddot{x} - 2\dot{y}\omega_S - y\dot{\omega}_S) \hat{\mathbf{x}}_S + (\ddot{y} + \dot{x}\omega_S - x\dot{\omega}_S) \hat{\mathbf{y}}_S + (\ddot{z}) \hat{\mathbf{z}}_S + \begin{vmatrix} \hat{\mathbf{x}}_S & \hat{\mathbf{y}}_S & \hat{\mathbf{z}}_S \\ 0 & 0 & \omega_S \\ -y\omega_S & x\omega_S & 0 \end{vmatrix} \\ &= (\ddot{x} - 2\dot{y}\omega_S - y\dot{\omega}_S - x\omega_S^2) \hat{\mathbf{x}}_S + (\ddot{y} + 2\dot{x}\omega_S + x\dot{\omega}_S - y\omega_S^2) \hat{\mathbf{y}}_S + \ddot{z} \hat{\mathbf{z}}_S \end{aligned} \quad (2.38)$$

Equalizing the corresponding components of equations 2.30 and 2.38

$$\ddot{x} - 2\dot{y}\omega_S - y\dot{\omega}_S - x\omega_S^2 = -\frac{\mu_1}{r_{13}^3}(x - x_1) - \frac{\mu_2}{r_{23}^3}(x - x_2) \quad (2.39a)$$

$$\ddot{y} + 2\dot{x}\omega_S + x\dot{\omega}_S - y\omega_S^2 = -\frac{\mu_1}{r_{13}^3}y - \frac{\mu_2}{r_{23}^3}y \quad (2.39b)$$

$$\ddot{z} = -\frac{\mu_1}{r_{13}^3}z - \frac{\mu_2}{r_{23}^3}z \quad (2.39c)$$

Consider the classical non-dimensionalization of CR3BP as follows:

$$\xi = \frac{x}{l^*} \quad (2.40a)$$

$$\eta = \frac{y}{l^*} \quad (2.40b)$$

$$\zeta = \frac{z}{l^*} \quad (2.40c)$$

$$\rho = \frac{r}{l^*} \quad (2.40d)$$

By employing the assumptions of CR3BP, namely $\omega_S = 1$ and hence $\dot{\omega} = 0$, we obtain the following set of non-dimensional ODEs for the cartesian components

$$\ddot{\xi} - 2\dot{\eta} - \xi = -\frac{1-\mu}{\rho_{13}^3}(\xi + \mu) - \frac{\mu}{\rho_{23}^3}[\xi - (1-\mu)] \quad (2.41a)$$

$$\ddot{\eta} + 2\dot{\xi} - \eta = -\frac{1-\mu}{\rho_{13}^3}\eta - \frac{\mu}{\rho_{23}^3}\eta \quad (2.41b)$$

$$\ddot{\zeta} = -\frac{1-\mu}{\rho_{13}^3}\zeta - \frac{\mu}{\rho_{23}^3}\zeta \quad (2.41c)$$

2.3.2 Jacobi Constant

The Jacobi integral is the sole pseudo-integral of motion that exists in the CR3BP within the rotating synodic RF. It is especially important for investigating the stability and accessible regions influenced by the third body in the binary system.

Defining the potential function U in the inertial RF as

$${}^F U = \sum_{i=1}^2 \frac{\mu_i}{r_{i3}} \quad (2.42)$$

where the index 3 indicates the spacecraft and i denotes the i -th gravitational body. In order to write the same potential in the rotating RF, it is necessary to consider the centrifugal potential as well and thus

$${}^R U = \frac{\mu_1}{r_{13}} + \frac{\mu_2}{r_{23}} + \frac{1}{2}\omega_S(x^2 + y^2) \quad (2.43)$$

non-dimensionalizing gives the following expression of pseudopotential

$${}^R \mathcal{U} = \frac{1-\mu}{\rho_{13}} + \frac{\mu}{\rho_{23}} + \frac{1}{2}(\xi^2 + \eta^2) \quad (2.44)$$

Deriving with respect to non-dimensional coordinates

$$\frac{\partial \mathcal{W}}{\partial \xi} = \xi - \frac{1-\mu}{\rho_{13}^3}(\xi + \mu) - \frac{\mu}{\rho_{23}^3}[\xi - (1-\mu)] \quad (2.45a)$$

$$\frac{\partial \mathcal{W}}{\partial \eta} = \eta - \frac{1-\mu}{\rho_{13}^3}\eta - \frac{\mu}{\rho_{23}^3}\eta \quad (2.45b)$$

$$\frac{\partial \mathcal{W}}{\partial \zeta} = -\frac{1-\mu}{\rho_{13}^3}\zeta - \frac{\mu}{\rho_{23}^3}\zeta \quad (2.45c)$$

Comparing equation (2.45) and (2.41) yields

$$\ddot{\xi} - 2\dot{\eta} = \frac{\partial \mathcal{W}}{\partial \xi} \quad (2.46a)$$

$$\ddot{\eta} + 2\dot{\xi} = \frac{\partial \mathcal{W}}{\partial \eta} \quad (2.46b)$$

$$\ddot{\zeta} = \frac{\partial \mathcal{W}}{\partial \zeta} \quad (2.46c)$$

Focusing again on the dimensional equations (2.39), multiplying each component of equation by $2\dot{x}, 2\dot{y}, 2\dot{z}$, and summing them gives:

$$2\ddot{x}\dot{x} + 2\ddot{y}\dot{y} + 2\ddot{z}\dot{z} - 2\omega_S^2(\dot{x}\dot{x} + \dot{y}\dot{y}) = 2\dot{x}\frac{\partial U}{\partial x} + 2\dot{y}\frac{\partial U}{\partial y} + 2\dot{z}\frac{\partial U}{\partial z} = 2\frac{dU}{dt} \quad (2.47)$$

Integrating the previous equation results in Jacobi's integral

$$\dot{x}^2 + \dot{y}^2 + \dot{z}^2 = V^2 = 2U - J_C \quad (2.48)$$

The term on the left side of the equation corresponds to the square of the velocity V^2 . On the right side, the first term contains the pseudopotential U , which includes the $\omega_S^2(x^2 + y^2)$ term, and the second term is J_C , commonly known as Jacobi's constant. This constant can be understood as analogous to the inverse of the mechanical specific energy \mathcal{E} ; the greater the value of J_C , the less energy the spacecraft possesses in the synodic system. In its non-dimensional form, the Jacobian integral equation appears as

$$\dot{\xi}^2 + \dot{\eta}^2 + \dot{\zeta}^2 = v^2 = 2\mathcal{W} - \mathcal{J}_C \quad (2.49)$$

2.3.3 Equilibrium Solutions

Although nowadays there is still no analytical solution for the complete set of ODEs (2.46), Joseph-Louis Lagrange demonstrated the existence of equilibrium points,

which are named after him[26]. Therefore, following Lagrange's approach, first step is set the gradient vector of the pseudopotential function equal to zero, which means imposing zero velocity and acceleration in the rotating reference system.

$$\nabla \mathcal{U} = 0 \quad (2.50)$$

in scalar form

$$\frac{\partial \mathcal{U}}{\partial \xi} = \xi - \frac{1-\mu}{\rho_{13}^3} (\xi + \mu) - \frac{\mu}{\rho_{23}^3} [\xi - (1-\mu)] = 0 \quad (2.51a)$$

$$\frac{\partial \mathcal{U}}{\partial \eta} = \eta - \frac{1-\mu}{\rho_{13}^3} \eta - \frac{\mu}{\rho_{23}^3} \eta = 0 \quad (2.51b)$$

$$\frac{\partial \mathcal{U}}{\partial \zeta} = -\frac{1-\mu}{\rho_{13}^3} \zeta - \frac{\mu}{\rho_{23}^3} \zeta = 0 \quad (2.51c)$$

A set of coordinates $\{\xi_i, \eta_i, \zeta_i\}$ that satisfy the above equations can be determined for each of the five Lagrangian points (LPs). The last equation is immediately satisfied by setting $\zeta = 0$, indicating that all equilibrium points lie in the $\hat{\xi}_S - \hat{\eta}_S$ plane. Setting η and ζ to zero yields a quintic equation as a function of ξ . The roots, three of which are real, do not exist in closed form and must be computed numerically. In the context of the CR3BP problem, the equilibrium solutions are commonly referred to as libration points. Since the first three lie on the ξ -axis, they are specifically called collinear libration points. Euler was the first to identify these solutions in 1765. The other two equilibrium solutions, first found by Lagrange, can be determined by setting the distances of the primaries with respect to the spacecraft equal to one, namely $\rho_{13} = \rho_{23} = 1$; these points are also known as equilateral libration points or triangular libration point.

Figure 2.5 shows the positions of the five LPs in the Earth-Moon system. As mentioned before, it is possible to find the collinear points along the ξ -axis and the equilateral libration points at the vertices of an equilateral triangle, with the distance between the primaries as its base. L_4 and L_5 's radial positions are depicted by the dashed circle while L_3 is located outside this zone. The smaller primary body, the Moon in this case, is located between L_1 and L_2 . It seems that these points are equidistant from the Moon but in reality L_2 is little further away. The dotted circles represent the orbits of the primaries concerning the barycenter when observed from an inertial RF. Given that the center of mass of such a system is 4760 km from the center of the Earth, it resides inside the Earth at 73% of its radius[21].

The complete form for the numerical calculation of the position of collinear points is[27]:

$$\xi^5 \mp (3-\mu)\xi^4 + (3-2\mu)\xi^3 - \mu\xi^2 \pm 2\mu\xi - \mu = 0 \quad (2.52)$$

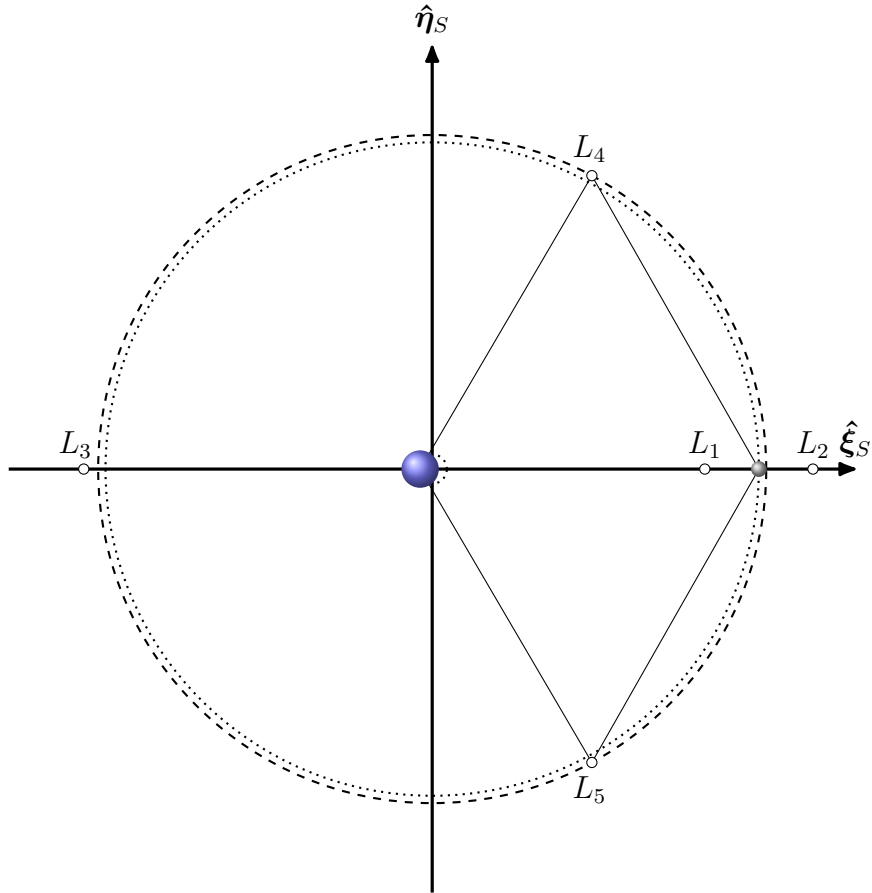


Figure 2.5: Lagrangian Points in Earth-Moon synodic RF

Supposing that the smaller primary body is at least an order of magnitude smaller than the larger primary, the first two LPs are located approximately at the same distance relative to the smaller primary, close to the radius of Hill's sphere

$$x_{Li} \approx \mp r_{12} \sqrt{\frac{\mu_2}{3\mu_1}} \quad i = 1, 2$$

Among the five Lagrangian points, L1, L2, and L3 are considered unstable, while L4 and L5 are stable. Points L4 and L5 exhibit stability as long as the mass of the primary body is at least 24.96 times of the one of the secondary body. When a body positioned at L4 or L5 starts to drift from this point, accelerating away, the Coriolis force comes into play, correcting its trajectory and maintaining a stable orbit around the Lagrangian point. For additional details on the stability of these points, refer to [28–30].

2.3.4 Zero Velocity Surfaces

A significant outcome derived from the previous treatment of the Jacobi integral, wherein the relative velocity in the synodic RF is set to zero, is the concept of Zero-Velocity Surfaces (ZVS). When a specific value of the Jacobi constant is given, the equation for a surface representing the boundaries that the third body, the spacecraft, cannot cross while moving within an allowed region is automatically provided.

$$\mathcal{J}_C = 2\mathcal{U} = 2 \left(\frac{1-\mu}{\rho_1} + \frac{\mu}{\rho_2} \right) + (\xi^2 + \eta^2) \quad (2.53)$$

By inverting the signs in equation (2.49), the quantities resemble those of energy in the (2BP), thus the representation of these surfaces aligns to be similar to what is expected for potential energy. Figure 2.6 shows these surface for the Earth-Moon system.

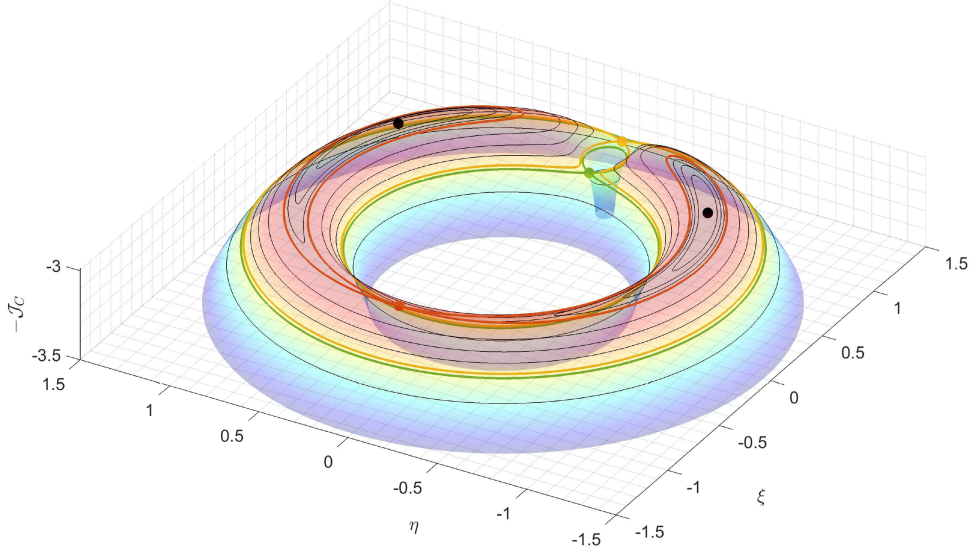


Figure 2.6: 3D Earth-Moon Zero-Velocity Surfaces at L1 energy. Credits:[17]

A spacecraft traveling in close proximity to the primary body at a low speed, near orbital velocity, and thus possessing a low initial energy value and consequently a high \mathcal{J}_C value, will be confined to a circle-like zone (Figure 2.7a). As the initial energy (both kinetic and potential energy) increases, \mathcal{J}_C becomes less positive. Consequently, more accessible regions for the spacecraft broaden, allowing it to reach these regions with zero velocity. The first encountered region is one that intersects L1 (Figure 2.7b), creating a corridor to the Moon, the ZVS level shown in Figure 2.6 in green. Further energy increases open up additional areas, including

those behind the Moon (Figure 2.7c). A spacecraft able to reach the L2 ZVS has enough energy to escape the Earth-Moon system along specific trajectories leveraging the gravitational pull of the primary body. As the energy continues to increase, the corridor widens until escape in the opposite direction from the Moon becomes possible (Figure 2.7d), corresponding to the level of L3, outlined in red in Figure 2.6. Finally, when the spacecraft can access L4 and L5, represented by black dots, it will have enough energy to cross any region, therefore there will be no more prohibited areas (Figure 2.7e and Figure 2.7f).

The same concepts are shown in Figure 2.8, where all regions in white correspond to $\mathcal{I}_C > \mathcal{I}_{C,L1}$, orange regions to $\mathcal{I}_{C,L2} < \mathcal{I}_C < \mathcal{I}_{C,L1}$, yellow regions to $\mathcal{I}_{C,L3} < \mathcal{I}_C < \mathcal{I}_{C,L2}$, and red regions to $\mathcal{I}_{C,L4} = \mathcal{I}_{C,L5} < \mathcal{I}_C < \mathcal{I}_{C,L3}$.

	ξ	η	ζ	\mathcal{I}_C
L_1	0.83740242	0.00000000	0.00000000	3.188326
L_2	1.15618808	0.00000000	0.00000000	3.172147
L_3	-1.00506193	0.00000000	0.00000000	3.012145
L_4	0.48785136	0.86602540	0.00000000	2.987999
L_5	0.48785136	-0.86602540	0.00000000	2.987999

Table 2.1: Positions and Jacobi Constants of the Earth-Moon system, synodic RF. Credits:[17]

Table 2.1 presents the coordinates and respective Jacobi Constants for each of the five Lagrangian points in the Earth-Moon system, as discussed in this paper. The numbering of the LPs is based on the decreasing values of the \mathcal{I}_C , reflecting the order in which these points become accessible.

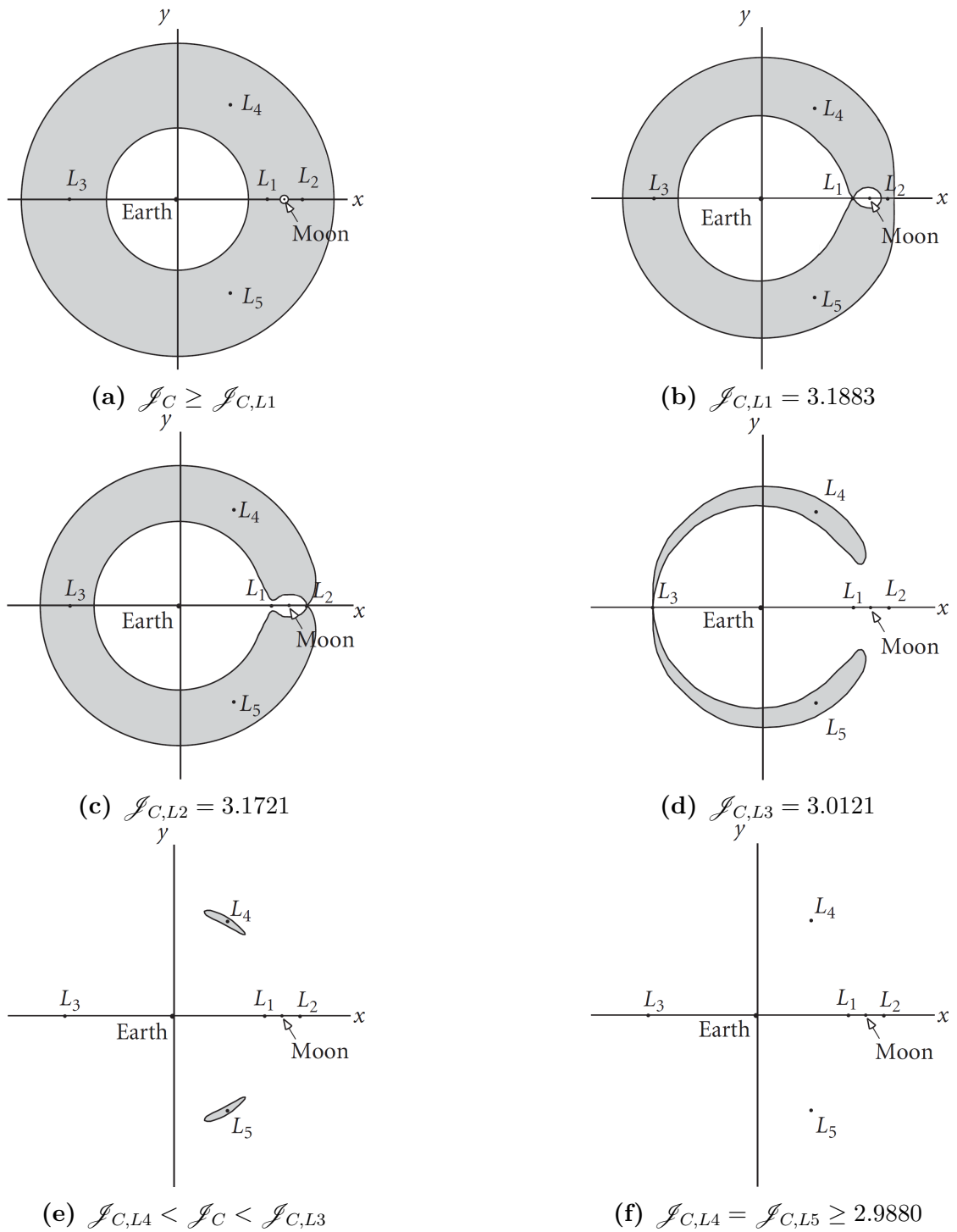


Figure 2.7: Forbidden regions in the Earth-Moon system for decreasing values of Jacobi's constant. Credits:[21]

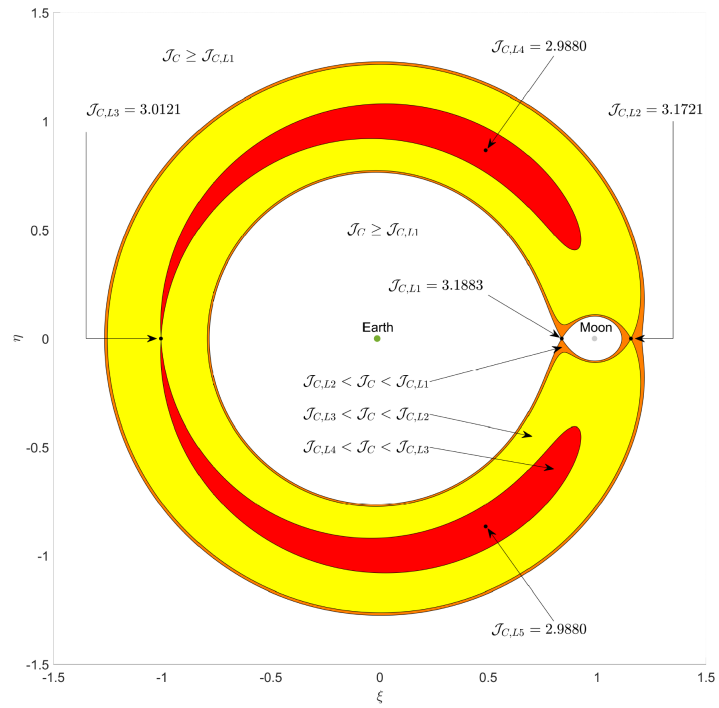


Figure 2.8: Earth-Moon Zero-Velocity Surfaces at LPs energy. Credits:[17]

2.4 N-Body Problem

Although the CR3BP is a very useful tool for performing preliminary analysis and considerations in multi-body dynamical systems, achieving high-fidelity trajectory optimization requires the use of a more accurate dynamical model that describe the solar system more more closely, taking into account the effects and perturbations due to the other bodies and phenomena in the solar system. In this dissertation, the JPL DE430 planetary ephemerides are utilized in the NBP dynamical model. This model considers four gravitational bodies (Sun, Earth, Moon, and spacecraft) and incorporates various perturbations and effects, which will be thoroughly discussed in Section 2.6.

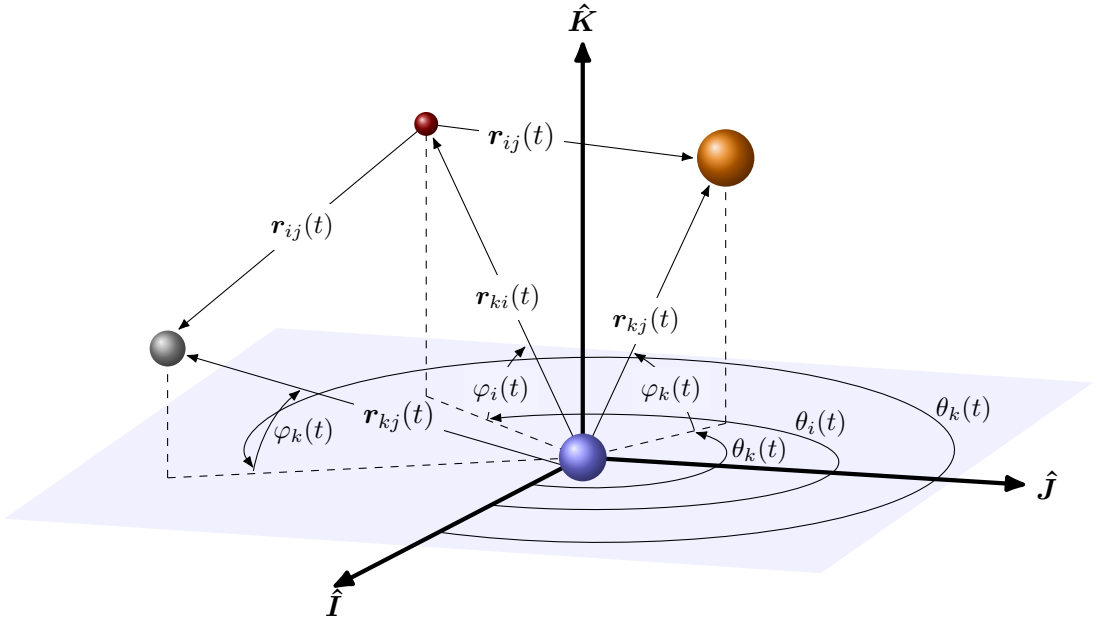


Figure 2.9: N-Body Problem EME2000 RF

Unlike in the 3BP scenario, it is more convenient to employ a non-rotating reference system when dealing with the equations of motion in the NBP. In this study, trajectories in the ephemeris model are computed with Earth as the central body and in light of the above, the reference system used is EME2000. As illustrated in Figure 2.9, the central body is denoted as the k -th among the n bodies, the spacecraft is denoted as i , and all other bodies are represented as j -th.

In a generic inertial RF, the acceleration experienced by the spacecraft is described by Equation 2.28, which for the sake of clarity is given again below

$$\ddot{\mathbf{r}}_i = - \sum_{\substack{j=1 \\ j \neq i}}^n \frac{\mu_j}{r_{ji}^2} \frac{\mathbf{r}_{ji}}{r_{ji}} \quad (2.54)$$

The formulation is most useful when expressed relative to the center of mass of the central body, manifesting as the following second-degree differential equation[19]

$$\ddot{\mathbf{r}}_{ki} = - \frac{(\mu_i + \mu_k)}{r_{ki}^3} \mathbf{r}_{ki} + \sum_{\substack{j=1 \\ j \neq i, k}}^n \mu_j \left(\frac{\mathbf{r}_{ij}}{r_{ij}^3} - \frac{\mathbf{r}_{kj}}{r_{kj}^3} \right) \quad (2.55)$$

It is worth noting that although all quantities of the NBP, including positions and velocities, are time-dependent, the notation (t) denoting dependence in time is omitted from the NBP equations for the sake of simplicity.

The position vectors \mathbf{r}_{kj} obtained from the DE430 JPL ephemerides are given in rectangular coordinates $\{x_{kj}, y_{kj}, z_{kj}\}$ with respect to the Earth in the ICRF, namely $\mathbf{r}_{kj} = x_{kj}\hat{\mathbf{I}} + y_{kj}\hat{\mathbf{J}} + z_{kj}\hat{\mathbf{K}}$. Since, as mentioned in Section 2.1.1, the difference between ICRF and EME2000 is negligible, the second one is used. Instead, the spacecraft position vector \mathbf{r}_{ki} is computed during the trajectory analysis process. The relative position vector \mathbf{r}_{ij} can be obtained by a simple subtraction of vectors as follows

$$\mathbf{r}_{ij} = \mathbf{r}_{kj} - \mathbf{r}_{ki} \quad (2.56)$$

In general, for questions related to numerical accuracy, a method similar to that used in CR3BP is employed, namely non-dimensionalizing the variables, masses and lengths, with respect to characteristic quantities[17]. For the sake of completeness, these characteristic quantities, for the Earth-Moon system, are shown in Table 2.2.

Quantity	Earth-Moon
l^*	r_{EM}
μ^*	$\mu_E + \mu_M$
Derived	
\mathcal{I}_C	$\sqrt{\frac{(l^*)^3}{\mu^*}}$
V^*	$\frac{l^*}{\mathcal{I}^*}$

Table 2.2: Characteristic quantities in NBP for Earth-Moon system

Thus, the non-dimensionalized formulation of Equation 2.55 is as follows

$$\ddot{\mathbf{r}}_{ki} = -\frac{(\check{\mu}_i + \check{\mu}_k)}{\check{r}_{ki}^3} \check{\mathbf{r}}_{ki} + \sum_{\substack{j=i \\ j \neq i, k}}^n \check{\mu}_j \left(\frac{\check{\mathbf{r}}_{ij}}{\check{r}_{ij}^3} - \frac{\check{\mathbf{r}}_{kj}}{\check{r}_{kj}^3} \right) \quad (2.57)$$

where the generic position vector is

$$\check{\mathbf{r}}_{kj} = \frac{\mathbf{r}_{kj}}{l^*} = \check{x}_{kj} \hat{\mathbf{I}} + \check{y}_{kj} \hat{\mathbf{J}} + \check{z}_{kj} \hat{\mathbf{K}} \quad (2.58)$$

2.5 Equation of Motion in Spherical Coordinates

The set of Equations of Motion (2.9) can be formulated in cardinal directions. In particular, the position of the spacecraft is expressed in polar coordinates in the EME2000 reference system, by its radius r , its latitude φ and its longitude θ . Instead, the velocity is projected onto the spacecraft centred topocentric ZEN RF, thus with components: a radial (Zenith), a tangential (East) and a normal (North)[17].

$$\frac{dr}{dt} = u \quad (2.59a)$$

$$\frac{d\theta}{dt} = \frac{v}{r \cos \varphi} \quad (2.59b)$$

$$\frac{d\varphi}{dt} = \frac{w}{r} \quad (2.59c)$$

$$\frac{du}{dt} = -\frac{\mu}{r^2} + \frac{v^2}{r} + \frac{w^2}{r} + \frac{T_u}{m} + (a_P)_u \quad (2.59d)$$

$$\frac{dv}{dt} = -\frac{uv}{r} + \frac{vw}{r} \tan \varphi + \frac{T_v}{m} + (a_P)_v \quad (2.59e)$$

$$\frac{dw}{dt} = -\frac{uw}{r} - \frac{v^2}{r} \tan \varphi + \frac{T_w}{m} + (a_P)_w \quad (2.59f)$$

$$\frac{dm}{dt} = -\frac{T}{c} \quad (2.59g)$$

where the projections of the thrust vector is

$$T_u = T \sin \alpha_T \quad (2.60a)$$

$$T_v = T \cos \alpha_T \cos \beta_T \quad (2.60b)$$

$$T_w = T \cos \alpha_T \sin \beta_T \quad (2.60c)$$

in which α_T is the in-plane thrust angle in the ZEN RF and β_T is the out-plane thrust angle.

2.6 Perturbing Accelerations

The dynamic model incorporates three primary perturbative accelerations affecting the spacecraft's motion: those caused by the gravity of the Sun and Moon, solar radiation pressure, and the Earth's non-sphericity. Consequently, the vector comprising all perturbative accelerations in Equation(2.9) is composed of:

$$\mathbf{a}_P = \mathbf{a}_{lsp} + \mathbf{a}_{SRP} + \mathbf{a}_J \quad (2.61)$$

The formulation of these perturbative accelerations has been extensively discussed in various textbooks, including [16, 17, 19, 31] which can be consulted for more specific details.

2.6.1 Lunisolar Effect

Perturbations from lunisolar effects have been widely discussed over time because they are crucial in forecasting deviations in specific orbits, especially highly elliptical ones, from expected behavior[17, 31, 32].

The positions of the Sun and Moon are determined through the DE430 JPL ephemerides[22], supplying the body position vector \mathbf{r}_{Eb} in rectangular coordinates relative $\{x_{Eb}, y_{Eb}, z_{Eb}\}$ to the Earth, the central body, in the ICRF. Note again that ICRF and EME2000 are used interchangeably in this thesis due to their negligible difference. The subscript b is used to indicate a generic body, hence with $b = s$ for the Sun and $b = l$ for the Moon.

$$\mathbf{r}_{Eb} = x_{Eb}\hat{\mathbf{I}} + y_{Eb}\hat{\mathbf{J}} + z_{Eb}\hat{\mathbf{K}} \quad (2.62)$$

By applying the rotation defined in Equation (2.8), the coordinates in the spacecraft topocentric frame are obtained

$$(r_{Eb})_u = x_b \cos \theta \cos \varphi + y_b \sin \theta \cos \varphi + z_b \sin \varphi \quad (2.63a)$$

$$(r_{Eb})_v = -x_b \sin \theta + y_b \cos \theta \quad (2.63b)$$

$$(r_{Eb})_w = -x_b \cos \theta \sin \varphi - y_b \sin \theta \sin \varphi + z_b \cos \varphi \quad (2.63c)$$

The perturbative acceleration experienced by the spacecraft \mathbf{a}_{bg} , caused by the third body with gravitational parameter μ_b and position vector with respect to the Earth \mathbf{r}_{Eb} , is equivalent to the gravitational accelerations exerted by the perturbing body on the spacecraft \mathbf{a}_{SCb} and on the Earth \mathbf{a}_{Eb} , as follows

$$\mathbf{a}_{bg} = \mathbf{a}_{SCb} - \mathbf{a}_{Eb} = -\frac{\mu_b}{r_{bSC}^3}\mathbf{r}_{bSC} - \frac{\mu_b}{r_{Eb}^3}\mathbf{r}_{Eb} \quad (2.64)$$

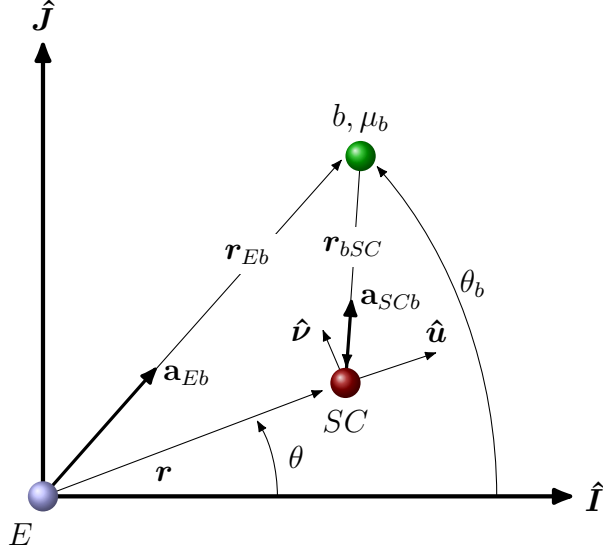


Figure 2.10: Representation of third-body gravitational perturbation

where the spacecraft relative position vector with respect to the perturbing body is defined as $\mathbf{r}_{bSC} = \mathbf{r} - \mathbf{r}_{Eb}$. Projecting the acceleration in the topocentric RF gives the following perturbing components

$$(\mathbf{a}_{bg})_u = \frac{\mu_b}{r_{bSC}^3} [(r_{Eb})_u - r] - \frac{\mu_b}{r_{Eb}^3} (r_{Eb})_u \quad (2.65a)$$

$$(\mathbf{a}_{bg})_v = \frac{\mu_b}{r_{bSC}^3} (r_{Eb})_v - \frac{\mu_b}{r_{Eb}^3} (r_{Eb})_v \quad (2.65b)$$

$$(\mathbf{a}_{bg})_w = \frac{\mu_b}{r_{bSC}^3} (r_{Eb})_w - \frac{\mu_b}{r_{Eb}^3} (r_{Eb})_w \quad (2.65c)$$

with

$$r_{bSC} = \sqrt{[r - (r_{Eb})_u]^2 + (r_{Eb})_v^2 + (r_{Eb})_w^2} \quad (2.66)$$

Note that, since gravity depends only on position, the perturbing acceleration depends only on r, θ, φ as well as time. The lunisolar perturbation results from the sum of the gravitational disturbances caused by both the Moon ($b = l$) and the Sun ($b = s$).

In scenarios where the third body is significantly distant compared to the Earth-spacecraft distance, such as the case with the Sun where $\mathbf{r}_{Es} \gg \mathbf{r}$, and coplanarity of the orbits is assumed, a straightforward expression for the tangential and radial components of the perturbative acceleration can be derived[16, 17, 31]

$$(\mathbf{a}_{SC_s} - \mathbf{a}_{E_s}) \cdot \hat{\mathbf{u}} = \frac{3}{2} \frac{\mu_s}{r_{E_s}^3} \{1 + \cos [2(\theta_s - \theta)]\} \quad (2.67a)$$

$$(\mathbf{a}_{SC_s} - \mathbf{a}_{E_s}) \cdot \hat{\mathbf{v}} = \frac{3}{2} \frac{\mu_s}{r_{E_s}^3} \sin [2(\theta_s - \theta)] \quad (2.67b)$$

2.6.2 Solar Radiation Pressure

Solar radiation pressure is the second perturbation considered by the dynamical model used in this thesis. It is related to the force that a photon emitted by the Sun, traveling at the speed of light and therefore having some momentum, exerts when hitting a surface[16, 17, 31].

The physical properties of the spacecraft used in this work are as follows

Quantity	Symbol	Value	Dimension
Mass	m_0	850	kg
Cross-Section Surface	S	5.7	m ²
Surface Reflectivity	η_R	0.7	

Table 2.3: Spacecraft characteristic values

The photon pressure p at generic distance r from the Sun is

$$p = \frac{\mathcal{P}}{4\pi r^2} a_{light} \quad (2.68)$$

where $\mathcal{P} = 1367W/m^2$ is the total power radiated by the Sun, which depends on the inverse square of the distance from the Sun in astronomical units(AU). The photon pressure at $r^* = 1AU$ is $p^* = 4.55682 \cdot 10^6 N/m^2$. Assuming

$$\Gamma = (1 + \eta_R) pS \quad (2.69)$$

the components of acceleration on a spherical body of mass m and cross-section S within a distance from the Sun r_{sSC} result in:

$$(\mathbf{a}_{srp})_u = -\frac{\Gamma}{mr_{sSC}^3} [(r_{Es})_u - r] \quad (2.70a)$$

$$(\mathbf{a}_{srp})_v = -\frac{\Gamma}{mr_{sSC}^3} (r_{Es})_v \quad (2.70b)$$

$$(\mathbf{a}_{srp})_w = -\frac{\Gamma}{mr_{sSC}^3} (r_{Es})_w \quad (2.70c)$$

Similar to the previous case, the SRP is a function of the variables r, θ, φ , but it also depends on the instantaneous mass of the spacecraft, which changes during the propulsive phase of the trajectory. The influence of solar radiation pressure results in an acceleration directed from the Sun to the spacecraft, inversely proportional to the square of the distance between the two bodies. This acceleration, along with the gravitational acceleration from the Sun, exhibits a similar dependence on distance and is parallel but in opposite directions[31]. It is worth noting that the formulation presented here is a simplified version; in fact, it assumes that the surface always faces the Sun.

2.6.3 Earth Asphericity

The Earth's gravitational potential is described by the spherical harmonic Earth Gravitational Model EGM2008[33]; the "tide-free system" is implied in this work, for detailed information please refer to [34]. The potential due to the non-spherical nature of the Earth for a body located at a distance r from the center of the Earth, with longitude θ_{Lo} and latitude φ , is defined as[16, 17, 19, 31]

$$\mathcal{V} = -\frac{\mu_E}{r} \left\{ 1 + \sum_{n=2}^N \left(\frac{r_E}{r} \right)^n \sum_{m=0}^n [C_{nm} \cos(m\theta_{Lo}) + S_{nm} \sin(m\theta_{Lo})] P_{nm} \sin \varphi \right\} \quad (2.71)$$

where μ_E is the gravitational parameter and r_E is the semimajor axis of the Earth ellipsoid.

In this dissertation, associated Legendre functions, P_{nm} , of the eighth order, and spherical harmonic coefficients, C_{nm} and S_{nm} , of the eighth order are implemented. Since nutation and precession are neglected, the Earth's rotation is assumed to be uniform, and thus the Earth's declination and latitude coincide. The Earth's longitude is obtained as

$$\theta_{Lo}(t) = \theta - \theta_G(t) = \theta - [\theta_{Gref} + \omega_E (t - t_{ref})] \quad (2.72)$$

where $\theta_{Gref} = 280.46061837504$ deg is the Greenwich right ascension at the reference time t_{ref} , which is the J2000 epoch, January 1, 2000 at 12:00:00 UTC (51544.5 MJD), and ω_E is determined by assuming a sidereal day equal to 86164.098903690351 s, with the neglect of precession. The perturbing acceleration resulting from the asphericity of the Earth is the gradient of $\Phi = \mathcal{V} + \mu_E/r$, and its components in the topocentric reference system are evaluated as follows

$$(a_J)_u = \frac{\partial \Phi}{\partial r} \tag{2.73a}$$

$$(a_J)_v = \frac{\partial \Phi}{\partial \theta} \frac{1}{r \cos \varphi} \tag{2.73b}$$

$$(a_J)_w = \frac{\partial \Phi}{\partial \varphi} \frac{1}{r} \tag{2.73c}$$

Differentiation with respect to r and θ is uncomplicated, while derivation with respect to φ involves computing the derivatives of the associated Legendre functions, which are obtained recursively by employing the properties of Legendre polynomials. Derivatives are evaluated directly with respect to φ , assuming P_{nm} equal to 0 for $m > n$, gives[31]

$$\begin{cases} P_{n1} & \text{for } m = 0 \\ \left[\frac{P_{n(m+1)} - (n+m)(n-m+1)P_{n(m-1)}}{2} \right] & \text{for } m > 0 \end{cases} \tag{2.74}$$

In the present thesis, escape trajectories from the Lagrangian L2 point of the Earth-Moon binary system are examined, and consequently, the influence of the gravitational model is nearly zero and could be neglected. Nevertheless, the potential model presented here has been implemented in a manner that allows for the evaluation of such perturbations in any future studies that may require it, without the need to modify the code. In the analysis under consideration, however, the influence remains entirely negligible.

Chapter 3

Optimal Trajectories

Dealing with an Optimal Control Problem (OCP) involves finding the optimal control law that maximizes or minimizes a specific index of merit. The optimal trajectory is the one that maximizes the final mass of the spacecraft, given the initial mass, or similarly, is the trajectory that minimizes the mass of propellant used to complete a transfer from an initial point to an end point. The parameters that influence the achievement of the desired target must be appropriately controlled during the trajectory's evolution, ensuring adherence to constraints and maximizing the index of merit. The following chapter is divided into four sections: the first one provides a description of the two main numerical methods, direct and indirect, that can be used to solve OCPs; the second one first describes a generic OCP as a Two-Point Boundary Value Problem (TPBVP), followed by a Multi-Point Boundary Value Problem (MPBVP); the third one shows how the MPBVP is implemented and how it is solved through the single-shooting method; in the last one is presented the application to the case study.

3.1 Direct and Indirect Numerical Method

The fundamental principle underlying all numerical optimization methods is the decomposition of a generally complex problem into a sequence of finite subproblems, making them more manageable. In the context of low-thrust trajectory optimization for optimal control problems, the aim is to exploit numerical methods to transform the continuous problem into an approximate set of finite-dimensional subproblems. This transformation, known as transcription, aims to convert the governing set of ordinary differential equations into a problem characterized by a finite number of variables.

Numerical methods can be broadly categorized into two main types: direct and indirect methods.

Direct methods reformulate the optimal control problem as a nonlinear programming problem. The trajectory is discretized, and state and control variables are typically approximated through constant parameterization for each arc of the trajectory. Essentially, direct methods perform a parametric optimization of the time-continuous problem, converting it into an approximate finite-dimensional problem by discretizing both the state and the controls. Although direct methods can handle diverse problem formulations with minimal programming effort, achieving accurate solutions demands a particularly dense mesh for domain discretization, involving a large number of parameters, making them computationally expensive. Despite domain refinement efforts, direct methods may still suffer from accuracy issues, often necessitating solution refinement techniques. Nevertheless, with modern computers capable of handling high computational costs, one of the historical drawback of direct methods is being mitigated.

Indirect methods, on the other hand, reconfigure the optimal control problem into a Boundary Value Problem (BVP) using optimal control theory (OCT). The trajectory can be divided into arcs, which proves useful when dealing with discontinuities in the problem. The Pontryagin Maximum Principle (PMP) determines the optimal control law. The unknowns of the problem that must be found, in order to satisfy all boundary conditions and imposed constraints, are the initial variables. Indirect methods first investigate the optimality conditions of the continuous-time optimal control problem, leading to the BVP, which remains continuous through the Euler-Lagrange equations. To solve it, the BVP is discretized in time to obtain a numerical solution. Unlike direct methods, the indirect ones handle the continuous form of state and control variables. Solutions provided by indirect methods are highly accurate and generally have minimal computational cost and time compared to direct methods due to the smaller size of the problem. However, they are subject to convergence problems, mainly due to sensitivity to initial conditions and the need to account for possible discontinuities along the trajectory. It is noteworthy that solving an OCP with indirect methods requires the manual computation of problem-dependent quantities by OCT. Lawden has significantly contributed to the application of these methods in the field of space trajectory optimization; for specific details, refer to the text [35].

For a more in-depth understanding of numerical methods and their application to low-thrust trajectory optimization, please see Ref.[5] and Ref.[36], respectively.

Over the years, numerous studies at the Politecnico di Torino have established a highly efficient framework for applying optimal control theory to space trajectories. This has resulted in the development of a robust and performant code, which is also utilized in this thesis[17, 37].

3.2 Optimal Control Theory

The objective of optimal control theory is to maximize a specified quantity, the merit index \mathcal{J} , by determining an optimal control law from a set of possible ones. This law has to satisfy all constraints as the trajectory evolves from the initial state to the final state in the dynamic model. In the OCP, a set of first-order differential equations $\dot{\mathbf{x}}$ is defined to describe the variation over time of n state variables. These ODEs are functions of the state vector $\mathbf{x}(t)$ itself, the control vector $\mathbf{u}(t)$ (which contains m control variables), and the time t , the independent variable.

$$\dot{\mathbf{x}}(t) = \mathbf{f}(\mathbf{x}(t), \mathbf{u}(t), t) \quad (3.1)$$

Finding the optimal solution involves computing the optimal trajectory $\mathbf{x}^*(t)$ that, subject to the control law $\mathbf{u}^*(t)$, either maximizes or minimizes the index of merit, depending on the specific case.

3.2.1 Two-Point Boundary Value Problem

When the trajectory is determined solely by conditions at its external boundaries, namely at the initial time t_0 and final time t_f , the problem represented by the Equation (3.1) is referred to as Two-Point Boundary Value Problem. The various constraints that the trajectory must respect are grouped in the constraints vector $\boldsymbol{\chi}$

$$\boldsymbol{\chi}(\mathbf{x}_0, \mathbf{x}_f, t_0, t_f) = \mathbf{0} \quad (3.2)$$

where $\boldsymbol{\chi} : [\mathbb{R}^n, \mathbb{R}^n, \mathbb{R}, \mathbb{R}] \rightarrow \mathbb{R}^q$ contains all the q constraints. Similarly, the constraint vector \mathbf{u} could be subject to bounds, but this will be discussed later.

As mentioned earlier, the optimum in OCT is achieved by computing the maximum or minimum of the merit index, defined as follows

$$\mathcal{J} = \varphi(\mathbf{x}_0, \mathbf{x}_f, t_0, t_f) + \int_{t_0}^{t_f} [\Phi(\mathbf{x}(t), \mathbf{u}(t), t)] dt \quad (3.3)$$

Two scalar parameters are involved in the formulation of the functional \mathcal{J} : the first φ depends on the values assumed by the state variables and time at the extremal boundaries, while the integral of the function Φ depends on the values assumed by the state variables, the controls, and time itself over time. In simple terms, it quantifies how the solution evolves from the initial state to the final state. By setting each of the two scalar functions to zero individually yields two specific formulations: Lagrange's formulation results from setting φ to zero, and Mayer's

formulation results from setting Φ to zero. For the sake of simplicity, from now on, $\varphi(\mathbf{x}_0, \mathbf{x}_f, t_0, t_f)$ will simply be referred to as φ , and $\mathcal{X}(\mathbf{x}_0, \mathbf{x}_f, t_0, t_f)$ as \mathcal{X} .

At this point, the fundamental manipulation underlying indirect methods is introduced. In these methods, the optimum is determined from the augmented merit function \mathcal{J}^* , which includes a measure of how much the state variables and constraints are respected during the evolution of the solution of the ODEs in the dynamic model. Thus, the adjoint variables, gathered in the adjoint vector $\boldsymbol{\lambda}(t)$, associated with the state variables, and the Lagrange multipliers $\boldsymbol{\mu}$, linked to the boundary conditions, are introduced

$$\mathcal{J}^* = \varphi + \boldsymbol{\mu}^T \boldsymbol{\mathcal{X}} + \int_{t_0}^{t_f} [\Phi + \boldsymbol{\lambda}^T (\mathbf{f} - \dot{\mathbf{x}})] dt \quad (3.4)$$

where $\boldsymbol{\lambda} \in \mathbb{R}^n$ and $\boldsymbol{\mu} \in \mathbb{R}^m$. The Equation (3.4), as the Equation (3.3), is a function of the state variables $\mathbf{x}(t)$, and consequently of their derivatives $\dot{\mathbf{x}}(t)$, and of the control variables $\mathbf{u}(t)$. If both the equations of state and the boundary conditions are satisfied, then $\boldsymbol{\mathcal{X}} = \mathbf{0}$ and $\mathbf{f} = \dot{\mathbf{x}}$ and thus the functional \mathcal{J} is equal to the augmented functional \mathcal{J}^* . Consequently, the solution of the augmented problem in Equation (3.4) is mathematically equivalent to the solution of the problem in Equation (3.3), provided that all constraints are satisfied.

The time derivatives of the state variables $\dot{\mathbf{x}}$ that are integrated during the optimization process are potentially unknown. Therefore, it is useful to eliminate them by integrating the $-\boldsymbol{\lambda}^T \dot{\mathbf{x}}$ term by part

$$\int_{t_0}^{t_f} -(\boldsymbol{\lambda}^T \dot{\mathbf{x}}) dt = -(\boldsymbol{\lambda}_f^T \mathbf{x}_f) + (\boldsymbol{\lambda}_0^T \mathbf{x}_0) + \int_{t_0}^{t_f} (\dot{\boldsymbol{\lambda}}^T \mathbf{x}) dt \quad (3.5)$$

by substituting in the Equation (3.4), the following is obtained

$$\mathcal{J}^* = \varphi + \boldsymbol{\mu}^T \boldsymbol{\mathcal{X}} + (\boldsymbol{\lambda}_0^T \mathbf{x}_0 - \boldsymbol{\lambda}_f^T \mathbf{x}_f) + \int_{t_0}^{t_f} (\Phi + \boldsymbol{\lambda}^T \mathbf{f} - \dot{\boldsymbol{\lambda}}^T \mathbf{x}) dt \quad (3.6)$$

In Equation (3.6) now appears the system's Hamiltonian \mathcal{H}

$$\mathcal{H} = \Phi + \boldsymbol{\lambda}^T \mathbf{f} \quad (3.7)$$

Calculating the first derivative of the functional gives

$$\delta \mathcal{J}^* = \left(\frac{\partial \varphi}{\partial t_0} + \boldsymbol{\mu}^T \frac{\partial \boldsymbol{x}}{\partial t_0} - \mathcal{H}_0 \right) \delta t_0 + \quad (3.8)$$

$$+ \left(\frac{\partial \varphi}{\partial t_f} + \boldsymbol{\mu}^T \frac{\partial \boldsymbol{x}}{\partial t_f} + \mathcal{H}_f \right) \delta t_f + \quad (3.9)$$

$$+ \left(\frac{\partial \varphi}{\partial \boldsymbol{x}_0} + \boldsymbol{\mu}^T \frac{\partial \boldsymbol{x}}{\partial \boldsymbol{x}_0} + \boldsymbol{\lambda}_0^T \right) \delta \boldsymbol{x}_0 + \quad (3.10)$$

$$+ \left(\frac{\partial \varphi}{\partial \boldsymbol{x}_f} + \boldsymbol{\mu}^T \frac{\partial \boldsymbol{x}}{\partial \boldsymbol{x}_f} - \boldsymbol{\lambda}_f^T \right) \delta \boldsymbol{x}_f + \quad (3.11)$$

$$+ \int_{t_0}^{t_f} \left[\left(\frac{\partial \mathcal{H}}{\partial \boldsymbol{x}} + \dot{\boldsymbol{\lambda}}^T \right) \delta \boldsymbol{x} + \frac{\partial \mathcal{H}}{\partial \boldsymbol{u}} \delta \boldsymbol{u} \right] dt \quad j = 1, \dots, n_p \quad (3.12)$$

In order to maximize or minimize the merit index \mathcal{J}^* , it is necessary to find its stationary points; consequently, its first derivative must be zero for any choice of $\delta t_0, \delta t_f, \delta \boldsymbol{x}_0, \delta \boldsymbol{x}_f, \delta \boldsymbol{x}$ and $\delta \boldsymbol{u}$. Therefore, a meticulous selection of the added variables and Lagrange multipliers, ensuring that the respective multiplicative coefficients cancel out, is essential. From each specific term in Equation (3.8), different sets of conditions emerge. If the multiplying coefficients of the first two lines are zero, two algebraic equations are obtained at the initial and final times, known as the transversality conditions. The second two lines yield $2n$ algebraic equations, one for each state quantity at the initial and final bounds, referred to as the optimality conditions. The last two multiplication coefficients lead to two important results: n Euler-Lagrange ODEs for the adjoint variables and m algebraic equations for the control.

3.2.2 Boundary Conditions

The boundary conditions consist of the two transversality conditions and the $2n$ optimality conditions. Nullifying the respective coefficients of $\partial t_0, \partial t_f, \partial \boldsymbol{x}_0$ and $\partial \boldsymbol{x}_f$ in the set of Equations (3.8) gives

$$\frac{\partial \varphi}{\partial t_0} + \boldsymbol{\mu}^T \frac{\partial \boldsymbol{x}}{\partial t_0} - \mathcal{H}_0 = 0 \quad (3.13a)$$

$$\frac{\partial \varphi}{\partial t_f} + \boldsymbol{\mu}^T \frac{\partial \boldsymbol{x}}{\partial t_f} + \mathcal{H}_f = 0 \quad (3.13b)$$

$$\frac{\partial \varphi}{\partial \boldsymbol{x}_0} + \boldsymbol{\mu}^T \frac{\partial \boldsymbol{x}}{\partial \boldsymbol{x}_0} + \boldsymbol{\lambda}_0^T = \mathbf{0} \quad (3.13c)$$

$$\frac{\partial \varphi}{\partial \boldsymbol{x}_f} + \boldsymbol{\mu}^T \frac{\partial \boldsymbol{x}}{\partial \boldsymbol{x}_f} - \boldsymbol{\lambda}_f^T = \mathbf{0} \quad (3.13d)$$

Considering the two transversality Equations (3.13a) and (3.13b), a notable distinction emerges based on whether time is present or absent in the function φ and whether it is constrained or unconstrained. When time does not appear in φ and is unconstrained, the Hamiltonian is null at that point, both for the initial and final times. In these cases, the values of time become dependent on the optimization process. Conversely, when either one or both times are constrained, the corresponding Hamiltonian is unrestricted, and its value depends on the optimization process. For example, consider missions with an assigned duration Δt , where an initial epoch, t_0 , is assigned, leading to the subsequent assignment of the final epoch, $t_f = t_0 + \Delta t$. In this circumstance, both \mathcal{H}_0 and \mathcal{H}_f are nonzero. On the contrary, in missions where the final epoch is not constrained but subject to the optimization process, and only the initial epoch t_0 is assigned, one has $\mathcal{H}_0 \neq 0$ and $\mathcal{H}_f = 0$.

Similarly, when considering Equations (3.13c) and (3.13d), if the specific i -th state variable x_i does not appear in the φ function or in any constraint, its adjoint variable λ_{x_i} is zero at the same point. Conversely, if x_i is constrained, the corresponding adjoint variable is unconstrained. For instance, consider a simple Hohmann transfer where both the initial radius r_0 and the final radius r_f are constrained at their respective initial and final times, such that their corresponding adjoint vectors, λ_{r_0} and λ_{r_f} , are nonzero. In contrast, if the initial radius r_0 is left free, thus subject to the optimization process, the results is $\lambda_{r_0} = 0$ [17].

Equation for adjoint and control variables

Nullifying the multiplicative coefficients in the last line of Equation (3.8) produces a set of ODEs that describe how the adjoint variables and controls evolve over time. Specifically, as mentioned earlier, canceling the coefficient of $\delta \mathbf{x}$ yields the Euler-Lagrange equations for the adjoint variables

$$\dot{\boldsymbol{\lambda}} = \frac{d\boldsymbol{\lambda}}{dt} = - \left(\frac{\partial \mathcal{H}}{\partial \mathbf{x}} \right)^T \quad (3.14)$$

Instead, nullifying the coefficient of $\delta \mathbf{u}$ provides m algebraic equations for the controls

$$\left(\frac{\partial \mathcal{H}}{\partial \mathbf{u}} \right)^T = 0 \quad (3.15)$$

In general, one or more elements of the control vector \mathbf{u} can be constrained within a specific allowed interval \mathbf{u} . Since $\mathbf{u}(\mathbf{x}(t), t)$, the specific controls can depend on either the state variables or time itself. In this work only explicit and constant constraints are considered. For example, considering the thrust of the thruster,

it cannot take negative values, consequently its minimum allowable value, \mathcal{U}_{min} , must be 0, while the maximum value T_{max} , although dependent on the thruster type, certainly cannot be infinite, consequently the maximum allowable value is $\mathcal{U}_{max} = T_{max}$. It is concluded that the thrust level is in the range $0 \leq T \leq T_{max}$, namely within the allowable range $\mathcal{U}_{min} \leq u \leq \mathcal{U}_{max}$.

In the presence of explicit constraints, the optimal control value for each point of the trajectory is determined by the Pontryagin Maximum Principle (PMP), or analogously in the case of a minimization problem, the Pontryagin minimum Principle (PmP), by identifying the value that extremizes the Hamiltonian of Equation (3.7) at each specific point. Two possibilities can occur:

- if the control obtained from Equation (3.15) is within the allowable range, it represents the optimal control;
- if the control obtained from Equation (3.15) is outside the allowable range, the optimal control is at the limit of the allowable range, meaning it takes on its maximum or minimum value

Further consideration is necessary in the particular case where the Hamiltonian is linear concerning one of the constrained control variables, as the control does not explicitly appear in Equation (3.15). Two additional possibilities arise in this scenario:

- if the coefficient of the control in Equation (3.15) is nonzero, \mathcal{H} is maximized by imposing that the control takes the maximum admissible value, $u_i = \mathcal{U}_{i,max}$, if the coefficient is positive, or the minimum allowed value, $u_i = \mathcal{U}_{i,min}$, the coefficient is negative. This condition is known as *bang-bang* control, precisely what occurs in the implemented OCP, where the Hamiltonian is linear concerning the selected control variable, namely thrust T ;
- If the coefficient of the control in Equation (3.15) is zero for a finite time interval, a singular arc occurs, and it is necessary to set all successive time derivatives of the coefficient equal to zero until the control specifically appears in one of them, the optimal control is then determined by setting this time derivative equal to zero.

In summary, since a Two-Point Boundary Value Problem is formulated, with the m imposed boundary conditions $\mathbf{x} = \mathbf{0}$, one encounters $2 + 2n + m$ equations derived from the transversality, optimality, and control equations, respectively. These equations implicitly determine two times (t_0 and t_f), the initial state values of the $2n$ state ODEs (for \mathbf{x} and $\boldsymbol{\lambda}$) and the m adjoint constants ($\boldsymbol{\mu}$).

3.2.3 Multi-Point Optimal Control Problem

The trajectory can be partitioned into n_p subintervals, known as phases or arcs, to improve robustness and convergence of the code. It is precisely in this scenario, where constraints are also imposed at internal points of the trajectory, that the Multi-Point Boundary Value Problem (MPBVP) originates. The variables are continuous within each arc, while they may present discontinuities at the interface points between two adjacent arcs. As illustrated in Figure 3.1, the j -th arc begins at point $(j-1)_+$ and ends at point j_- . Additionally, each j -th arc spans a generic duration Δt_j , typically unknown and thus subject to the optimization process, and, in the most general case, varies from arc to arc.

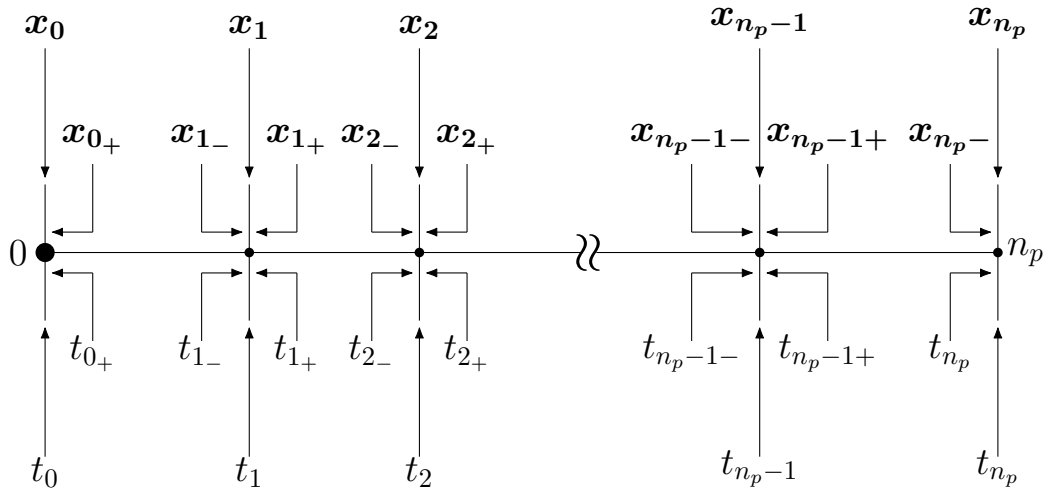


Figure 3.1: Simplified representation of an MPBVP trajectory composed of n_p arcs

In this context, boundary conditions can be imposed on both internal and external boundaries. Furthermore, they can be functions of both the state variable and the independent time variable, taking the following form

$$\mathbf{x}(\mathbf{x}_{(j-1)_+}, \mathbf{x}_{j_-}, t_{(j-1)_+}, t_{j_-}) = \mathbf{0} \quad j = 1, \dots, n_p \quad (3.16)$$

The functional \mathcal{J} becomes

$$\mathcal{J} = \varphi(\mathbf{x}_{(j-1)_+}, \mathbf{x}_{j_-}, t_{(j-1)_+}, t_{j_-}) + \sum_{j=1}^{n_p} \int_{t_{(j-1)_+}}^{t_{j_-}} \Phi(\mathbf{x}(t), \mathbf{u}(t), t) dt \quad (3.17)$$

Here, the function φ depends on the values of variables and times at each boundary, namely, both for the extremal boundary of the entire trajectory and for

each arc. Instead, the sum of all integrals of the function Φ always depends on the evolution of the state variables, the controls, and time itself, with the additional consideration of how the solution evolves from arc to arc. The augmented functional results

$$\mathcal{J}^* = \varphi + \boldsymbol{\mu}^T \boldsymbol{x} + \sum_{j=1}^{n_p} \int_{t_{(j-1)+}}^{t_{j-}} \left[\Phi + \boldsymbol{\lambda}^T (\boldsymbol{f} - \dot{\boldsymbol{x}}) \right] dt \quad (3.18)$$

and, after integrating by part

$$\mathcal{J}^* = \varphi + \boldsymbol{\mu}^T \boldsymbol{x} + \sum_{j=1}^{n_p} \left(\boldsymbol{\lambda}_{(j-1)+}^T \boldsymbol{x}_{(j-1)+} - \boldsymbol{\lambda}_{j-}^T \boldsymbol{x}_{j-} \right) + \sum_{j=1}^{n_p} \int_{t_{(j-1)+}}^{t_{j-}} \left(\Phi + \boldsymbol{\lambda}^T \boldsymbol{f} - \dot{\boldsymbol{\lambda}}^T \boldsymbol{x} \right) dt \quad (3.19)$$

The first-order derivative $\delta \mathcal{J}^*$, expressed for each arc, is given by

$$\delta \mathcal{J}^* = \left(\frac{\partial \varphi}{\partial t_{(j-1)+}} + \boldsymbol{\mu}^T \frac{\partial \boldsymbol{x}}{\partial t_{(j-1)+}} + \mathcal{H}_{(j-1)+} \right) \delta t_{(j-1)+} + \quad (3.20a)$$

$$+ \left(\frac{\partial \varphi}{\partial t_{j-}} + \boldsymbol{\mu}^T \frac{\partial \boldsymbol{x}}{\partial t_{j-}} + \mathcal{H}_{j-} \right) \delta t_{j-} + \quad (3.20b)$$

$$+ \left(\frac{\partial \varphi}{\partial \boldsymbol{x}_{(j-1)+}} + \boldsymbol{\mu}^T \frac{\partial \boldsymbol{x}}{\partial \boldsymbol{x}_{(j-1)+}} + \boldsymbol{\lambda}_{(j-1)+}^T \right) \delta \boldsymbol{x}_{(j-1)+} + \quad (3.20c)$$

$$+ \left(\frac{\partial \varphi}{\partial \boldsymbol{x}_{j-}} + \boldsymbol{\mu}^T \frac{\partial \boldsymbol{x}}{\partial \boldsymbol{x}_{j-}} - \boldsymbol{\lambda}_{j-}^T \right) \delta \boldsymbol{x}_{j-} + \quad (3.20d)$$

$$+ \sum_{j=1}^{n_p} \int_{t_{(j-1)+}}^{t_{j-}} \left[\left(\frac{\partial \mathcal{H}}{\partial \boldsymbol{x}} + \dot{\boldsymbol{\lambda}}^T \right) \delta \boldsymbol{x} + \frac{\partial \mathcal{H}}{\partial \boldsymbol{u}} \delta \boldsymbol{u} \right] dt \quad j = 1, \dots, n_p \quad (3.20e)$$

The optimality and transversality conditions are more conveniently expressed in the MPBVP by considering the j -th extreme as the upper extremal of the $(j-1)$ -th interval or the lower extremal of the j -th interval, thus

$$\frac{\partial \varphi}{\partial t_{j+}} + \boldsymbol{\mu}^T \frac{\partial \boldsymbol{x}}{\partial t_{j+}} - \mathcal{H}_{j+} = 0 \quad j = 0, \dots, n_p - 1 \quad (3.21a)$$

$$\frac{\partial \varphi}{\partial t_{j-}} + \boldsymbol{\mu}^T \frac{\partial \boldsymbol{x}}{\partial t_{j-}} + \mathcal{H}_{j-} = 0 \quad j = 1, \dots, n_p \quad (3.21b)$$

$$\frac{\partial \varphi}{\partial \boldsymbol{x}_{j+}} + \boldsymbol{\mu}^T \frac{\partial \boldsymbol{x}}{\partial \boldsymbol{x}_{j+}} + \boldsymbol{\lambda}_{j+}^T = \mathbf{0} \quad j = 0, \dots, n_p - 1 \quad (3.21c)$$

$$\frac{\partial \varphi}{\partial \boldsymbol{x}_{j-}} + \boldsymbol{\mu}^T \frac{\partial \boldsymbol{x}}{\partial \boldsymbol{x}_{j-}} - \boldsymbol{\lambda}_{j-}^T = \mathbf{0} \quad j = 1, \dots, n_p \quad (3.21d)$$

Regarding the Euler-Lagrange equations, the considerations in Section 3.2.2 remain applicable in the context of the MPBVP.

3.3 Boundary Value Problem

As described in the previous section, the OCT transforms the original BVP into an augmented one, where some initial values may be unknown. The solution to this augmented problem is determined by finding the optimal initial state $\mathbf{y}_0^* = \{(\mathbf{x}^{*T}) (\boldsymbol{\lambda}^{*T})\}^T$ that enables reaching the desired final state \mathbf{y}_f^* while satisfying all constraints. The use of indirect methods requires particular attention to the robustness of the code and its high sensitivity to initial conditions. In this study, the objective is to optimize the low-thrust trajectory of a spacecraft in the high-fidelity dynamical model of the 4BP. Analyzing this scenario requires special care, given the strong nonlinearity of the 4BP, which may lead to several numerical problems hindering convergence. Considering these highlighted issues, it becomes evident that significant improvements can be achieved by dividing the trajectory into arcs with an associated control law, as detailed in Section 3.2.3. The chosen method for computing the solution is single-shooting, selected for its simplicity of implementation, computational efficiency, and speed.

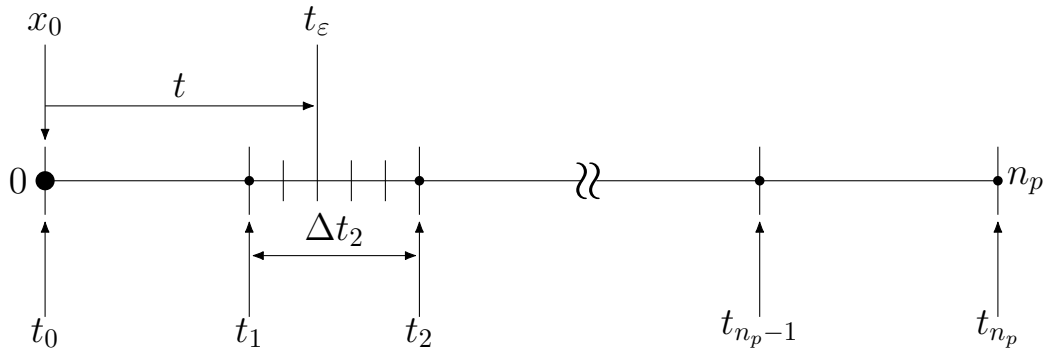


Figure 3.2: Simplified representation of nondimensional time t_ε in the j -th arc

The generic arc is divided into n_E equidistant sub-elements, as shown in Figure 3.2. One of the primary challenges with indirect methods is the unknown duration of each arc, potentially resulting in a highly ill-conditioned problem. Consequently, to avoid these problems, for the purpose of integration the independent time variable t is replaced by a new nondimensional time variable defined as follows

$$t_\varepsilon = j - 1 + \frac{t - t_{j-1}}{t_j - t_{j-1}} = j - 1 + \frac{t - t_{j-1}}{\Delta t_j} \quad (3.22)$$

with

$$\Delta t_j = t_j - t_{j-1} \quad j = 1, \dots, n_p \quad (3.23)$$

In this way, the integration extremes of the subintervals are fixed and correspond to the consecutive integer values of the new variable at the boundaries.

The general form of the complete ODE set for the indirect method is

$$\dot{\mathbf{y}} = \mathbf{f}(\mathbf{y}(t), t) \quad (3.24)$$

while in nondimensional form

$$\dot{\check{\mathbf{y}}} = \mathbf{f}(\check{\mathbf{y}}(t_\varepsilon), t_\varepsilon) \quad (3.25)$$

where $\check{\mathbf{y}}$ includes state and adjoint variables. The problem may also involve constant variables; hence, a new vector, \mathbf{z} , is introduced to account for the constants vector \mathbf{c}

$$\mathbf{z} = \{\mathbf{y}^T \mathbf{c}^T\}^T \quad (3.26)$$

Introducing the nondimensional variable t_ε in place of t , a new set of ODEs emerges

$$\dot{\check{\mathbf{z}}} = \frac{d\check{\mathbf{z}}}{dt_\varepsilon} = \mathbf{f}(\check{\mathbf{z}}(t_\varepsilon), t_\varepsilon) \quad (3.27)$$

where

$$\dot{\check{\mathbf{y}}} = \frac{d\check{\mathbf{y}}}{dt_\varepsilon} = \Delta t_j \frac{d\mathbf{y}(t)}{dt} \quad (3.28a)$$

$$\dot{\check{\mathbf{c}}} = \frac{d\check{\mathbf{c}}}{dt_\varepsilon} = \mathbf{0} \quad (3.28b)$$

The boundary conditions are now expressed as

$$\mathbf{x}(\check{\mathbf{s}}) = \mathbf{0} \quad (3.29)$$

where $\check{\mathbf{s}}$ is the vector containing the values that the variables take at both internal and external boundaries, namely

$$\check{\mathbf{s}} = \{\check{\mathbf{y}}_0^T \quad \check{\mathbf{y}}_1^T \quad \dots \quad \check{\mathbf{y}}_{n_p-1}^T \quad \check{\mathbf{y}}_{n_p}^T \quad \check{\mathbf{c}}^T\}^T \quad (3.30)$$

As previously mentioned, solving the MPBVP means finding the optimal initial values that lead to desired final states while satisfying all constraints through a numerical iteration method. Subsequently, the single-shooting method is employed

to determine the optimal initial state $\check{\mathbf{q}}_0^*$ that satisfies the boundary conditions $\mathbf{x}(\check{\mathbf{q}}_0^*) = \mathbf{0}$. The iteration process begins with the definition of a guess initial vector for the unknown variables $\check{\mathbf{q}}_r = \check{\mathbf{z}}_0$. Although, in reality, only some initial values of the variables are unknown, here is considered the more general formulation where all initial values are unknown. In each r -th iteration, the error on the boundary conditions is computed as $\check{\mathbf{x}}(\check{\mathbf{q}}_r)$. In the subsequent $(r + 1)$ -th iteration, the BCs become a function of the values assumed by the boundary conditions and the state vector at the previous r -th iteration, namely with a first-order Taylor's expansion

$$\mathbf{x}(\check{\mathbf{q}}_{r+1}) = \mathbf{x}(\check{\mathbf{q}}_r) + \frac{\partial \mathbf{x}(\check{\mathbf{q}}_r)}{\partial \check{\mathbf{q}}_{r+1}} (\check{\mathbf{q}}_{r+1} - \check{\mathbf{q}}_r) \quad (3.31)$$

the partial derivatives of the constraint vector with respect to the forward-in-time free-variable vector quantities compose the Jacobian matrix $\check{\mathbf{J}}$.

Henceforth, the notation is simplified as follows

$$\check{\mathbf{x}}_r = \mathbf{x}(\check{\mathbf{q}}_r) \quad (3.32a)$$

$$\check{\mathbf{J}}(\check{\mathbf{x}}_r) = \check{\mathbf{J}}(\check{\mathbf{x}}(\check{\mathbf{q}}_r), \check{\mathbf{q}}_{r+1}) \quad (3.32b)$$

If a solution exists, then $\check{\mathbf{x}}_{r+1} = \mathbf{0}$, and hence, the iterative solution has the following form

$$\check{\mathbf{x}}_r + [\check{\mathbf{J}}(\check{\mathbf{x}}_r)] (\check{\mathbf{q}}_{r+1} - \check{\mathbf{q}}_r) = \mathbf{0} \quad (3.33)$$

Consequently, at each iteration, the state of the vector $\check{\mathbf{q}}_r$ and the updated value of the constraint vector $\check{\mathbf{x}}_r$ can be calculated

$$\check{\mathbf{q}}_{r+1} = \check{\mathbf{q}}_r - [\check{\mathbf{J}}(\check{\mathbf{x}}_r)]^{-1} \check{\mathbf{x}}_r \quad (3.34)$$

The Jacobian matrix is calculated as a product between two matrix

$$\check{\mathbf{J}}(\check{\mathbf{x}}_r) = \frac{\partial \check{\mathbf{x}}_r}{\partial \check{\mathbf{q}}_{r+1}} = \frac{\partial \check{\mathbf{x}}_r}{\partial \check{\mathbf{s}}_r} \frac{\partial \check{\mathbf{s}}_r}{\partial \check{\mathbf{q}}_{r+1}} \quad (3.35)$$

This condition can be described by a State Transition Matrix (STM) that linearly maps the successive states at $(r + 1)$ -th step relative to those of the previous r -th step. By considering t_{ε_0} as the initial nondimensional time and $t_\varepsilon > t_{\varepsilon_0}$ as a generic forward value in nondimensional time, the STM can be written as

$$\frac{\partial \check{\mathbf{z}}_r}{\partial \check{\mathbf{q}}_{r+1}} = \check{\Phi}(t_\varepsilon, t_{\varepsilon_0}) \quad (3.36)$$

The ODEs describing the evolution of STM take the following form

$$\dot{\check{\Phi}}(t_\varepsilon, t_{\varepsilon_0}) = \frac{d}{dt_\varepsilon} \check{\Phi}(t_\varepsilon, t_{\varepsilon_0}) \quad (3.37)$$

$$= \frac{d}{dt_\varepsilon} \left(\frac{\partial \check{\mathbf{z}}}{\partial \check{\mathbf{z}}_0} \right) \quad (3.38)$$

$$= \frac{\partial}{\partial \check{\mathbf{z}}_0} \left(\frac{d\check{\mathbf{z}}}{dt_\varepsilon} \right) \quad (3.39)$$

$$= \frac{\partial \dot{\check{\mathbf{z}}}}{\partial \check{\mathbf{z}}} \frac{\partial \check{\mathbf{z}}}{\partial \check{\mathbf{z}}_0} \quad (3.40)$$

$$\dot{\check{\Phi}}(t_\varepsilon, t_{\varepsilon_0}) = \check{\mathbf{A}}(t_\varepsilon) \check{\Phi}(t_\varepsilon, t_{\varepsilon_0}) \quad (3.41)$$

the initial STM is the identity matrix, namely $\check{\Phi}(t_{\varepsilon_0}, t_{\varepsilon_0}) = \mathbf{I}$. The Jacobian matrix $\check{\mathbf{A}}$ is a block matrix composed as follows

$$\check{\mathbf{A}}(t_\varepsilon) \left[\begin{array}{c|c} \frac{\partial \dot{\check{\mathbf{x}}}}{\partial \check{\mathbf{x}}} & \frac{\partial \dot{\check{\mathbf{x}}}}{\partial \check{\boldsymbol{\lambda}}} \\ \hline \frac{\partial \dot{\check{\boldsymbol{\lambda}}}}{\partial \check{\mathbf{x}}} & \frac{\partial \dot{\check{\boldsymbol{\lambda}}}}{\partial \check{\boldsymbol{\lambda}}} \end{array} \right] \quad (3.42)$$

The method presented also allows to take into account the discontinuities of the variables at the boundaries; in fact, a generic discontinuity located at the j -th boundary can be included both in the vector of variables $\check{\mathbf{z}}$ and in the STM $\check{\Phi}$ through a vector relation $\check{\mathbf{h}}$ that links the values of the variables before and after the discontinuity

$$\check{\mathbf{z}}_{j+} = \check{\mathbf{h}} \cdot \check{\mathbf{z}}_{j-} \quad (3.43a)$$

$$\check{\Phi}(t_{\varepsilon_+}, t_{\varepsilon_0}) = \frac{\partial \check{\mathbf{h}}}{\partial \check{\mathbf{z}}_j} \check{\Phi}(t_{\varepsilon_-}, t_{\varepsilon_0}) \quad (3.43b)$$

In conclusion, the optimal initial state $\check{\mathbf{z}}_0^*$ that allows the trajectory to evolve to the desired final state $\check{\mathbf{z}}_f^*(\check{\mathbf{z}}_0^*, t_\varepsilon)$ while respecting imposed constraints $\check{\mathbf{X}}$ is determined by simultaneously integrating the principal set of ordinary differential equations and state transition matrices

$$\dot{\check{\mathbf{z}}} = \mathbf{f}(\check{\mathbf{z}}(t_\varepsilon), t_\varepsilon) \quad (3.44a)$$

$$\dot{\check{\Phi}}(t_\varepsilon, t_{\varepsilon_0}) = \check{\mathbf{A}}(t_\varepsilon) \check{\Phi}(t_\varepsilon, t_{\varepsilon_0}) \quad (3.44b)$$

The required precision E_{max} in the code is

$$E_{max} = \max(x_i) \quad (3.45)$$

The linear mapping procedure employed in STMs introduces errors that may affect convergence during the iterative process, potentially leading to an increase in error rather than its reduction at the boundary conditions. In order to increase robustness and improve convergence, two important features are implemented

- The correction applied at each iteration is only a fraction of the determined one

$$\check{z}_{r+1} = \check{z}_r - \kappa_1 \cdot [\check{J}(\check{x}_r)]^{-1} \check{x}_r \quad (3.46)$$

where κ_1 is the relaxation parameter. Values between 0.1 and 1 are usually appropriate to ensure convergence in most cases. Lower values can be used during the first rough assumptions for unknown values, while higher values can be chosen when the initial solution is already reasonably close to the optimal solution;

- At the end of each iteration, the current error is compared with the errors in the boundary conditions from the previous iteration

$$E_{max,r+1} < \kappa_2 E_{max,r} \quad (3.47)$$

here $\kappa_2 = 2 \div 3$ is usually suitable to help the first step of the iterative process in converging, even though the first two steps increase the maximum error by establishing the correct direction of optimality in the search space. If the error in the new iteration is significantly larger than in the previous one, the bisection method is applied to the correction, up to a maximum of five times. After the fifth application, the process is automatically stopped since it is unable to converge from the selected trial solution.

3.4 Application of OCT in the Case Study

The dynamic system subject to optimization is obtained by neglecting the terms related to aerodynamic forces in the ODEs given in Equation 2.9

$$\frac{d\mathbf{r}}{dt} = \mathbf{V} \quad (3.48a)$$

$$\frac{d\mathbf{V}}{dt} = \mathbf{g} + \frac{\mathbf{T}}{m} + \mathbf{a}_P \quad (3.48b)$$

$$\frac{dm}{dt} = -\frac{T}{c} \quad (3.48c)$$

The objective of the optimization is to maximize the final mass of the spacecraft at the end of the trajectory, thereby minimizing the mass of propellant used. The Mayer formulation is chosen, namely $\varphi = 0$. The state vector $\mathbf{x}(t)$ is

$$\mathbf{x} = \{r \quad \theta \quad \varphi \quad u \quad v \quad w \quad m\}^T \quad (3.49)$$

The augmented state vector $\mathbf{y}(t)$ is obtained by adding, for each variable, its respective adjoint variable

$$\mathbf{y} = \{r \quad \theta \quad \varphi \quad u \quad v \quad w \quad \lambda_r \quad \lambda_\theta \quad \lambda_\varphi \quad \lambda_u \quad \lambda_v \quad \lambda_w \quad m \quad \lambda_m\}^T \quad (3.50)$$

Since the optimization targets the final mass of the spacecraft at the end of the trajectory, the merit index is the value as of the mass at the last arc, where $j = n_p$

$$\mathcal{J} = \varphi = m_f = m_{n_p} \quad (3.51)$$

Expressing the Equations of Motion in spherical coordinates as in Equation (2.59) produces the following form of the Hamiltonian

$$\begin{aligned} \mathcal{H} = \boldsymbol{\lambda}^T \mathbf{f} &= \sum_{i=1}^{2n} \lambda_i f_i = \lambda_r u + \lambda_\theta \frac{v}{r \cos \varphi} + \lambda_\varphi \frac{w}{r} + \\ &+ \lambda_u \left[-\frac{\mu}{r^2} + \frac{v^2}{r} + \frac{w^2}{r} + \frac{T_u}{m} + (\mathbf{a}_P)_u \right] + \\ &+ \lambda_v \left[-\frac{uv}{r} + \frac{vw}{r} \tan \varphi + \frac{T_v}{m} + (\mathbf{a}_P)_v \right] + \\ &+ \lambda_w \left[-\frac{uw}{r} - \frac{v^2}{r} \tan \varphi + \frac{T_w}{m} + (\mathbf{a}_P)_w \right] + \\ &+ \lambda_m \frac{T}{c} \end{aligned} \quad (3.52)$$

written in compact form results

$$\mathcal{H} = \boldsymbol{\lambda}_r^T \mathbf{V} + \boldsymbol{\lambda}_V^T \left(\frac{\mathbf{T}}{m} - \mu \frac{\mathbf{r}}{r^3} \right) - \lambda_m \frac{T}{c} \quad (3.53)$$

Defining the *Switching Function* parameter as follows

$$\mathcal{S}_{\mathcal{F}} = \boldsymbol{\lambda}_V^T \frac{\mathbf{T}}{T} - \lambda_m \frac{m}{c} \quad (3.54)$$

and, introducing the $\mathcal{S}_{\mathcal{F}}$ parameter into Equation (3.53) yields the following form of the Hamiltonian

$$\mathcal{H} = \boldsymbol{\lambda}_r^T \mathbf{V} - \boldsymbol{\lambda}_V^T \mu \frac{\mathbf{r}}{r^3} + \frac{T}{m} \mathcal{S}_{\mathcal{F}} \quad (3.55)$$

The control vector $\mathbf{u}(t)$ corresponds to the thrust vector \mathbf{T} , encompassing both modulus and direction. As extensively discussed in the previous sections, the optimal control vector that maximizes the functional is the one that maximizes the Hamiltonian. The linearity of the \mathcal{H} with respect to the thrust T , as explained in Section 3.2.2, leads to a *bang-bang* control method. Consequently, the thrust must be set to its maximum $T = T_{max}$ when $\mathcal{S}_{\mathcal{F}} > 0$, while it must be null when $\mathcal{S}_{\mathcal{F}} < 0$. An important consideration regarding the direction of optimal thrust can be deduced from Ref.[35]: the optimal thrust direction that maximizes the switching function, and consequently the Hamiltonian, is parallel to the adjoint velocity vector $\boldsymbol{\lambda}_V$, called *primer vector*

$$\boldsymbol{\lambda}_V = \begin{pmatrix} \lambda_u \\ \lambda_v \\ \lambda_w \end{pmatrix} \quad \lambda_V = \|\boldsymbol{\lambda}_V\| \quad (3.56)$$

As seen in Section 3.2.2, in Equation (2.60), the thrust vector \mathbf{T} in the ZEN RF takes the following form

$$\mathbf{T} = \begin{pmatrix} T_u \\ T_v \\ T_w \end{pmatrix} = T \begin{pmatrix} \sin \alpha_T \\ \cos \alpha_T \cos \beta_T \\ \cos \alpha_T \sin \beta_T \end{pmatrix} \quad T = \|\mathbf{T}\| \quad (3.57)$$

where α_T is the thrust elevation angle and β_T is the heading angle, as illustrated in the Figure 3.3.

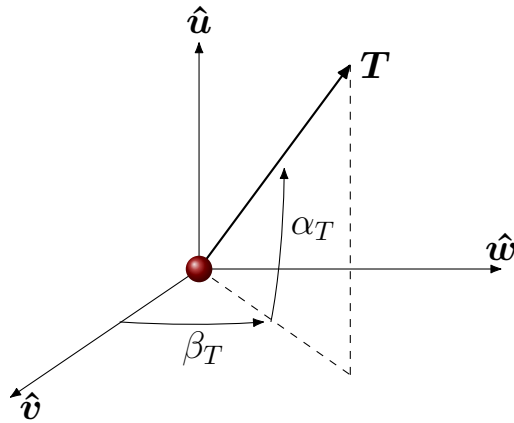


Figure 3.3: Thrust angle in the topocentric RF of the spacecraft

The optimal values of the thrust angles can be calculated by deriving the Hamiltonian in spherical coordinates in Equation (3.52) with respect to the angles themselves

$$\frac{\partial \mathcal{H}}{\partial \alpha_T} = 0 = \lambda_u \cos \alpha_T - (\lambda_v \cos \beta_T + \lambda_w \sin \beta_T) \sin \alpha_T \quad (3.58a)$$

$$\frac{\partial \mathcal{H}}{\partial \beta_T} = 0 = -\lambda_v \sin \beta_T + \lambda_w \cos \beta_T \quad (3.58b)$$

from which the following optimal directions are obtained

$$\sin \alpha_T = \frac{\lambda_u}{\lambda_V} \quad (3.59a)$$

$$\cos \alpha_T \cos \beta_T = \frac{\lambda_v}{\lambda_V} \quad (3.59b)$$

$$\cos \alpha_T \sin \beta_T = \frac{\lambda_w}{\lambda_V} \quad (3.59c)$$

The optimization process using indirect methods in highly nonlinear dynamical systems, such as the one implemented in this thesis, may give rise to numerical challenges in evaluating the error gradient, particularly concerning the handling of thrust discontinuity. Consequently, issues related to convergence may arise. In scenarios where the switching function takes on small values oscillating around zero and changes sign multiple times during the integration process, various numerical problems may occur. This could lead to the elimination of any desired thrust phase or the insertion of an undesired coasting phase. Such situations happens, for example, when a solution is on the boundary between a single-burn structure (a first thrust phase followed by a coasting phase) and a two-burn structure (thrust-coast-thrust-coast), especially if the second thrust phase has a short duration. Even if the described scenario occurs for only a few integration steps, the error gradients may be computed with low accuracy, compromising the convergence of the solution. To address this issue, this dissertation adopts a proactive approach by determining the structure of the switching function a priori. In other words, the sequence of thrust and coast phases is chosen in advance. Initially, the simplest structure, the two-arc structure, is assumed. In case the Pontryagin Maximum Principle is violated, the initially chosen structure is modified through a simple inspection of the switching function, which offers guidance on necessary adjustments to the strategy. Furthermore, an additional boundary condition is imposed requiring the switching function to be zero at the switch points where the thruster transitions from on to off or vice versa. This approach significantly enhances numerical accuracy, convergence speed, and overall robustness.

Chapter 4

Escape Trajectories from Earth-Moon L2

This chapter examines the escape trajectories from the Lagrangian Point L2 of the Earth-Moon system, computed using the n -body dynamic model described in Chapter 2. The dynamics in the vicinity of this point are highly complex. Escape trajectories are characterized by an initial phase in which the spacecraft must initiate the evasion, requiring the thrust to overcome the gravitational pull of the Moon, followed by a phase in which the gravitational pull of the Sun begins to play a key role.

The influence of the Sun on the evolution of the escape trajectory depends mainly on the relative positions of the spacecraft and the Sun itself at each moment. Recalling Equations 2.67, restated below for simplicity, it can be observed that the solar perturbation produces acceleration in the radial and tangential directions of the spacecraft

$$(\mathbf{a}_{SCs} - \mathbf{a}_{Es}) \cdot \hat{\mathbf{u}} = \frac{3}{2} \frac{\mu_s}{r_{Es}^3} \{1 + \cos [2(\theta_s - \theta)]\} \quad (4.1a)$$

$$(\mathbf{a}_{SCs} - \mathbf{a}_{Es}) \cdot \hat{\mathbf{v}} = \frac{3}{2} \frac{\mu_s}{r_{Es}^3} \sin [2(\theta_s - \theta)] \quad (4.1b)$$

Two proportional terms are defined to describe the influence of the Sun based on the angular difference between the Sun and the spacecraft $\Delta\theta = \theta_s - \theta$ [38, 39]

$$\sigma_u = 1 + \cos (2\Delta\theta) \quad (4.2a)$$

$$\sigma_v = \sin (2\Delta\theta) \quad (4.2b)$$

The trends of the two terms σ_u, σ_v and the overall term $\sigma = \sigma_u + \sigma_v$ are depicted in Figure 4.1.

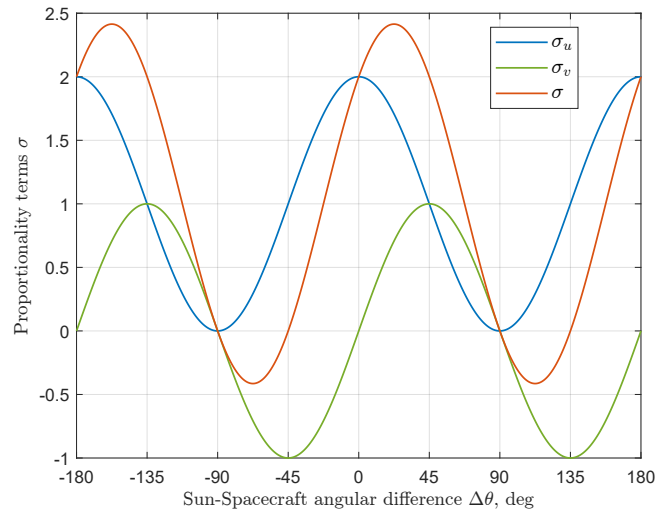


Figure 4.1: Solar gravitational perturbation proportionality terms

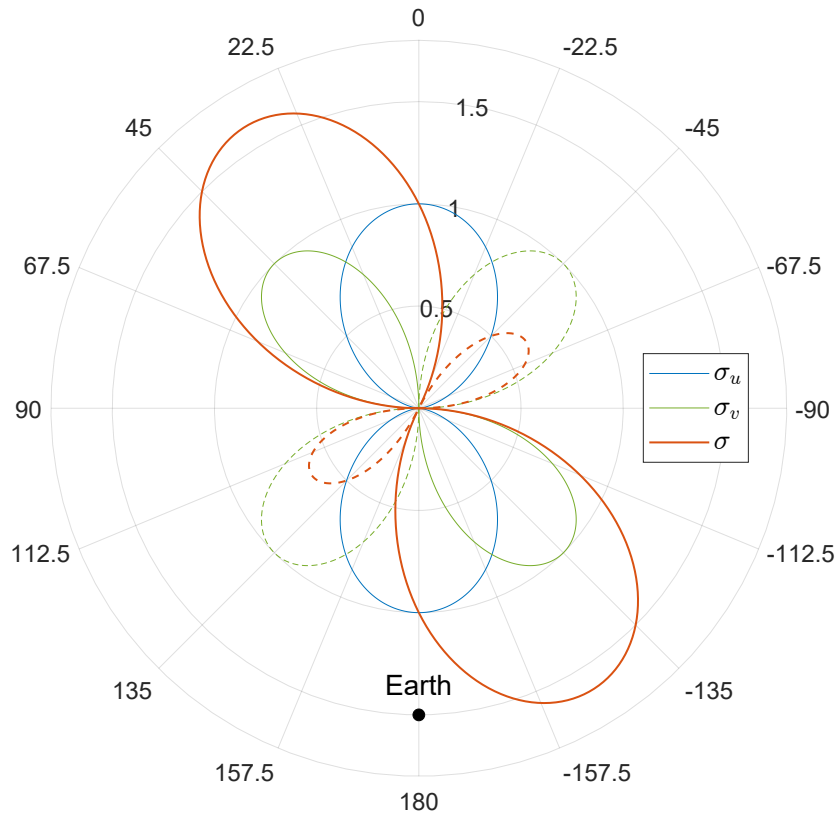


Figure 4.2: Polar plot of σ_u, σ_v and σ in function of $\Delta\theta$ in SC-Earth rotating RF

Figure 4.2 presents a polar plot of the proportionality terms, with σ_u multiplied by a coefficient of 1/2 to range from 0 to 1[17]. The values of σ represent the sum of the two contributions, where the positive values are shown as continuous lines, and the negative ones are indicated by dashed lines.

In the more general case, significant values of σ_u , indicating an increase in tangential velocity, are likely more advantageous in the initial phases. Conversely, in the later phases, when the escape is nearing completion and velocities tend to become radial, substantial values of σ_v are more beneficial. However, it is important to note that these generalizations may not always hold true, and the expected performance could vary depending on the position of the Sun relative to the starting point at the time of departure. Large positive values of σ_v , indicating a positive influence on spacecraft energy, are observed when the Sun is in the first and third quadrants of the spacecraft rotating system. In the second and fourth quadrants, the influence is either negative or null. As for σ_u , there are no values resulting in a negative influence; the maximum positive effect occurs when $-45^\circ < \Delta\theta < 45^\circ$ or $\Delta\theta > 135^\circ$ and $\Delta\theta < -135^\circ$. When considering the sum of the two contributions σ , the most favorable combination for a positive effect on spacecraft energy is when $\Delta\theta \approx 22.5^\circ$ or $\Delta\theta \approx -157.5^\circ$, while the least favorable combination occurs when $\Delta\theta \approx 112.5^\circ$ or $\Delta\theta \approx -67.5^\circ$.

In the following treatment, the analysis begins by evaluating the influence of varying the departure date throughout an entire lunar month on the performance of the escape trajectory. Subsequently, attention is directed towards analyzing the influence related to the variation of the escape duration. Finally, in a more complex analysis, the influence of the variation in the final characteristic energy is examined.

4.1 Boundary Conditions

In the context of low-thrust escape trajectories employing electric propulsion, the direction of the thrust that the spacecraft must provide plays a key role. For instance, within the framework of the two-body problem, considering a low Earth orbit, the spacecraft must consistently thrust in the direction of the tangential velocity to accumulate sufficient energy for a successful escape from Earth's gravitational pull. Depending on the orbit under consideration, the thrust may need to align parallel to the direction of velocity $\hat{\boldsymbol{v}}$ for planar orbits or adopt a specific in-plane thrust angle, namely with a specific projection in the ZEN reference system, for inclined orbits. However, the more complex the dynamical model considered, the less obvious becomes the search for the optimal direction of thrust that should be applied due to the influence of the combined gravitational attractions of other bodies, which can lead to completely unexpected solutions. In the Earth-Moon system analyzed

in this thesis, this complexity is further aggravated by the interactions of the gravitational forces of both bodies in addition to that of the Sun. In particular, this combined effect is predominant during the initial phases of the escape when the spacecraft is close to these two bodies, while as it moves away, the preponderating effect becomes the Sun's gravitational pull. Since the scenario is complex and the sensitivity of indirect methods to initial conditions is elevated, it's fundamental to judiciously choose these conditions. This section provides a presentation of the initial conditions chosen.

4.1.1 Terminal Conditions

As previously described in Section 2.2.2, the escape is assumed to be complete when the spacecraft reaches a distance from the main body equal to three times the radius of the main body's sphere of influence. Thus, in this analysis, the terminal distance r_f is set at approximately three times the radius of the Earth's sphere of influence, namely 3 million km.

Considering a circular orbit with a radius equal to the distance between the Lagrangian point and the center of the Earth as the starting point of the escape, an upper time limit for the escape can be calculated using Hohmann's formulation. In the two-body problem, the Hohmann ellipse is the transfer that requires the smallest ΔV to reach a specific final point from a specific starting point. The position of Lagrangian point L2 is computed using Hill's sphere formulation, with the assumption that the mass of the Moon is significantly smaller than that of the Earth:

$$r_{HI} = r_{El} \left(\frac{\mu_l}{3\mu_E} \right)^{1/3} = 6.1524 \cdot 10^4 \text{ km} \quad (4.3)$$

The initial position with respect to the Earth is determined as

$$r_0 = r_{El} + r_{HI} = r_{El} \left[1 + \left(\frac{\mu_l}{3\mu_E} \right)^{1/3} \right] = 4.4592 \cdot 10^5 \text{ km} \quad (4.4)$$

The Hohmann transfers semimajor axis is:

$$a_h = \frac{r_0 + r_f}{2} = 1.722960 \cdot 10^6 \text{ km} \quad (4.5)$$

consequently, the transfer duration $\mathcal{T}_h = \mathcal{T}/2$ is calculated as half the period of the Hohmann ellipse:

$$\mathcal{T}_{h,max} = \pi \sqrt{\frac{a_h^3}{\mu_E}} = 130.25 \text{ days} \quad (4.6)$$

The duration value just obtained represents the upper limit for the scenario considered. The spacecraft reaches the terminal point of the transfer with a velocity, determined as follows

$$V_f = \sqrt{2\mu_E \left(\frac{1}{r_f} - \frac{1}{2a_h} \right)} = 0.1854 \text{ km/s} \quad (4.7)$$

Since the escape is considered complete upon reaching r_f , the trajectory is an open path and consequently, the calculated velocity V_f approximates the hyperbolic excess velocity V_∞

$$V_{\infty, \min} = 0.1854 \text{ km/s} \quad (4.8a)$$

$$\mathcal{C}_{3f, \min} = 0.0344 \text{ km}^2/\text{s}^2 \quad (4.8b)$$

The latter two quantities represent the lower limit of the hyperbolic excess velocity and characteristic energy, respectively.

A reasonable choice of terminal conditions can be made by considering the upper and lower limits mentioned above. For the duration of the escapes Δt , a range of 60 to 90 days has been selected, while for the characteristic energy \mathcal{C}_{3f} , a range of values between 0.1 and 0.5 km^2/s^2 . These conditions have been applied alternatively, resulting in three different case studies:

- Fixed escape duration
- Variable escape duration
- Fixed characteristic energy

4.1.2 Initial Conditions

The starting point L2 is determined by the Hill sphere formulation in Equation (4.3), where the time-dependent distance between the two main bodies appears and is obtained from the JPL DE430 ephemerides. This is precisely why a variation in the starting date may significantly impact the performance of the escape. In fact, the variation in the states of the Moon and Sun over time influences the nature of the trajectory, meaning that even if the other initial conditions are the same, a variation in the start date will induce different behaviors and solutions. In this thesis, the analysis begins by examining escape trajectories with a duration set at 75 days and departure date that varies systematically in one-day increments over an entire lunar month. The average duration of the synodic month, which varies slightly over time, is about 29.53 days[40]. Consequently, the analyses in this phase involve starting epochs spanning from 19/10/2025 to 15/11/2025. In

this first phase, extensively discussed in the following sections, the identification of three solution families occurred, labeled with the Roman numerals I, II, and III. Additionally, the first family is further divided into three sub-families labeled with the letters A, B, and C. Consequently, five starting epochs, presented in Table 4.1, have been chosen for the subsequent analyses, facilitating a comprehensive description of each family’s behavior.

ID	Color	Epoch (UTC)	Family	Sub-Family
\mathcal{E}_1	●	2025/10/19 06:26:52.6170	I	A
\mathcal{E}_2	●	2025/10/21 06:26:31.5324	I	A
\mathcal{E}_3	●	2025/10/22 06:26:20.9901	I	B
\mathcal{E}_4	●	2025/10/29 06:25:07.1942	II	
\mathcal{E}_5	●	2025/11/03 06:24:14.4828	III	
\mathcal{E}_6	●	2025/11/11 06:22:50.1446	I	C

Table 4.1: Selected departure epochs

The initial conditions of the state variables $\mathbf{x}_0(\mathcal{E})$ are always known for each starting epoch. The position vector is determined by using the Equation (4.4) to identify the radius, coupled with JPL ephemerides to accurately position the spacecraft at the L2 point. On the other hand, the initial velocity vector is established by imposing the same angular velocity as the relative motion of the primaries.

The initial conditions that must be provided to the code for each starting epoch pertain to the adjoint variables $\boldsymbol{\lambda}_0(\mathcal{E})$ and are unknown.

$$\boldsymbol{\lambda}_0(\mathcal{E}) = \{\lambda_r \quad \lambda_\theta \quad \lambda_\varphi \quad \lambda_u \quad \lambda_v \quad \lambda_w\} \quad (4.9)$$

To induce an optimization process that converges, reasonable values for these variables must be provided. Some exhibit reasonably intuitive evolution over time, while others have less predictable behavior. The adjoint variables related to velocity play a crucial role; their magnitude indicates the relevance of thrust the direction of the specific velocity to which the adjoint variable refers at a given time; the sign indicates whether this thrust aligns (if positive) or opposes (if negative) the direction of the specific velocity. In simpler words, a higher magnitude of one adjoint variable than the others emphasizes importance in the direction of thrust along the corresponding velocity. The adjoint variable λ_r provides a measure of the significance of the change in radius over time. Therefore, at the beginning of the escape, its value is naturally positive, indicating the start of the escape. The other two adjoint variables assume a less important role.

Another crucial piece of information to determine a priori, as explained in Section 3.4, is the structure of the thrust arcs, that is, the number of phases into

which the trajectory should be divided. The structure typically involves an initial thrust arc to initiate the escape maneuver, followed by a coasting phase to reach the final destination. The structure described is the simplest one, a double arc with a single thrust phase. In cases where the PMP is violated, more complex structures can be chosen, such as a four-arc structure in which there are two thrust and two coasting phases. It's noteworthy that in scenarios where the final destination is fixed and the terminal velocity is free, the final values of the adjoint variables for the velocity components are zero, in fact, in the terminal phase of the trajectory the switching function is negative and the thruster is off.

4.1.3 Propellant Consumption

The final equation in set (2.9) describes the fuel consumption over time resulting from the applied constant thrust. This assumption is based on the constancy of available power and specific impulse at 1 AU, leading to a constant thrust. The available power, and consequently the thrust, are inversely proportional to the square of the distance from the Sun

$$T(r_{sSC}) = \frac{2\eta_T P(r_{sSC})}{c} = \frac{2\eta_T}{c} \frac{P^*}{r_{sSC}^2} = \frac{T^*}{r_{sSC}^2} \quad (4.10)$$

where the efficiency η_T is assumed constant; the effective exhaust velocity c is proportional to the specific impulse I_{sp} , since $c = I_{sp}g_0$ and thus is also constant; P^* and T^* are the values of available power and thrust at 1 AU.

The implemented electric propulsion system is a Hall-effect thruster, the main characteristics of which are shown in Table 4.2.

Quantity	Value	Dimension
P^*	4.2	kW
I_{sp}	2000	s
η_T	0.625	

Table 4.2: Implemented electric propulsion system's main characteristic

Following the calculation of the optimal trajectory, the final mass of the spacecraft is known. Consequently, by applying the Tsiolkovsky relation, seen in Equation (1.1) and provided below for clarity, the ΔV required by the mission can be calculated.

$$\Delta V = -I_{sp}g_0 \ln \left(\frac{m_f}{m_0} \right) \quad (4.11)$$

4.2 Escapes with imposed mission duration Δt

By varying the departure date over an entire lunar month, from October 19, 2025 to November 15, 2025, and fixing the evasion duration at 75 days while leaving the final energy free, an entire family of solutions emerges, as illustrated in Figure 4.3.

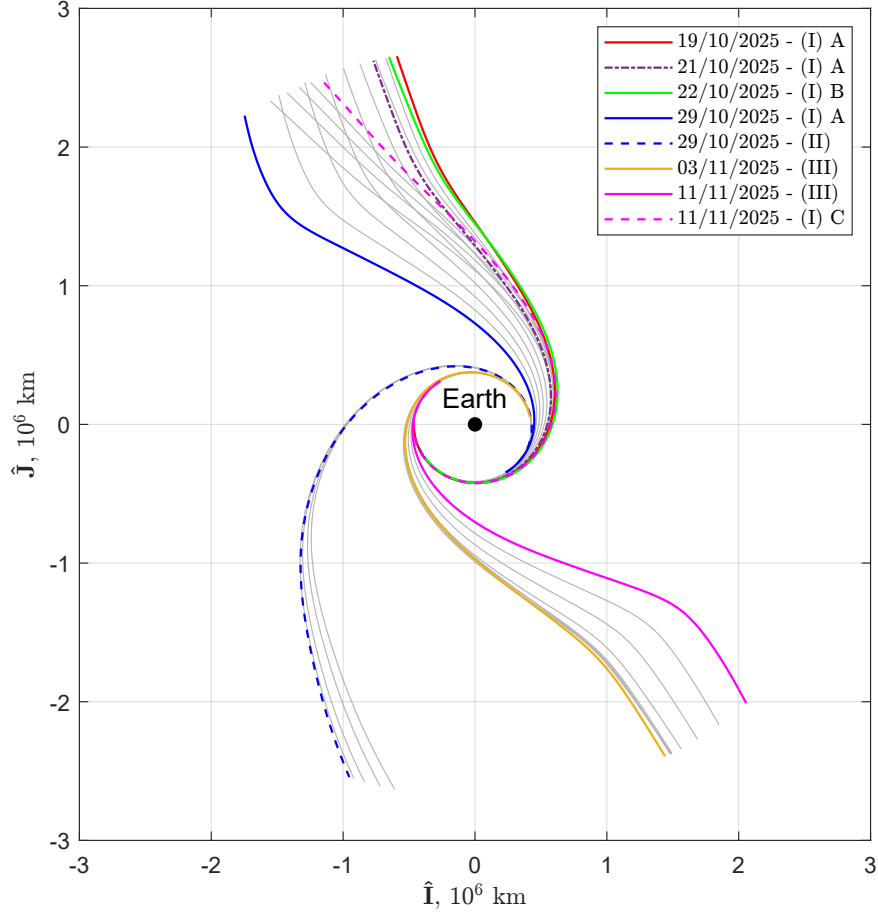


Figure 4.3: EML2 escape trajectories over a lunar month - fixed $\Delta t = 75$ days, free \mathcal{C}_{3f} , EME2000 RF

Given the intricate nature of the analyzed system, the trajectories are found to be organized into distinct families. The solutions highlighted in Figure 4.3, with their detailed performance outlined in Table 4.3, have been selected to represent each of these solution families and will be utilized as reference from now on. Additionally, a 4-arc solution is also included, which will be analyzed in detail later.

Figure 4.4a presents the trend of propellant request and final characteristic energy for all solutions along the entire lunar month. Family 1, spanning from \mathcal{E}_1 to \mathcal{E}_4 , exhibits the maximum \mathcal{C}_{3f} and minimum propellant consumption at the

ID	Line ID	Departure Date	Family	Sub Family	n_p	m_f kg	ΔV m/s	\mathcal{C}_{3f} (km/s) ²
1	●	19/10/2025	I	A	2	848.003	46.135	0.2330
2	●	21/10/2025	I	A	4	847.690	53.372	0.1823
3	●	22/10/2025	I	B	2	847.094	67.170	0.2067
4	●	29/10/2025	I	A	2	843.181	157.975	0.0072
4	●	29/10/2025	II		2	849.114	20.453	0.4796
5	●	03/11/2025	III		2	849.033	22.315	0.2042
6	●	11/11/2025	III		2	840.806	213.298	0.0549
6	●	11/11/2025	I	C	2	847.703	53.078	0.4584

Table 4.3: EML2 escape trajectories performance - fixed $\Delta t = 75$ days, free \mathcal{C}_{3f}

beginning. Moving toward \mathcal{E}_4 , the propellant request increases significantly, and \mathcal{C}_{3f} decreases to zero values, suggesting that these specific evasions are not feasible. At \mathcal{E}_2 , there is a slight local increase in \mathcal{C}_{3f} . Family 2, extending from \mathcal{E}_4 to \mathcal{E}_5 , is characterized by very high performance, which means high \mathcal{C}_{3f} and low fuel consumption. Family 3, which ranges from \mathcal{E}_5 to \mathcal{E}_6 , has a behavior similar to that of Family 1, with higher performance at the beginning, then decreasing toward \mathcal{E}_6 . Family 1, which starts at \mathcal{E}_6 , after one lunar month, tracks the performance observed at \mathcal{E}_1 . Similar conclusions can be derived from Figure 4.4b, which displays the trend of final mass and \mathcal{C}_{3f} over the entire lunar month.

Looking at Figure 4.5, which illustrates the trend of the adjoint variables $\lambda_{r,0}$, $\lambda_{u,0}$, and $\lambda_{v,0}$, it becomes evident that the worsening of escape performance occurs when the gradient of the optimal adjoints tends to reach very high or very low values. In fact, at the end of the escape trajectory these must be zero, and thus a high initial gradient implies low escape performance.

The relative position between the Sun and spacecraft significantly influences the escape performance. In cases where becomes particularly disadvantageous achieving high levels of terminal energy, even with prolonged thrust phases, it is not possible. The relative Sun-Spacecraft and Moon-Spacecraft angles are shown in Figures 4.6a and 4.6b, while the in-plane thrust angle is represented in Figure 4.6c. Additionally, Figure 4.7 presents a polar view of the Sun-Spacecraft angle evolution along the trajectory, overlaid on the representation of solar perturbation coefficients in Figure 4.2. The radial coordinate represents the Earth-Spacecraft position vector. The polar plot has been obtained through mathematical nondimensionalization; moreover, the initial coordinates of the various represented families are slightly separated for clarity.

The first selected departure date \mathcal{E}_1 is characterized by a two-arc structure, resulting in a single thrust phase, and low propellant consumption. The starting point is positioned near the maximum of overall solar perturbation σ , precisely

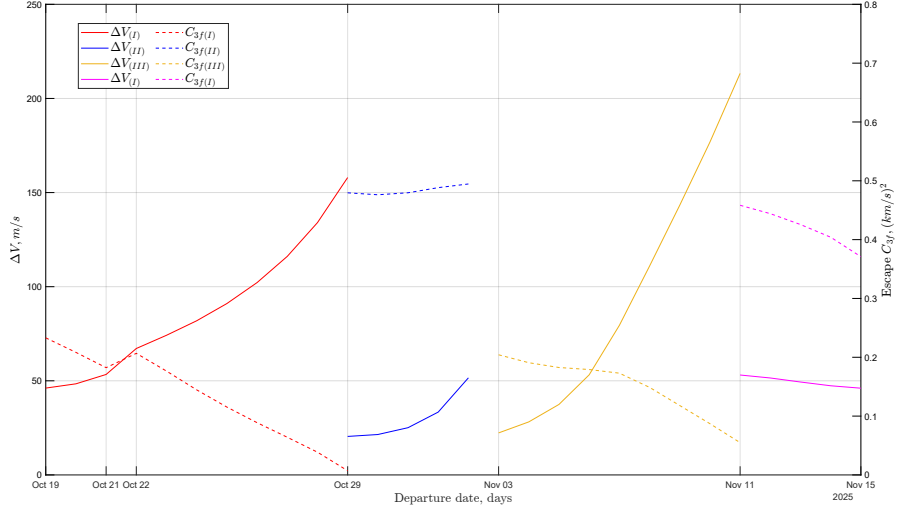
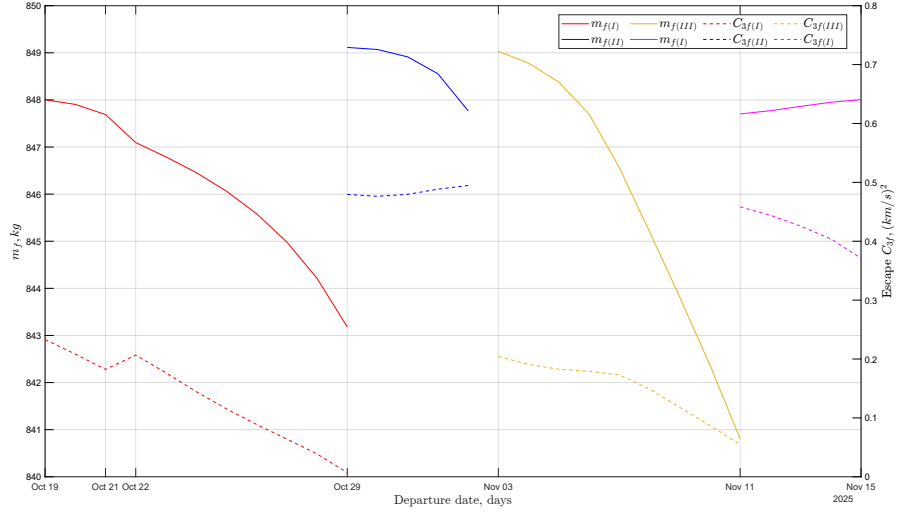

 (a) Trend over time of ΔV and \mathcal{C}_{3f}

 (b) Trend over time of m_f and \mathcal{C}_{3f}

Figure 4.4: EML2 escape trajectories over a lunar month - trend over time of cost and free final characteristic energy - fixed $\Delta t = 75$ days, free \mathcal{C}_{3f}

between the decreasing of positive tangential solar perturbation σ_v and the rising of radial solar perturbation σ_u . Thrust is applied until the radial solar perturbation also contributes significantly to the escape.

Departures at \mathcal{E}_4 , still characterized by a single-burn, diverge into two distinct families. The initial point is positioned within a region neutral to solar perturbations. The departure within the first family demonstrates significantly inferior performance compared to the second family. The first strategy aims to maximize the positive

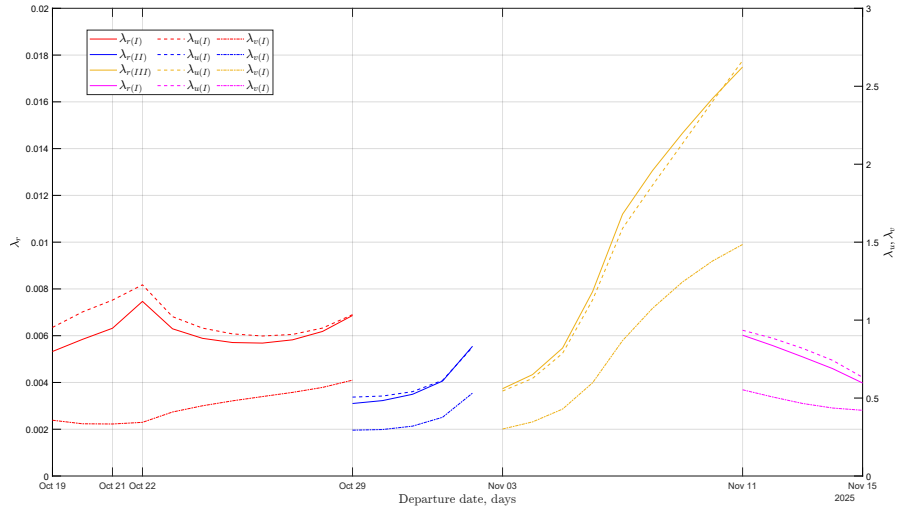
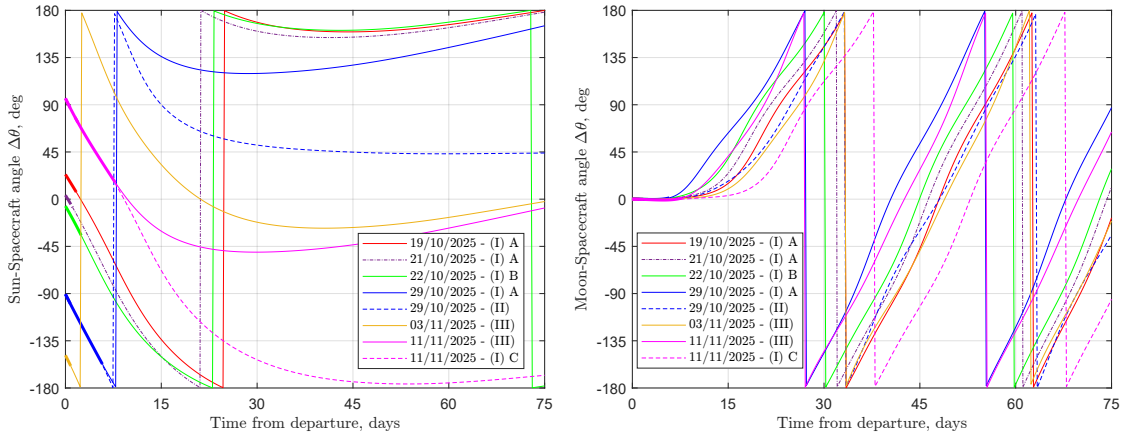


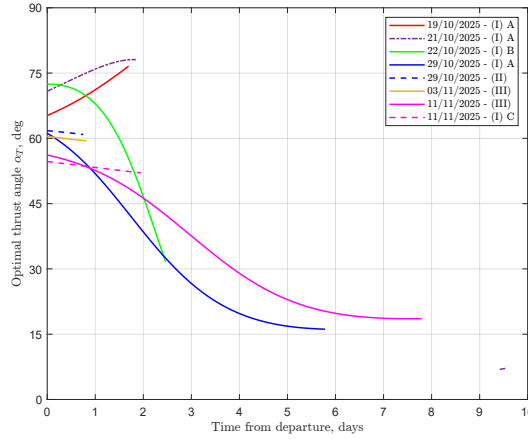
Figure 4.5: EML2 escape trajectories over a lunar month - trend over time of adjoint variables $\lambda_{r,0}$, $\lambda_{u,0}$, $\lambda_{v,0}$ - fixed $\Delta t = 75$ days, free \mathcal{C}_{3f}

tangential solar perturbation σ_v during the initial phase, in fact the angle of the optimal thrust begins rather radial and then evolves toward a more tangential direction. In this way the spacecraft is able to take advantage of the σ_v , but because it will spend a lot of time, in the later phase of the escape, in a very disadvantageous zone, namely the one with the maximum negative σ peak, it is forced to produce a very long burn. This solution represents a local optimum rather than a global one; indeed, the solution belonging to family II exhibits markedly higher performance. The latter is characterized by a strategy that accepts a shorter thrust phase applied solely at the beginning of the trajectory, precisely at the neutral point $\Delta\theta \approx 90^\circ$. This approach ensures that the radial acceleration enables the spacecraft to remain longer in the positive perturbative region, facilitating the attainment of sufficient velocity to pass swiftly the negative σ region and successfully complete the escape. In the \mathcal{E}_6 departures, starting from the diametrically opposite neutral point, the same behavior as just described for \mathcal{E}_4 departures is found. The solution exhibiting the highest performance is the one that belongs to the first family while the one with the worst performance belongs to the third. These two departures are a clear example of how exploiting positive solar perturbations leads to a better performance and a reduction of the used propellant; conversely, the greater the propulsive effort employed in unfavorable areas the greater the propellant demand and the lower the final energy achieved.

Investigating it is possible to come to the conclusion that the characteristic energy trends over time for both \mathcal{E}_4 and \mathcal{E}_6 . This aligns with the earlier discussion, as it can be observed that for the solutions involving a long initial thrust phase,



(a) Trend over time of Sun-Spacecraft relative angle $\Delta\theta$ (b) Trend over time of Moon-Spacecraft relative angle $\Delta\theta$



(c) Trend over time of optimal thrust angle α_T

Figure 4.6: EML2 selected escape trajectories over a lunar month - trend over time of Sun-SC relative angle, Moon-SC relative angle and optimal thrust angle - fixed $\Delta t = 75$ days, free \mathcal{C}_{3f}

\mathcal{C}_3 first rises vertically due to the thrust exerted, but then decreases to the point where \mathcal{C}_3 becomes lower in comparison to the strategy involving a shorter thrust arc.

Examining Figure 4.6c, it is evident that the EML2 escapes are characterized by a significant radial thrust component. This is attributed to the spacecraft's need to steadily move away from the Moon after departure to prevent being recaptured by the Moon's gravitational pull.

The departure at \mathcal{E}_5 employs an initial thrust arc to capitalize on the entire peak of the solar perturbation, leading to commendable performance with minimal

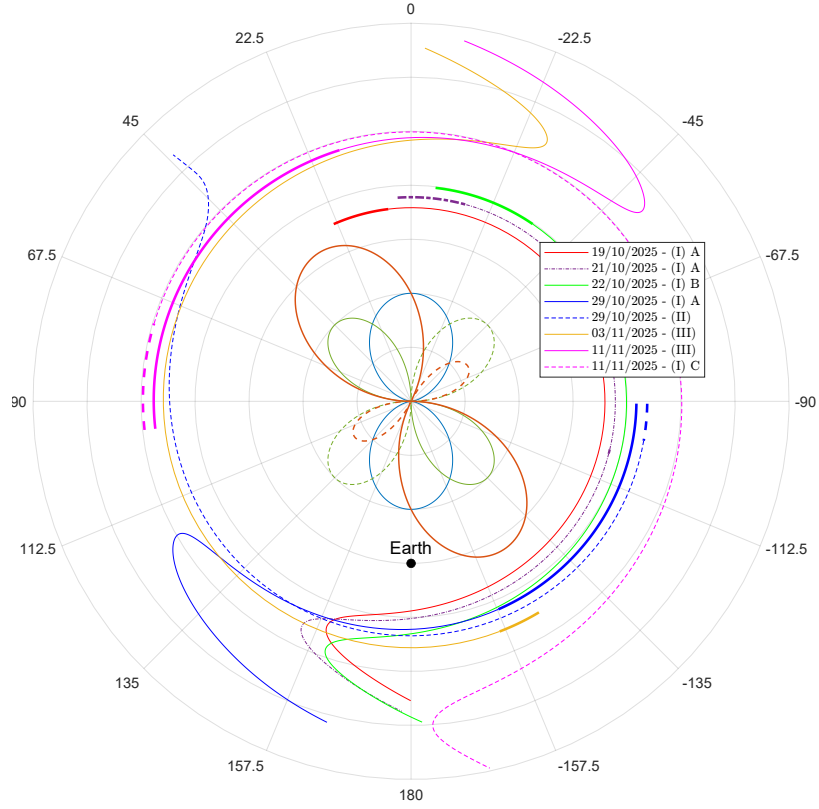


Figure 4.7: EML2 selected escape trajectories polar plot - fixed $\Delta t = 75$ days, free \mathcal{C}_{3f} , Earth-Spacecraft rotating RF

fuel consumption.

The departure at \mathcal{E}_2 , in contrast to the previously analyzed departures, features a 4-arc structure. The switching function trend for \mathcal{E}_1 , \mathcal{E}_2 , and another intermediate departure date. The first and last departures employ a two-arc strategy, while \mathcal{E}_2 utilizes the four-arc approach. Moving forward continuously from the preceding solutions to \mathcal{E}_2 reveals a non-monotonic trend in the initial phase, signifying the presence of a peak following an initial slope. When this peak is no longer situated at negative $\mathcal{S}_{\mathcal{F}}$ values, the PMP is violated and consequently the thrust structure in the violated arc must be modified. In this case, the thrust structure has been modified accordingly by inserting a second burn. Since the trend of δ_v reflects that of $\mathcal{S}_{\mathcal{F}}$, the change in initial assumptions can be clearly seen in Figure 4.5 when λ changes drastically in the family I.

Figure 4.8 shows the entire family of solutions plotted in the Sun-Earth synodic RF centered on the Earth. The solutions with departures $\mathcal{E}_1, \mathcal{E}_2, \mathcal{E}_3, \mathcal{E}_4$ of family I, and \mathcal{E}_6 of family I occupy the first and fourth quadrants, resulting in $\Delta\theta = 180^\circ$, thereby leveraging the radial component of the solar perturbation in the final

stages of the escape. Conversely, for the \mathcal{E}_5 and \mathcal{E}_6 departure dates of family III, a symmetrical scenario unfolds, culminating in the escape towards the Sun, still allowing favorable exploitation of the radial component during the concluding phase of the escape. The sole trajectory that deviates from ending at $\Delta\theta = 0^\circ$ or $\Delta\theta = 180^\circ$ is the one with departure \mathcal{E}_4 of family II, which end at $\Delta\theta = 45^\circ$. This deviation is attributed to a more intensive exploitation of the tangential component.

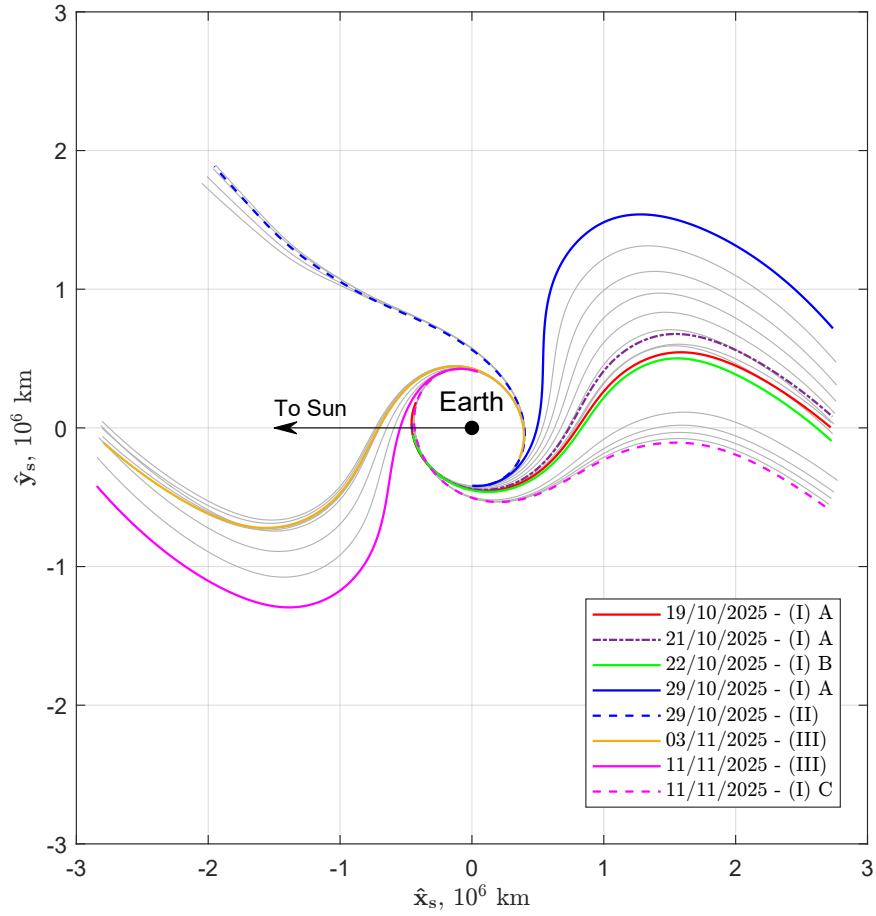


Figure 4.8: EML2 escape trajectories over a lunar month - fixed $\Delta t = 75$ days, free \mathcal{C}_{3f} , SE synodic RF

Henceforth, the departures outlined in Table 4.4 are taken as a reference for subsequent analysis.

ID	Epoch (UTC)	Family	Sub-Family
\mathcal{E}_1	2025/10/19 06:26:52.6170	I	A
\mathcal{E}_3	2025/10/22 06:26:20.9901	I	B
\mathcal{E}_4	2025/10/29 06:25:07.1942	II	
\mathcal{E}_5	2025/11/03 06:24:14.4828	III	
\mathcal{E}_6	2025/11/11 06:22:50.1446	I	C

Table 4.4: EML2 selected escape trajectories

4.3 Escapes with variable mission duration Δt

In this section, an analysis is conducted to assess how a variation in the escape duration impacts its performance. The duration is varied within the range of 60 to 90 days. Due to the Moon’s proximity to the starting point and the intricate lunisolar gravitational perturbations, the families described in the final free energy scenario become even more distinct. Figure 4.9 illustrates the manifold of solutions for each departure date under consideration, while Table 4.5 presents the performance for the selected durations in this analysis.

Figure 4.10 displays the Sun-Spacecraft angle for the selected durations for each start date, while Figure 4.11 shows the optimal thrust angle α_T .

In addition, Figure 4.12 shows the polar views of all escape trajectories as a function of Sun-Spacecraft angle $\Delta\theta$ and Figure 4.13 shows the trajectories in the Sun-Earth synodic RF, centered on Earth.

For the initial departure \mathcal{E}_1 , durations shorter than the reference, i.e., 75 days, employed in the analysis conducted in the previous section necessitate a modification in the thrust structure. Specifically, the introduction of a second thrust arc becomes essential to take advantage of the positive solar perturbations occurring in the third quadrant. The duration of this thrust phase increases as the available time for the escape decreases, aiming to better exploit the peak of the positive tangential component σ_v and accumulate sufficient energy before reaching the $\Delta = 180^\circ$ condition, where the radial component facilitates completing the escape. It is noteworthy that the direction of the initial thrust is not only strongly radial but also $\alpha_T > 90^\circ$ indicating that the spacecraft decelerates at the beginning of the trajectory, implying a passage closer to the Moon that still guarantees adequate energy for initiating the escape. The described scenario results in a higher final characteristic energy but also entails increased propellant consumption. Conversely, for durations approaching higher values, the strategy remains the same as in the free terminal energy analysis. As the duration increases, the thrust arc shortens, causing the spacecraft to spend more time in the subsequent unfavorable zone. This inevitably leads to a decrease in terminal energy but an improvement in fuel

consumption.

Departures \mathcal{E}_3 , \mathcal{E}_5 , and \mathcal{E}_6 exhibit characteristics similar to those of \mathcal{E}_1 . Specifically, for \mathcal{E}_3 and \mathcal{E}_6 , everything previously discussed remains applicable, except that in these cases, the situation involving the presence of $\alpha_T > 90^\circ$ does not occur. Conversely, \mathcal{E}_5 mirrors the behavior observed in \mathcal{E}_1 , with the introduction of the 4-arc structure occurring at 60 days in this case. Such a departure, marked by an initial position at the σ peak, enables achieving very high performance.

Finally, concerning the departure \mathcal{E}_4 with decreasing duration, the obtained solutions align with those belonging to family I, as observed in the analysis presented in Section 4.2. This strategy involves a single long thrust phase from the initial position, situated in a region neutral to solar perturbations, aiming to maximize the exploitation of the σ peak. This is also evident in the trend of the optimal thrust angle, where the initially dominant radial component gradually decreased in favor of a more tangential component. In the other case, when the duration tends to increase, the strategy resembles that of the family II solution presented in Section 4.2, in that thrust is applied in a reduced fashion and only at the beginning, when the spacecraft is in the neutral region.

Solutions with departures \mathcal{E}_1 , \mathcal{E}_3 , and \mathcal{E}_6 occupy the first and fourth quadrants, resulting in $\Delta\theta = 180^\circ$, thus exploiting the radial component of the solar perturbation in the final phases of the escape. In contrast, for the \mathcal{E}_5 departure dates, a symmetric scenario occurs, culminating in the escape toward the Sun, still allowing favorable exploitation of the radial component during the final phase of the escape. The only trajectories that deviate from ending with $\Delta\theta = 0^\circ$ or $\Delta\theta = 180^\circ$ are those with \mathcal{E}_4 departure that instead end with $\Delta\theta \approx 45^\circ$ and $\Delta\theta \approx 157.5^\circ$.

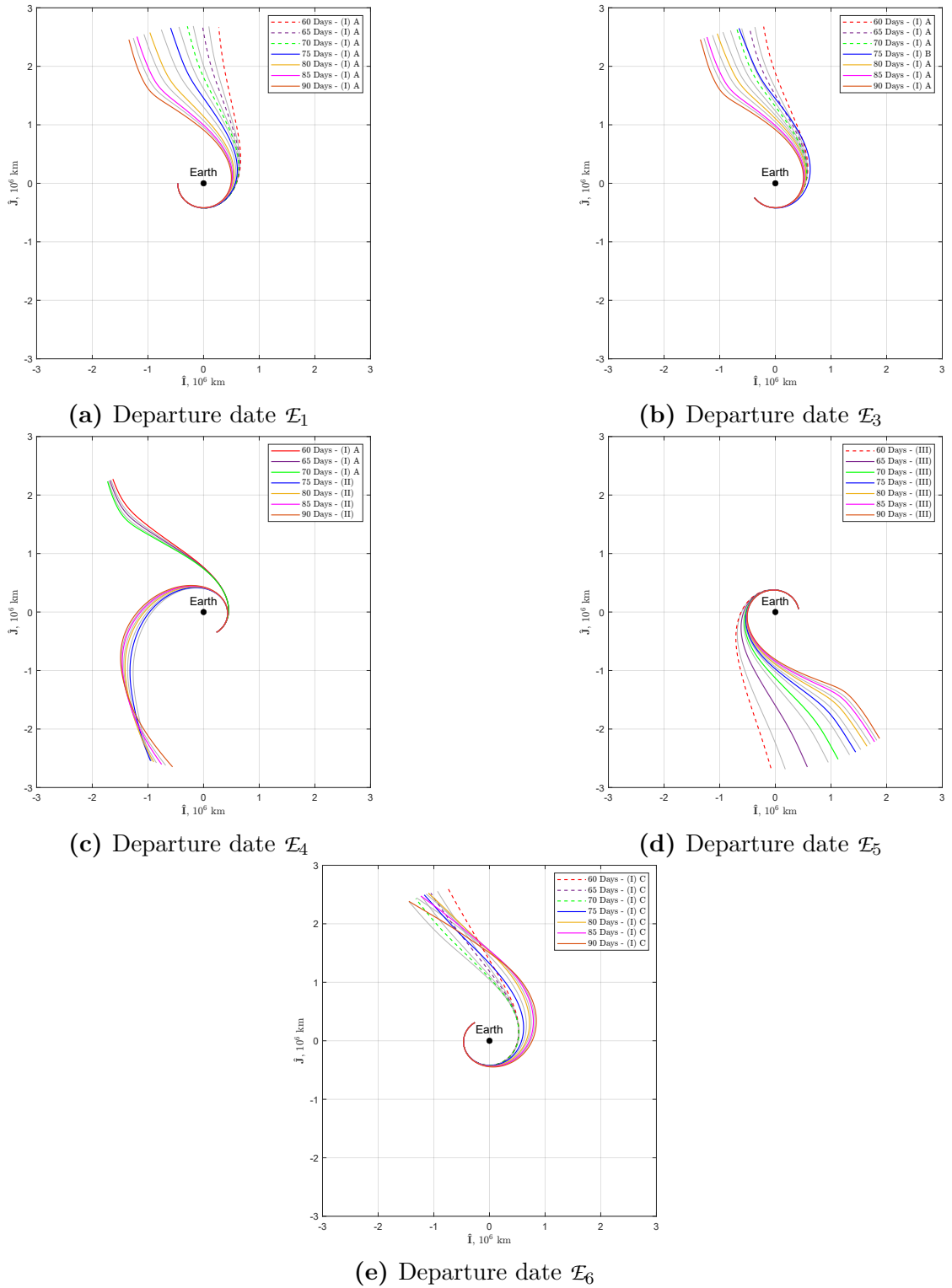


Figure 4.9: EML2 selected escape trajectories over a lunar month - variable Δt , free \mathcal{E}_{3f} , EME2000 RF

Duration <i>Days</i>	Line ID	Family	Sub Family	n_p	m_f <i>kg</i>	ΔV <i>m/s</i>	\mathcal{E}_{3f} <i>(km/s)²</i>
60	●	I	A	4	844.613	124.708	0.4832
65	●	I	A	4	846.148	89.092	0.3974
70	●	I	A	4	847.257	63.407	0.3232
75	●	I	A	2	848.003	46.135	0.2330
80	●	I	A	2	848.191	41.787	0.1282
85	●	I	A	2	848.248	40.464	0.0791
90	●	I	A	2	848.276	39.826	0.0647

 (a) Departure date \mathcal{E}_1

Duration <i>Days</i>	Line ID	Family	Sub Family	n_p	m_f <i>kg</i>	ΔV <i>m/s</i>	\mathcal{E}_{3f} <i>(km/s)²</i>
60	●	I	A	4	844.603	124.933	0.3782
65	●	I	A	4	845.841	96.213	0.2992
70	●	I	A	4	846.733	75.536	0.2246
75	●	I	B	2	847.094	67.169	0.2067
80	●	I	A	2	847.855	49.561	0.1066
85	●	I	A	2	848.087	44.196	0.0763
90	●	I	A	2	848.200	41.578	0.0683

 (b) Departure date \mathcal{E}_3

Duration <i>Days</i>	Line ID	Family	Sub Family	n_p	m_f <i>kg</i>	ΔV <i>m/s</i>	\mathcal{E}_{3f} <i>(km/s)²</i>
60	●	I	A	2	841.138	205.553	0.0745
65	●	I	A	2	842.045	184.416	0.0358
70	●	I	A	2	842.695	169.283	0.0084
75	●	II		2	849.114	20.453	0.4796
80	●	II		2	849.069	21.490	0.4411
85	●	II		2	849.029	22.415	0.4192
90	●	II		2	848.992	23.270	0.4248

 (c) Departure date \mathcal{E}_4
Table 4.5: EML2 escape trajectories performance - variable Δt , free \mathcal{E}_{3f}

Duration <i>Days</i>	Line ID	Family	Sub Family	n_p	m_f <i>kg</i>	ΔV <i>m/s</i>	\mathcal{E}_{3f} <i>(km/s)²</i>
60	●	III		4	847.780	51.283	0.5413
65	●	III		2	848.906	25.256	0.4331
70	●	III		2	849.002	23.037	0.3012
75	●	III		2	849.033	22.314	0.2042
80	●	III		2	849.049	21.955	0.1351
85	●	III		2	849.058	21.742	0.0991
90	●	III		2	849.064	21.601	0.0921

 (d) Departure date \mathcal{E}_5

Duration <i>Days</i>	Line ID	Family	Sub Family	n_p	m_f <i>kg</i>	ΔV <i>m/s</i>	\mathcal{E}_{3f} <i>(km/s)²</i>
60	●	I	C	4	842.842	165.872	0.6656
65	●	I	C	4	845.211	110.807	0.5301
70	●	I	C	4	846.887	71.955	0.4414
75	●	I	C	2	847.703	53.078	0.4584
80	●	I	C	2	847.654	54.213	0.4758
85	●	I	C	2	847.605	55.340	0.4662
90	●	I	C	2	847.553	56.540	0.4688

 (e) Departure date \mathcal{E}_6
Table 4.5: EML2 escape trajectories performance - variable Δt , free \mathcal{E}_{3f}

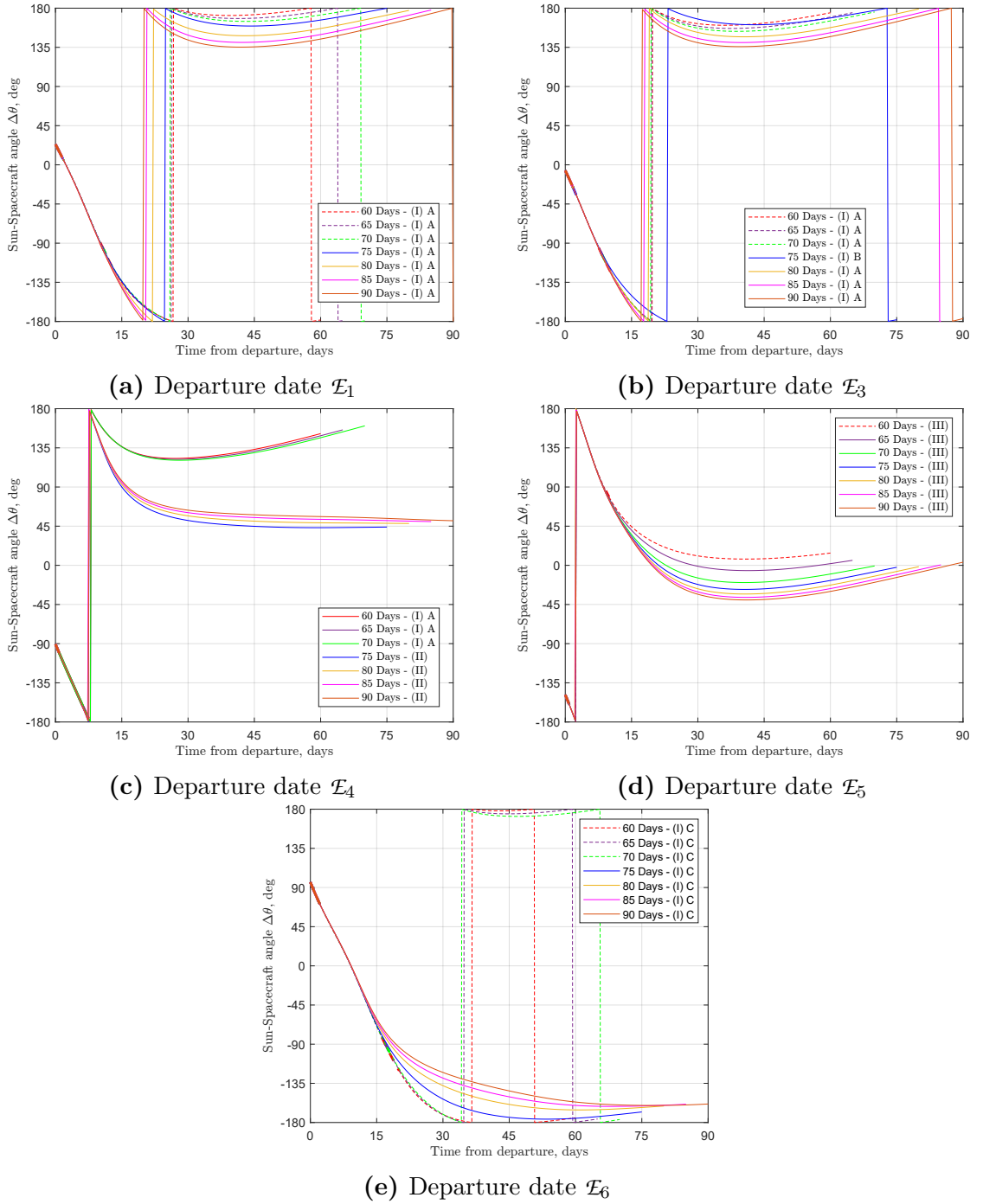


Figure 4.10: EML2 selected escape trajectories - trend over time of Sun-SC relative angle - variable Δt , free \mathcal{C}_{3f}

Escape Trajectories from Earth-Moon L2

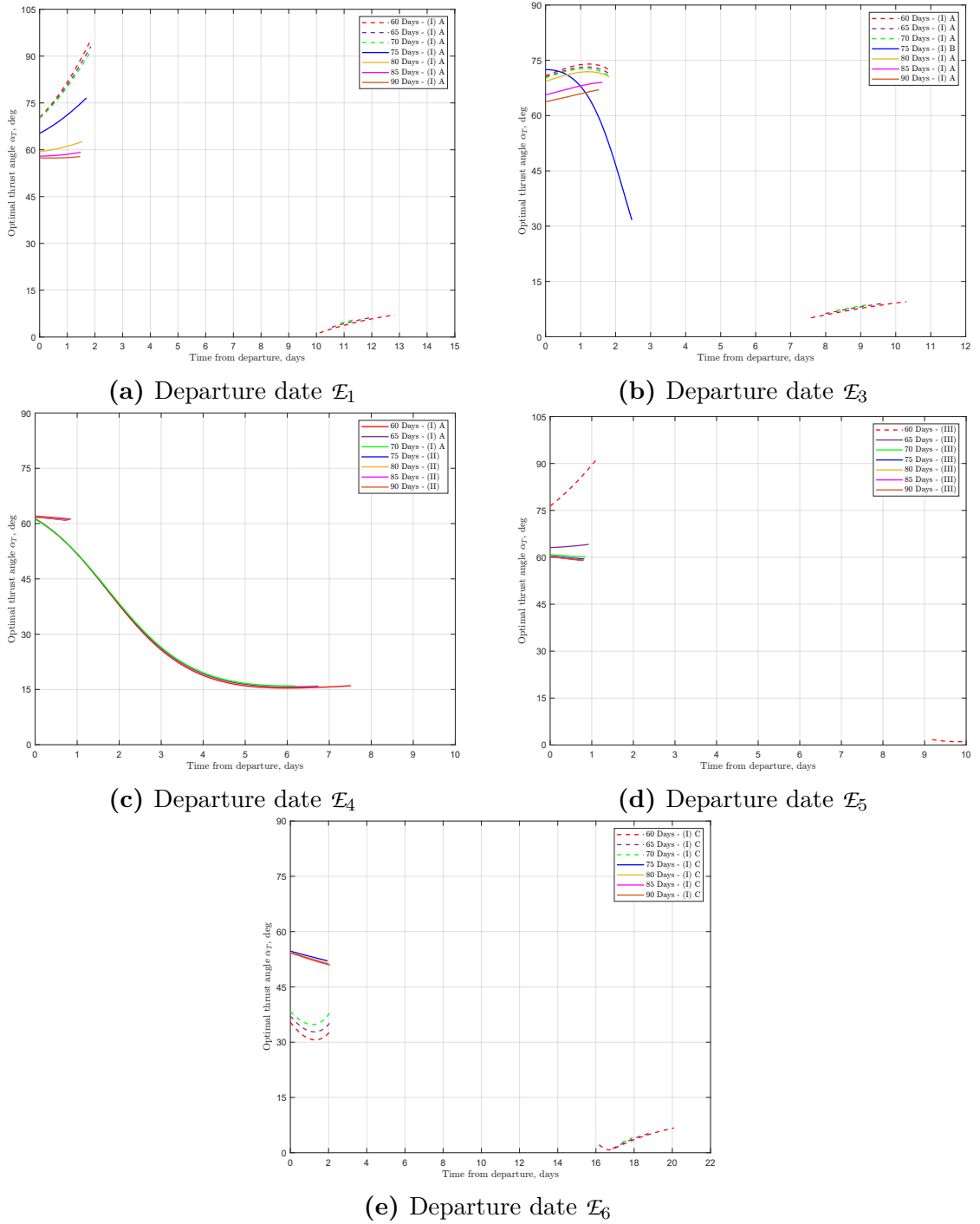


Figure 4.11: EML2 selected escape trajectories - trend over time of optimal thrust angle - variable Δt , free \mathcal{C}_{3f}

Escape Trajectories from Earth-Moon L2

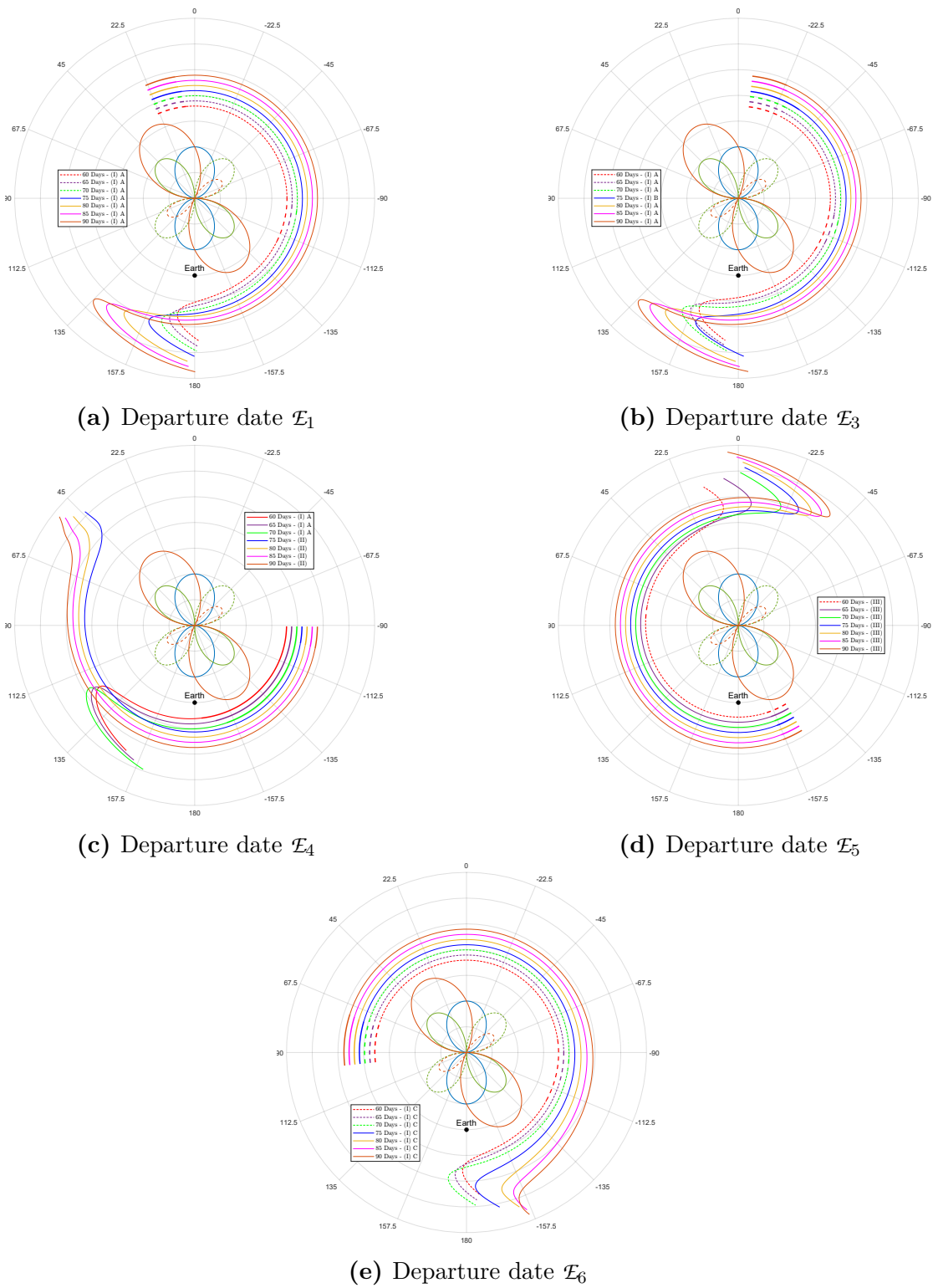
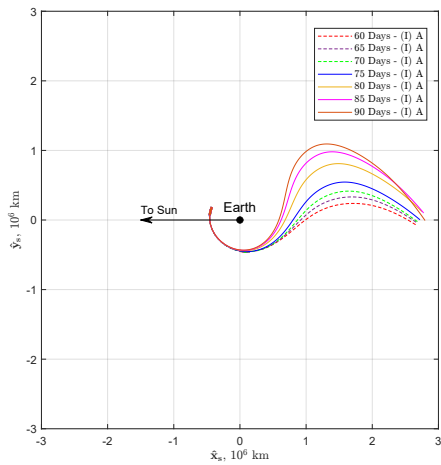
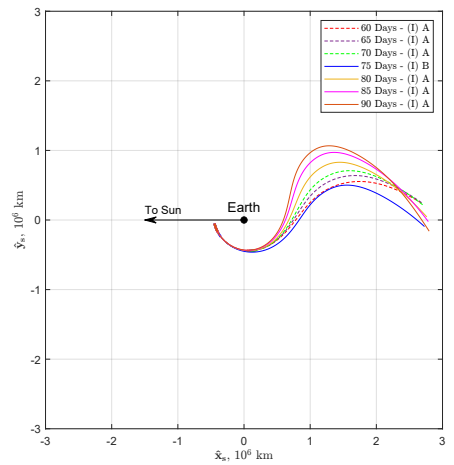


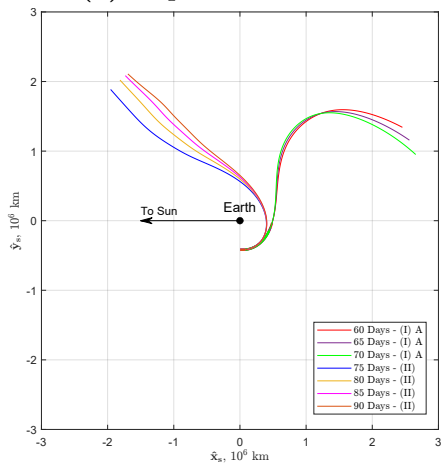
Figure 4.12: EML2 selected escape trajectories polar plot - variable Δt , free \mathcal{C}_{3f} , Earth-Spacecraft rotating RF



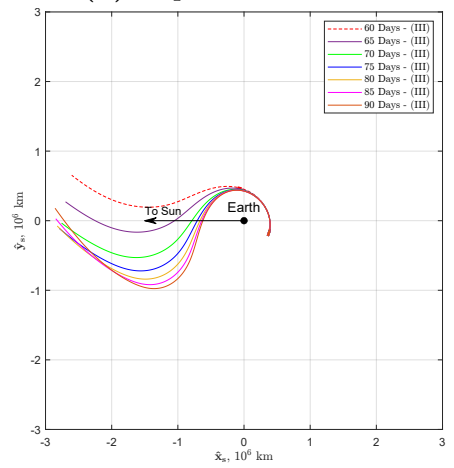
(a) Departure date \mathcal{E}_1



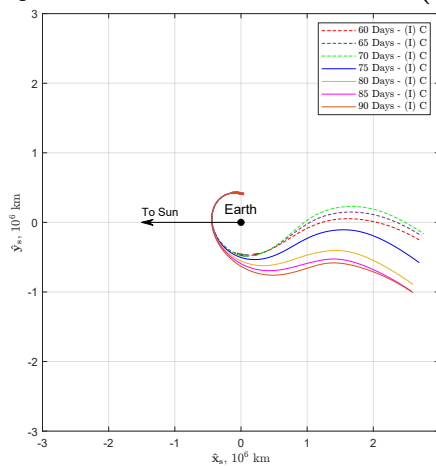
(b) Departure date \mathcal{E}_3



(c) Departure date \mathcal{E}_4



(d) Departure date \mathcal{E}_5



(e) Departure date \mathcal{E}_6

Figure 4.13: EML2 selected escape trajectories - variable Δt , free \mathcal{C}_{3f} , SE synodic RF

4.4 Escapes with constrained final energy \mathcal{C}_{3f}

In the latter section, an analysis is conducted to assess how imposing the final characteristic energy affects the escape performance. For each of the five previously selected dates, \mathcal{C}_{3f} is varied from $0.1 \text{ km}^2/\text{s}^2$ to $0.5 \text{ km}^2/\text{s}^2$. Again, due to the complex lunisolar gravitational perturbations, the solutions exhibit distinct families. Figure 4.14 displays the manifold of solutions for the selected dates, while Table 4.6 presents their respective performances.

Figure 4.15 shows the Sun-Spacecraft angle for each starting date, while Figure 4.16 displays the optimal thrust angle α_T .

Figure 4.17 illustrates the polar views of all escape trajectories as a function of Sun-Spacecraft angle $\Delta\theta$ and Figure 4.18 shows the trajectories in the Sun-Earth synodic RF, centered on Earth.

Starting from the first departure \mathcal{E}_1 , the low-energy scenario is characterized by the presence of a single thrust phase that progressively shortens as the final characteristic energy decreases. This allows the spacecraft to spend more time in the negative contribution region of the solar perturbation, losing energy until the final required energy is reached. This implies an evident reduction in fuel consumption. Once again, the thrust direction is predominantly radial. In the opposite scenario, where a high \mathcal{C}_{3f} must be achieved, the thrust structure requires the introduction of a second thrust arc when the spacecraft is in the unfavorable region. This last propulsive phase becomes longer the higher the final energy required.

Departures \mathcal{E}_5 and \mathcal{E}_6 exhibit behavior quite similar to that just described, but with all trajectories characterized by a two-arc thrust structure. The solutions for \mathcal{E}_6 feature longer average thrust phases than in the \mathcal{E}_5 case because their starting point is located in the region where the contribution of solar perturbations is neutral ($\Delta\theta = 90^\circ$).

Departures at \mathcal{E}_3 requiring low final energy exhibit behavior similar to that found in the analysis with free terminal energy. As \mathcal{C}_{3f} decreases, the thrust structure is modified by the insertion of a second thrust arc, indicating that for low values of final energy, the solutions align with the \mathcal{E}_2 solution presented in Section 4.2. It is important to note that for \mathcal{C}_{3f} less than $0.1 \text{ km}^2/\text{s}^2$, the second thrust phase is eliminated again. In the scenario requiring high energy, the elimination of the second thrust arc is evident. The spacecraft continues to thrust during the initial phase, even while in the negative solar perturbation zone aims of accumulating all the required energy before reaching the peak of σ_u at $\Delta\theta = 180^\circ$.

For \mathcal{E}_4 , only two solutions have been found, which follow the behavior observed in the free final energy scenario. The solutions for \mathcal{C}_{3f} equal to 0.3, 0.2, and $0.1 \text{ km}^2/\text{s}^2$ do not seem to be viable. Further solutions can be found imposing smaller values of \mathcal{C}_{3f} less than $0.1 \text{ km}^2/\text{s}^2$, result in solutions that belong to the family I,

as visible in the analysis carried out with fixed duration.

\mathcal{E}_{3f} (km/s) ²	Line ID	Family	Sub Family	n_p	Duration <i>Days</i>	m_f <i>kg</i>	ΔV <i>m/s</i>
0.10	●	I	A	2	82.37	848.224	41.032
0.20	●	I	A	2	76.74	848.094	44.035
0.30	●	I	A	2	74.40	847.806	50.689
0.40	●	I	A	4	71.76	846.932	70.921
0.50	●	I	A	4	67.21	845.374	107.037

(a) Departure date \mathcal{E}_0

\mathcal{E}_{3f} (km/s) ²	Line ID	Family	Sub Family	n_p	Duration <i>Days</i>	m_f <i>kg</i>	ΔV <i>m/s</i>
0.10	●	I	A	2	81.46	847.924	47.956
0.20	●	I	A	4	75.27	847.182	65.141
0.30	●	I	A	4	70.23	846.353	84.339
0.40	●	I	A	2	67.48	845.316	108.382
0.50	●	I	A	2	61.74	843.676	146.473

(b) Departure date \mathcal{E}_3

\mathcal{E}_{3f} (km/s) ²	Line ID	Family	Sub Family	n_p	Duration <i>Days</i>	m_f <i>kg</i>	ΔV <i>m/s</i>
0.40	●	II		2	86.36	848.940	24.479
0.50	●	II		2	72.84	849.135	19.962

(c) Departure date \mathcal{E}_4

\mathcal{E}_{3f} (km/s) ²	Line ID	Family	Sub Family	n_p	Duration <i>Days</i>	m_f <i>kg</i>	ΔV <i>m/s</i>
0.10	●	III		2	84.77	849.058	21.750
0.20	●	III		2	75.26	849.035	22.290
0.30	●	III		2	70.06	849.003	23.025
0.40	●	III		2	66.11	848.942	24.429
0.50	●	III		2	63.44	848.770	28.402

(d) Departure date \mathcal{E}_5

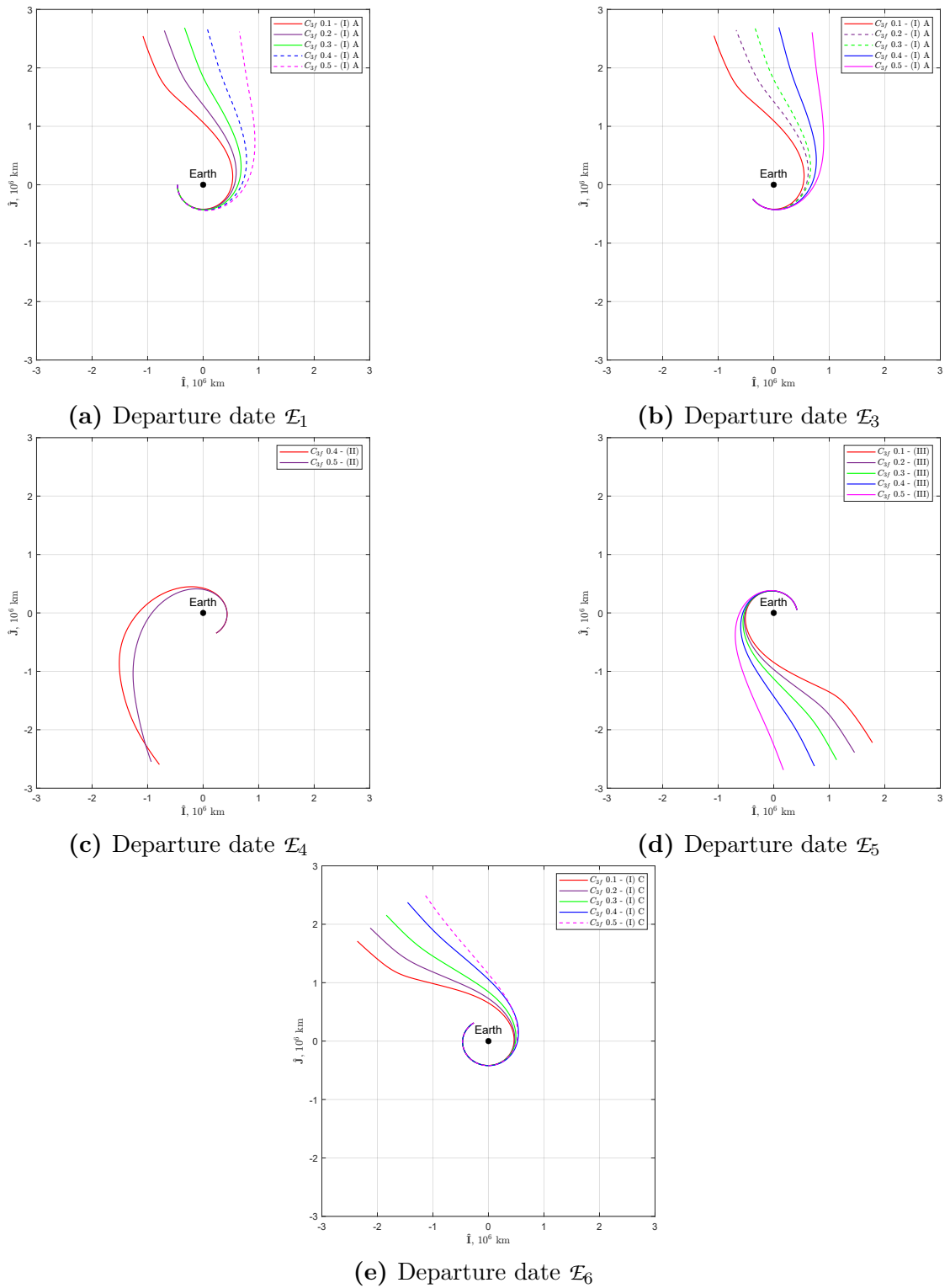


Figure 4.14: EML2 selected escape trajectories over a lunar month - free Δt , fixed \mathcal{C}_{3f} , EME2000 RF

\mathcal{E}_{3f} (km/s) ²	Line ID	Family	Sub Family	n_p	Duration <i>Days</i>	m_f <i>kg</i>	ΔV <i>m/s</i>
0.10	●	I	C	2	85.77	847.743	52.157
0.20	●	I	C	2	79.73	847.740	52.209
0.30	●	I	C	2	75.81	847.736	52.309
0.40	●	I	C	2	73.80	847.725	52.564
0.50	●	I	C	4	66.49	845.769	97.860

(e) Departure date \mathcal{E}_6

Table 4.6: EML2 escape trajectories performance - free Δt , fixed \mathcal{E}_{3f}

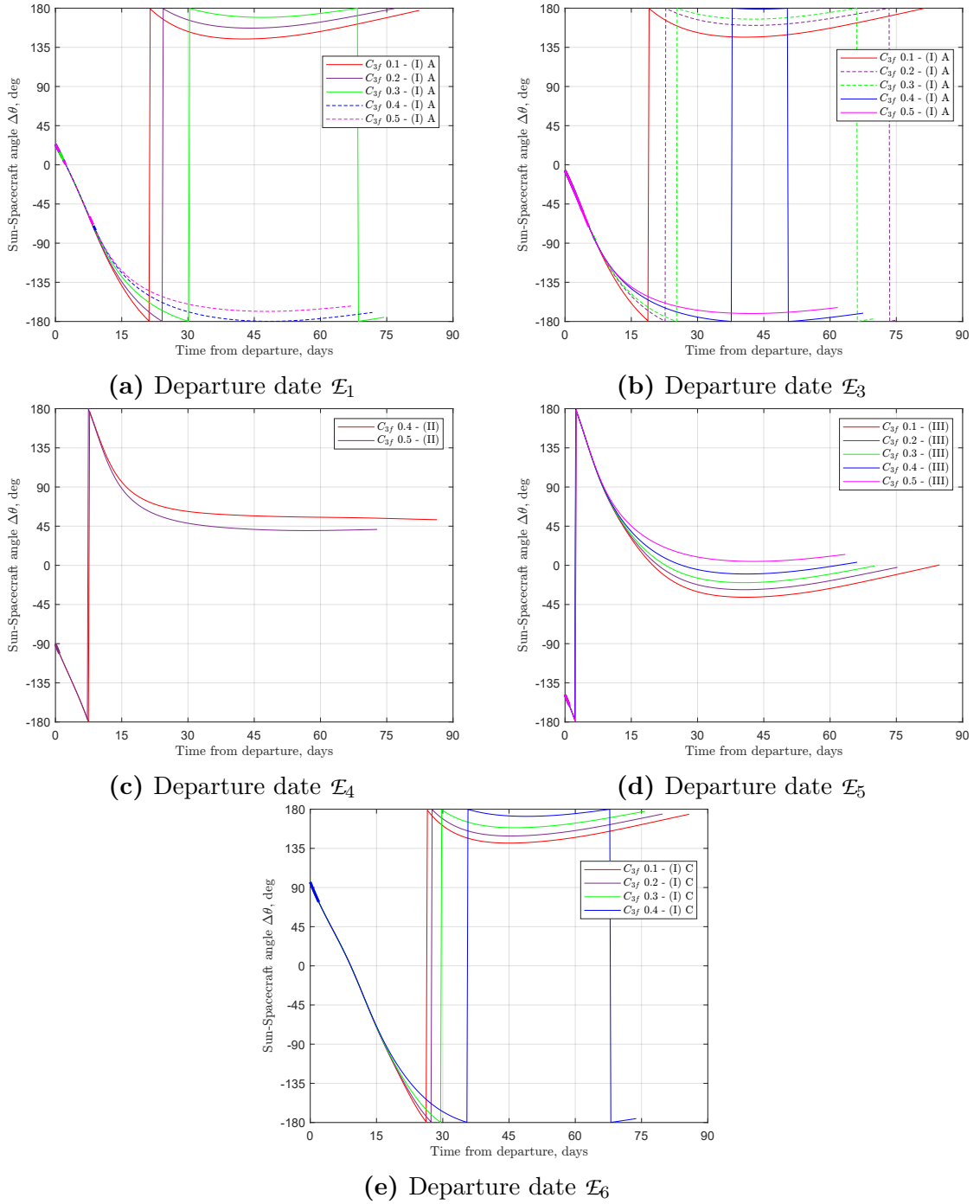


Figure 4.15: EML2 selected escape trajectories - trend over time of Sun-SC relative angle - free Δt , fixed \mathcal{C}_{3f}

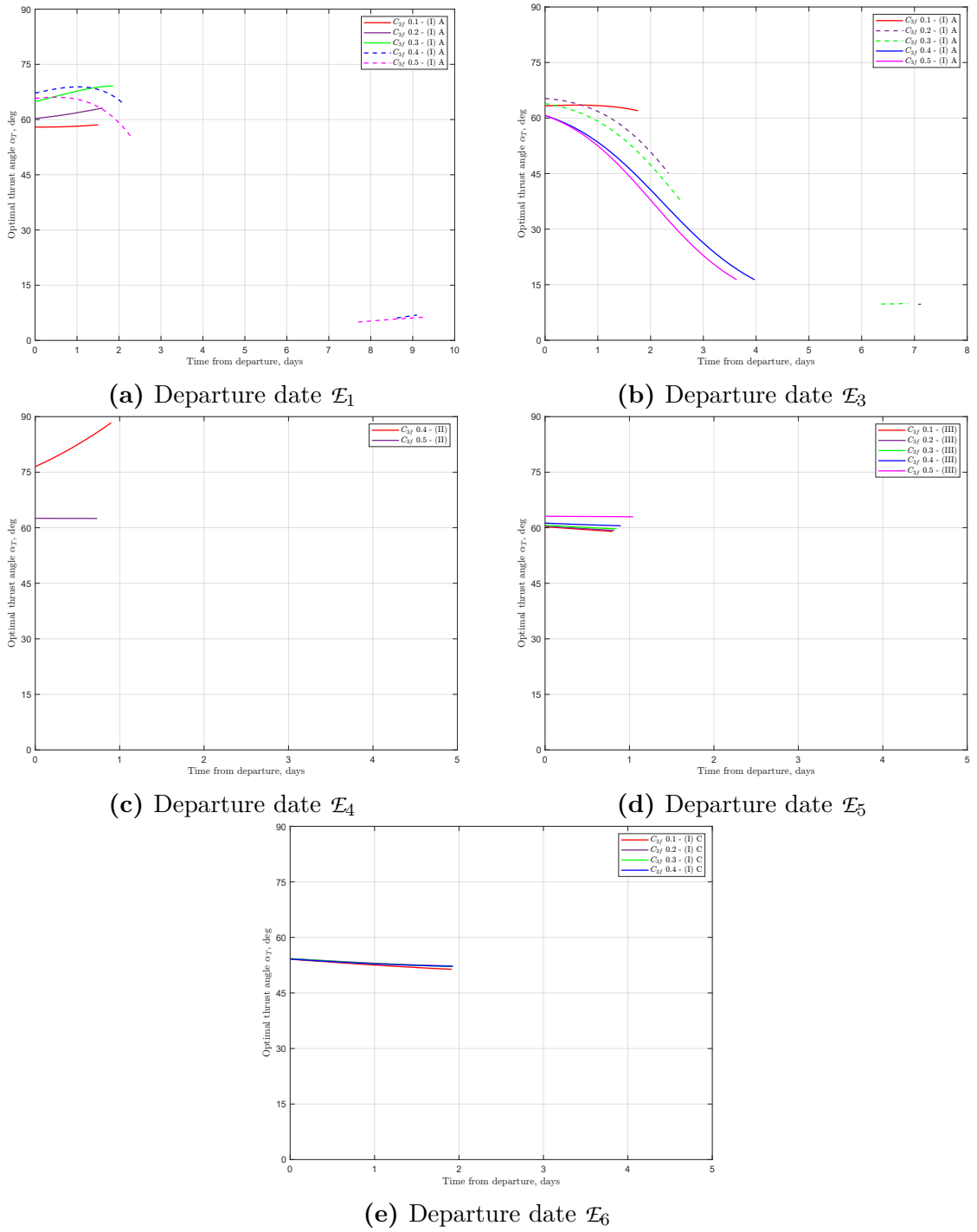


Figure 4.16: EML2 selected escape trajectories - trend over time of optimal thrust angle - free Δt , fixed \mathcal{C}_{3f}

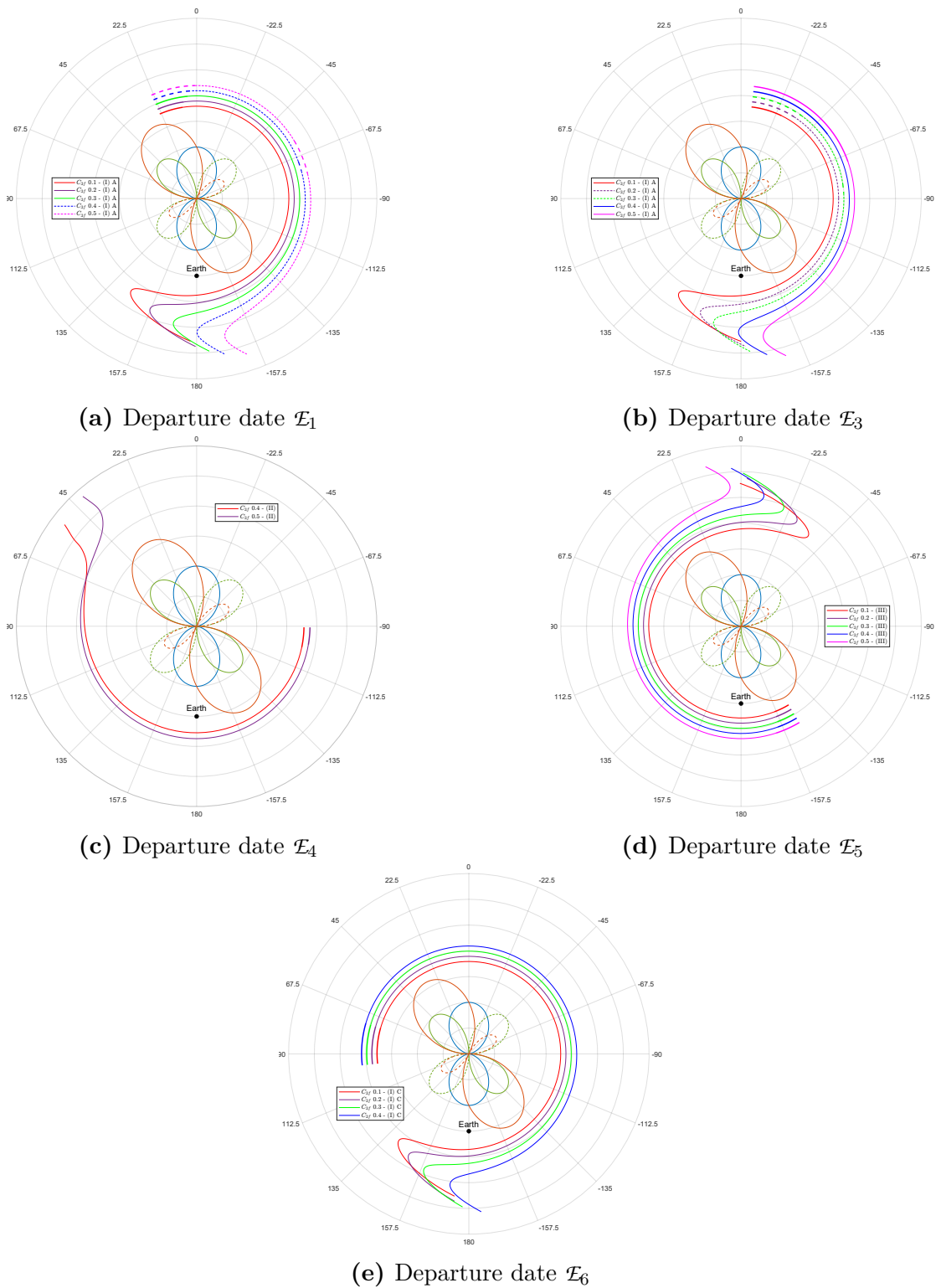
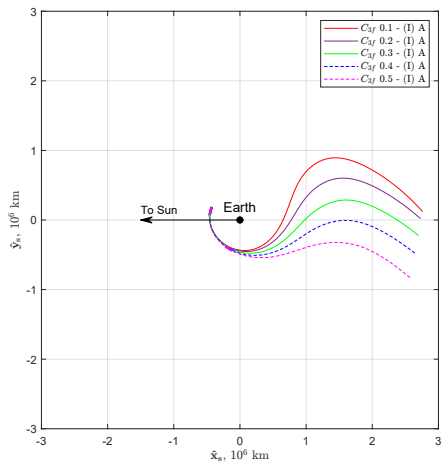
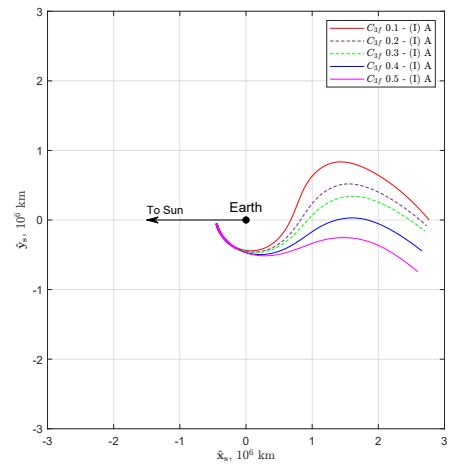


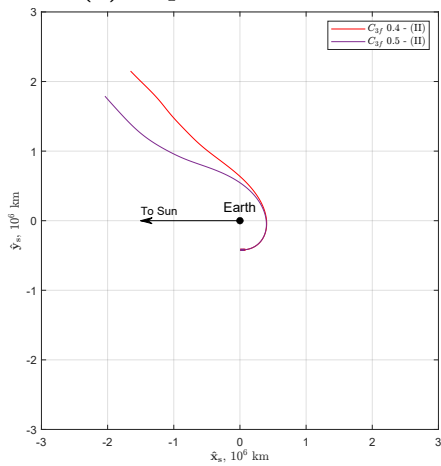
Figure 4.17: EML2 selected escape trajectories polar plot - free Δt , fixed \mathcal{C}_{3f} , Earth-Spacecraft rotating RF



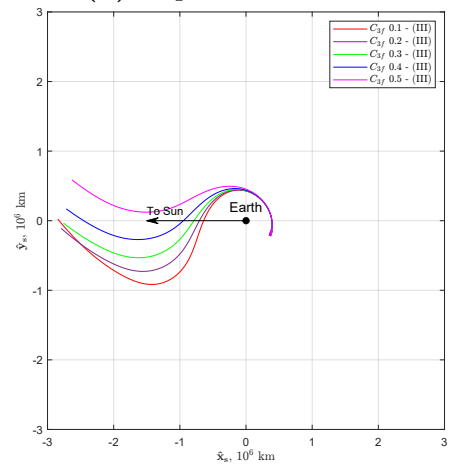
(a) Departure date \mathcal{E}_1



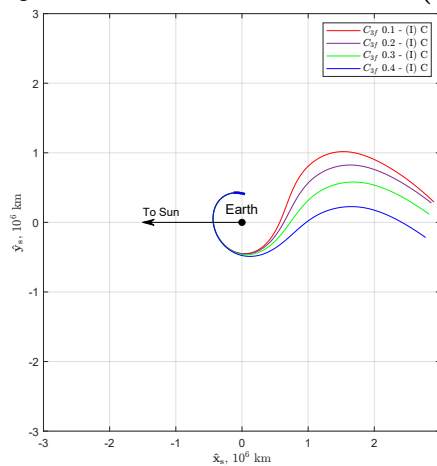
(b) Departure date \mathcal{E}_3



(c) Departure date \mathcal{E}_4



(d) Departure date \mathcal{E}_5



(e) Departure date \mathcal{E}_6

Figure 4.18: EML2 selected escape trajectories - free Δt , fixed \mathcal{C}_{3f} , SE synodic RF

Chapter 5

Conclusion

In conclusion, this thesis has delved into the intricate realm of optimizing escape trajectories from the L2 Lagrangian point in the Earth-Moon system. The choice of this particular scenario may provide insight into the heightened attention toward Lagrangian Points in recent times. These points signify specific equilibrium positions within the context of the three-body problem, enabling small objects like spacecraft to sustain relatively stable positions in relation to two primary bodies within a rotating reference system. Since Lagrangian points (LPs) are considered very attractive from the scientific community, due to their diverse advantages, particularly their suitability for deep space exploration, it is necessary to find effective methods for analyzing trajectories to and from these regions.

In this context, this discussion centers on the space trajectory optimization of low-thrust electric propulsion escapes within a high-fidelity model. Specifically, escape trajectories within the Sun-Earth (SE) and Earth-Moon (EM) binary systems are considered in a dynamical model that includes 4-body gravitation, Solar Radiation Pressure (SRP), and spherical harmonics representing the Earth's asphericity.

Indirect methods were deemed suitable for this purpose and were extensively employed in this work. Chapter 3 provides a thorough discussion of Optimal Control Theory (OCT) and the Multi-Point Boundary Value Problem (MPBVP), identifying the indirect method as the most suitable for addressing the application of OCT to the space trajectory optimization problem.

Pontryagin's Maximum Principle (PMP) was applied to enable crucial post-processing operations, facilitating adjustments to a converged solution when the Thrust Structure (TS) violated the PMP in certain arcs. This comprehensive approach enhances the reliability and effectiveness of trajectory optimization in

the complex dynamics of escape trajectories from Lagrangian Points.

This study offers an analysis of how the performance of escape trajectories is influenced by variations in departure date, duration, and by fixing the characteristic energy \mathcal{E}_3 .

Bibliography

- [1] International Space Exploration Coordination Group. «Global Exploration Roadmap - Supplement October 2022». In: (2022). URL: <https://www.globalspaceexploration.org/> (cit. on p. 1).
- [2] NASA. *Gateway - NASA*. URL: <https://www.nasa.gov/mission/gateway/> (cit. on pp. 1, 4).
- [3] ESA Earth Observation Portal (eoPortal). *Lunar Gateway - eoPortal*. URL: <https://www.eoportal.org/other-space-activities/lunar-gateway> (cit. on p. 1).
- [4] Konstantin Eduardovich Tsiolkovsky. *Exploration of World Spaces by Reactive Devices*. 1903. URL: <https://www.prilib.ru/en/node/416365> (cit. on p. 2).
- [5] John T Betts. *Practical Methods for Optimal Control and Estimation Using Nonlinear Programming, Second Edition*. Second. Society for Industrial and Applied Mathematics, 2010. DOI: 10.1137/1.9780898718577 (cit. on pp. 2, 38).
- [6] R. Bertrand and R. Epenoy. «New smoothing techniques for solving bang-bang optimal control problems - numerical results and statistical interpretation». In: *Optimal Control Applications and Methods* (2002). ISSN: 0143-2087. DOI: 10.1002/oca.709 (cit. on p. 3).
- [7] European Space Agency. *Vigil Mission*. URL: <https://www.eoportal.org/satellite-missions/vigil> (cit. on p. 3).
- [8] European Space Agency. *Euclid Overview*. URL: https://www.esa.int/Science_Exploration/Space_Science/Euclid_overview (cit. on p. 3).
- [9] European Space Agency. *Plato Factsheet*. URL: https://www.esa.int/Science_Exploration/Space_Science/Plato_factsheet (cit. on p. 3).
- [10] European Space Agency. *Ariel Space Mission – European Space Agency M4 Mission*. URL: <https://arielmision.space> (cit. on p. 3).
- [11] European Space Agency. *Ariel Space Mission – European Space Agency M4 Mission*. URL: <https://arielmision.space> (cit. on p. 3).

-
- [12] European Space Agency. *Comet Interceptor - Cosmos*. URL: <https://www.cosmos.esa.int/web/comet-interceptor/home> (cit. on p. 3).
- [13] Michihiro Matsumoto. *Deep Space Transportation System Using the Sun-Earth L2 Point*. 2007 (cit. on p. 4).
- [14] Franco Bernelli Zazzera, Francesco Topputo, and Mauro Massari. *Assessment of Mission Design Including Utilization of Libration Points and Weak Stability Boundaries*. 2004 (cit. on p. 4).
- [15] Keita Tanaka and Jun'ichiro Kawaguchi. «Escape Trajectories from the L2 Point of the Earth-Moon System». In: *Transactions of the Japan Society for Aeronautical and Space Sciences* 57 (4 2014), pp. 238–244. ISSN: 0549-3811. DOI: 10.2322/tjsass.57.238 (cit. on p. 4).
- [16] Luigi Mascolo and Lorenzo Casalino. «Optimal Escape from Sun-Earth and Earth-Moon L2 with Electric Propulsion». In: *Aerospace* 9 (Nov. 2022), p. 186. DOI: 10.3390/aerospace9040186 (cit. on pp. 4, 32–35).
- [17] Luigi Mascolo and Lorenzo Casalino. «Low-Thrust Optimal Escape Trajectories from Lagrangian Points and Quasi-Periodic Orbits in a High-Fidelity Model». In: (2022). URL: <https://hdl.handle.net/11583/2976595> (cit. on pp. 4, 7, 17, 25, 26, 28, 30–35, 38, 42, 56).
- [18] Roger R. Bate, Donald D. Mueller, Jerry E. White, and William W. Saylor. *Fundamentals of Astrodynamics*. Ed. by Dover. Second. 2020. ISBN: 978-0-486-49704-4 (cit. on pp. 7, 10, 13).
- [19] David A. Vallado. *Fundamentals of Astrodynamics and Applications*. Ed. by Microcosm Press. Fourth. Microcosm Press, 2013. ISBN: 978-1881883203 (cit. on pp. 7, 10, 11, 13, 16, 30, 32, 35).
- [20] Victor Szebehely. *Theory of Orbits: The Restricted Problem of Three Bodies*. Ed. by Academic Press. Elsevier, 1967. ISBN: 9780123957320. DOI: 10.1016/B978-0-12-395732-0.X5001-6 (cit. on p. 7).
- [21] Howard D. Curtis. *Orbital Mechanics for Engineering Students*. First. Butterworth-Heinemann, Elsevier, 2005. ISBN: 9780750661690 (cit. on pp. 7, 10, 13, 14, 23, 27).
- [22] *JPL Planetary and Lunar Ephemerides*. URL: https://ssd.jpl.nasa.gov/planets/eph_export.html (cit. on pp. 9, 32).
- [23] William M Folkner, James G Williams, Dale H Boggs, Ryan S Park, and Petr Kuchynka. *The Planetary and Lunar Ephemerides DE430 and DE431*. 2014 (cit. on p. 9).
- [24] National Aeronautics and Space Administration. *Report Concerning Space Data System Standards - Navigation Data - Definitions and Conventions CCSDS 500.0-G-4*. Nov. 2019 (cit. on p. 9).

- [25] Thomas A Pavlak. «Trajectory Design and Orbit Maintenance Strategies in Multi-Body Dynamical Regimes». In: (2013) (cit. on p. 17).
- [26] Joseph-Louis Lagrange. *Essai sur le Problème des Trois Corps*. Ed. by Oeuvres de Lagrange. Vol. 6. 1772, pp. 229–332 (cit. on p. 23).
- [27] National Aeronautics and Space Administration. *Appendix A - Locating the Lagrange Points*. URL: <https://descanso.jpl.nasa.gov> (cit. on p. 23).
- [28] National Aeronautics and Space Administration. *WMAP Observatory: Lagrange Points*. URL: https://wmap.gsfc.nasa.gov/mission/observatory_12.html (cit. on p. 24).
- [29] Richard Fitzpatrick. *Stability of Lagrange Points*. 2011. URL: <https://farside.ph.utexas.edu/teaching/336k/Newtonhtml/node126.html> (cit. on p. 24).
- [30] Neil J. Cornish. *The Lagrange Points*. 1998 (cit. on p. 24).
- [31] Francesco Simeoni, Lorenzo Casalino, Alessandro Zavoli, and Guido Colasurdo. «Indirect Optimization of Satellite Deployment into a Highly Elliptic Orbit». In: *International Journal of Aerospace Engineering* 20 (2012), pp. 389–404. ISSN: 1687-5966. DOI: 10.1155/2012/152683 (cit. on pp. 32–36).
- [32] Camilla Colombo. «Long-Term Evolution of Highly-Elliptical Orbits: Luni-Solar Perturbation Effects for Stability and Re-entry». In: *Frontiers in Astronomy and Space Sciences* 6 (2019). ISSN: 2296-987X. DOI: 10.3389/fspas.2019.00034. URL: <https://www.frontiersin.org/articles/10.3389/fspas.2019.00034> (cit. on p. 32).
- [33] National Geospatial-Intelligence Agency (NGA). *Earth Gravitational Model EGM2008*. 2008. URL: <https://earth-info.nga.mil/> (cit. on p. 35).
- [34] Nikolaos K. Pavlis, Simon A Holmes, Steve C Kenyon, and John K Factor. «The development and evaluation of the Earth Gravitational Model 2008 (EGM2008)». In: *Journal of Geophysical Research: Solid Earth* 117 (B4 Apr. 2012). ISSN: 0148-0227. DOI: <https://doi.org/10.1029/2011JB008916>. URL: <https://doi.org/10.1029/2011JB008916> (cit. on p. 35).
- [35] Derek F. Lawden. *Optimal Trajectories for Space Navigation*. Butterworths, 1963 (cit. on pp. 38, 52).
- [36] David Morante, Manuel Sanjurjo Rivo, and Manuel Soler. «A Survey on Low-Thrust Trajectory Optimization Approaches». In: *Aerospace* 8 (3 2021). ISSN: 2226-4310. DOI: 10.3390/aerospace8030088 (cit. on p. 38).
- [37] Lorenzo Casalino, Guido Colasurdo, and Dario Pastrone. «Optimal Low-Thrust Escape Trajectories Using Gravity Assist». In: *Journal of Guidance, Control, and Dynamics* 22 (5 Sept. 1999), pp. 637–642. ISSN: 0731-5090. DOI: 10.2514/2.4451 (cit. on p. 38).

- [38] Luigi Mascolo, Alessia De Iuliis, and Lorenzo Casalino. «Fast and accurate estimation of fuel-optimal trajectories to Near-Earth Asteroids». In: *Acta Astronautica* 188 (Nov. 2021), pp. 49–56. ISSN: 0094-5765. DOI: 10.1016/J.ACTAASTRO.2021.07.013 (cit. on p. 54).
- [39] Luigi Mascolo and Lorenzo Casalino. «Optimal Escape from Sun-Earth and Earth-Moon L2 with Electric Propulsion». In: *Aerospace* 9 (4 2022). ISSN: 2226-4310. DOI: 10.3390/aerospace9040186. URL: <https://www.mdpi.com/2226-4310/9/4/186> (cit. on p. 54).
- [40] National Aeronautics and Space Administration. *Eclipses and the Moon's Orbit*. URL: <https://eclipse.gsfc.nasa.gov/SEhelp/moonorbit.html> (cit. on p. 58).